STRUCTURAL AND MECHANISTIC ANALYSIS OF MEMBRANE REMODELING BY EPS15-HOMOLOGY DOMAIN-CONTAINING PROTEIN 2

Dissertation zur Erlangung des akademischen Grades des
Doktors der Naturwissenschaften (Dr. rer. nat.)

eingereicht im Fachbereich Biologie, Chemie, Pharmazie
der Freien Universität Berlin

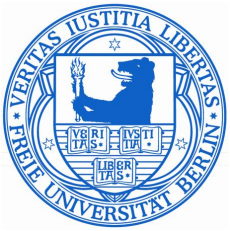

vorgelegt von

M. SC. CLAUDIO SIMON SHAH
aus Starnberg

2012

Die vorliegende Arbeit wurde von Mai 2008 bis September 2012 unter der Leitung von PROF. DR. OLIVER DAUMKE am Max-Delbrück-Centrum für Molekulare Medizin, Berlin-Buch, angefertigt.

1. Gutachter: PROF. DR. UDO HEINEMANN
2. Gutachter: PROF. DR. OLIVER DAUMKE

Disputation am 22. Januar 2013

ABSTRACT

Caveolae are flask-shaped invaginations of the plasma membrane. The Eps15-homology domain-containing protein 2 (EHD2) was recently identified as a caveolar component. The cellular function of EHD2 at caveolae is, however, still unclear. EHD2 is a multi-domain, dimeric ATPase of the dynamin superfamily that tubulates negatively charged liposomes. The amino-terminal (N-terminal) G domain is followed by an α-helical domain, which is connected via a flexible linker to the carboxy-terminal EH domain. As a member of the dynamin superfamily, EHD2 might exhibit a mechano-chemical function.

In this PhD thesis, the ATPase cycle and the structural transition of EHD2 induced by membrane binding were explored. The crystal structure of ADP-bound EHD2 resembled that of the previously determined ATP-bound form. This suggested that ATP hydrolysis does not induce a large scale conformational change. Next, the role of the N-terminus during membrane binding was studied. In solution, the N-terminus was demonstrated to bind to a hydrophobic groove of the G domain using electron paramagnetic resonance (EPR) and X-ray crystallography. Continuous wave EPR spectra and accessibility measurements showed that upon liposome binding the N-terminus switches into the membrane. An EHD2 variant lacking the N-terminus exhibited reduced membrane remodeling activity and concomitantly lost membrane-stimulated ATP hydrolysis. Furthermore, lipid tubules formed by an EHD2 variant lacking the N-terminus did not show the characteristic striated pattern of wild-type EHD2 in electron microscopy. This implied that regular coat formation requires the N-terminus. Interestingly, deletion of the N-terminus did not change the residence time of EHD2 at caveolae. This suggested that the N-terminus of EHD2 might not be involved in caveolae binding but rather in ATPase-dependent remodeling of caveola membranes. It has been shown that the EH domain of EHD2 binds with micromolar affinity to the BAR-domain containing protein PACSIN2, which also resides at caveolae. However, recruitment of EHD2 to caveolae depended on the integrity of the KPFxxxNPF loop and not on the EH domain.

A model was proposed where nucleotide-free EHD2 binds and deforms liposomes into tubular structures with an oligomeric EHD2 coat. Upon addition of ATP, the N-termini promote further membrane deformation.

ZUSAMMENFASSUNG

Caveolae sind kolben-förmige Einstülpungen der Plasmamembran. EHD2 (Eps15-homology domain-containing protein 2) wurde neulich als ein Bestandteil von Caveolae identifiziert. Allerdings ist die zelluläre Funktion von EHD2 an Caveolae noch unklar. EHD2 ist eine multidomänen, dimere ATPase der Dynamin-Familie, welche negativ geladene Liposomen tubuliert. Auf die amino-terminale (N-terminale) G Domäne folgt eine α-helikale Domäne, welche mittels eines flexiblen Linkers mit der carboxy-terminalen EH Domäne verknüpft ist. Als Mitglied der Dynamin-Familie könnte EHD2 eine mechano-chemische Funktion ausüben.

In der vorliegenden Arbeit wurden der ATPase Zyklus von EHD2 und strukturelle Veränderungen, welche durch Membranbindung ausgelöst werden, untersucht. Die Kristallstruktur von ADP-gebundenem EHD2 ähnelte der vorher gelösten ATP-gebundenen Struktur. Das zeigte, dass die Hydrolyse von ATP keine großflächigen konformationellen Änderungen bewirkt. Als Nächstes wurde die Rolle des N-terminus während der Membranbindung untersucht. In Lösung wurde mittels Elektronenspinresonanz (ESR) und Röntgenkristallographie gezeigt, dass der N-terminus in eine hydrophobe Tasche an der G Domäne bindet. ESR Spektren und Akzessibilitätsmessungen bewiesen, dass der N-terminus in Anwesenheit von Liposomen an die Membran wechselt. Eine EHD2 Variante ohne den N-terminus zeigte eine verringerte Membranremodellierungsaktivität und verlor gleichzeitig die membran-stimulierte ATP Hydrolyse. Lipidröhrchen, die sich in Anwesenheit einer EHD2 Variante ohne N-terminus bildeten, zeigten in der Elektronenmikroskopie keine charakteristischen Riffelungen wie wildtyp EHD2. Das implizierte, dass die Bildung einer regelmäßigen Proteinhülle den N-terminus benötigt. Interessanterweise änderte die Deletion des N-terminus nicht die Verweilzeit EHD2s an Caveolae. Das bedeutete, dass der N-terminus wahrscheinlich nicht für die Membranbindung benötigt wird, sondern für die ATP-abhängige Remodellierung der Caveola-Membranen. Es wurde gezeigt, dass die EH Domäne von EHD2 mit mikromolarer Affinität an das BAR Domäne enthaltende Protein PACSIN2 bindet, welches sich ebenfalls an Caveolae befindet. Allerdings hing die Rekrutierung von EHD2 an Caveolae von einer intakten KPFxxxNPF Schleife ab und nicht von der EH Domäne.

Ein Modell wurde vorgeschlagen, in dem nukleotid-freies EHD2 Liposomen bindet und zu Röhrchen deformiert. Diese Röhrchen sind von oligomeren EHD2 umhüllt. Die N-termini vermitteln, nach Zugabe von ATP, eine weitergehende Membrandeformation.

PUBLICATIONS

Parts of this work have been published in the following manuscripts:

Morén, B., Shah, C., Howes, M.T., Schieber, N.L., McMahon, H.T., Parton, R.G., Daumke, O. & Lundmark, R. EHD2 regulates caveola dynamics via ATP-driven targeting and oligomerization. *Mol Biol Cell*, 2012.

Marg, A., Schoewel, V., Timmel, T., Schulze, A., Shah, C., Daumke, O. & Spuler, S. Sarcolemmal repair is a slow process and includes EHD2. *Traffic*, 2012.

CONTENTS

1 INTRODUCTION

Eukaryotic cells are separated from the extracellular space by a lipid bilayer, the plasma membrane. They critically rely on transport of extracellular cargo across the plasma membrane. This transport might be passive, mediated by ion channels, or active, mediated by energy consuming transporters. Extracellular cargo might also enter the cell via endocytosis [1]. In this process, extracellular cargo binds to receptors located on the plasma membrane, thereby triggering the formation of membrane invaginations, which further progress into vesicles. These vesicles, containing the extracellular cargo, are transported to their destinations along the cytoskeleton. Another form of vesicular transport is exocytosis, where vesicles from the insight of the cell fuse with the plasma membrane, thereby emptying their cargo into the extracellular space [2].

In the following, the cellular functions and basic principles of clathrin-mediated endocytosis (CME) and the caveola system will be summarized. Endocytotic pathways depend on similar membrane remodeling strategies. Key players, including dynamin and the dynamin-related Eps15-homology domain-containing proteins (EHDs) will be highlighted.

1.1 CLATHRIN-MEDIATED ENDOCYTOSIS

CME is found in all eukaryotic cells and is linked to many cellular functions, including regulation of cell surface expression of proteins, controlling signaling pathways, removal of membrane components by lysosomal degradation and uptake of nutrients [3].

CME comprises five steps (Figure 1). Nucleation of clathrin-coated pits (CCPs) involves the formation of weak membrane curvature by Fer/CIP4 homology only (FCHo) proteins (containing a F-BAR domain, Section 1.3.2.2) [4] and EGFR pathway substrate 15 (Eps15) [5]. During the second step, the adapter protein 2 (AP2) binds PI(4,5)P_2 and selects cargo through various adapters [6]. Epsin increases membrane curvature with its epsin amino-(N-)terminal homology (ENTH) domain (Section 1.3.1) [7]. In the third step, roughly 100 cytosolic clathrin triskelia and membrane binding adapters are recruited to the emerging CCP and stabilize membrane curvature (Section 1.3.2.1) [8, 9]. The neck of the CCP is tightened by the N-BAR proteins amphiphysin and endophilin (Section 1.3.2.2) [10–12]. The fourth step, vesicle scission, depends on the large GTPase dynamin, which forms oligomeric assemblies around the neck of clathrin-coated pits and catalyzes scis-

sion (Section 1.4) [13, 14]. Brain-derived clathrin coated vesicles (CCVs) have an average outer diameter of 70-90 nm [15], compared to 120-150 nm in human epithelial cells [16]. In the last step, the CCV gets uncoated to prepare for fusion with the target membrane. Uncoating is carried out by Auxilin [17], heat shock cognate 70 (HSC70) [18] and Synaptojanin, a phospholipase, degrading PI(4,5)P_2 to PI(4)P [19], which has a lower affinity for AP2 [20, 21].

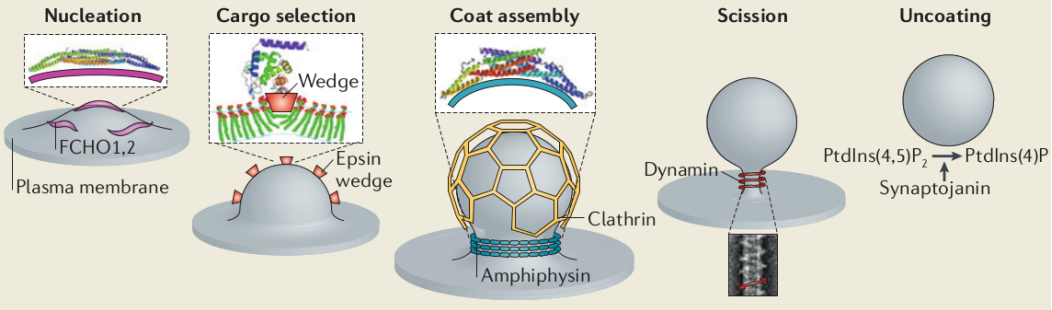

Figure 1: A schematic view on the five steps of clathrin-mediated endocytosis. Figure adapted from [3].

Recent work questioned the current view on clathrin-coated pit formation. Two groups showed independently that clathrin is required already earlier in the process. Cocucci *et al.* report that clathrin together with AP2 nucleates pit formation depending on PI(4,5)P_2 [22], and Kukulski *et al.* report that clathrin defines the spot of pit formation in yeast, but membrane invagination requires the actin skeleton [23].

1.2 THE CAVEOLA SYSTEM

CME was thought to be the most abundant endocytotic pathway for a long time, but now it becomes clear that 70 % of all extracellular material is taken up by clathrin-independent endocytosis [24, 25]. One of the clathrin-independent pathways involves the proteins caveolin1-3 forming cup-shaped plasma membrane invaginations with a diameter of 60-80 nm termed caveolae (Figure 2 A) [26–29]. In contrast to clathrin-coated vesicles, a coat structure can only be observed with specialized methods [26, 28, 30], and caveolae are stably associated with the plasma membrane in unstimulated cells [31]. One caveola holds about 144 caveolin (Cav) molecules in its plasma membrane microdomain [32]. The coat proteins Cav1 and Cav2 are expressed in a wide range of tissues, e.g. endothelial cells, adipocytes, fibroblasts and smooth muscle cells, whereas the expression of Cav3 is restricted to skeletal and cardiac muscle [33].

Cavs are synthesized at the endoplasmic reticulum (ER) and oligomerize in the ER and Golgi [35, 36]. Cavs are integral membrane proteins of 21 kDa in size. They adopt a hairpin conformation in the membrane, with the N- and

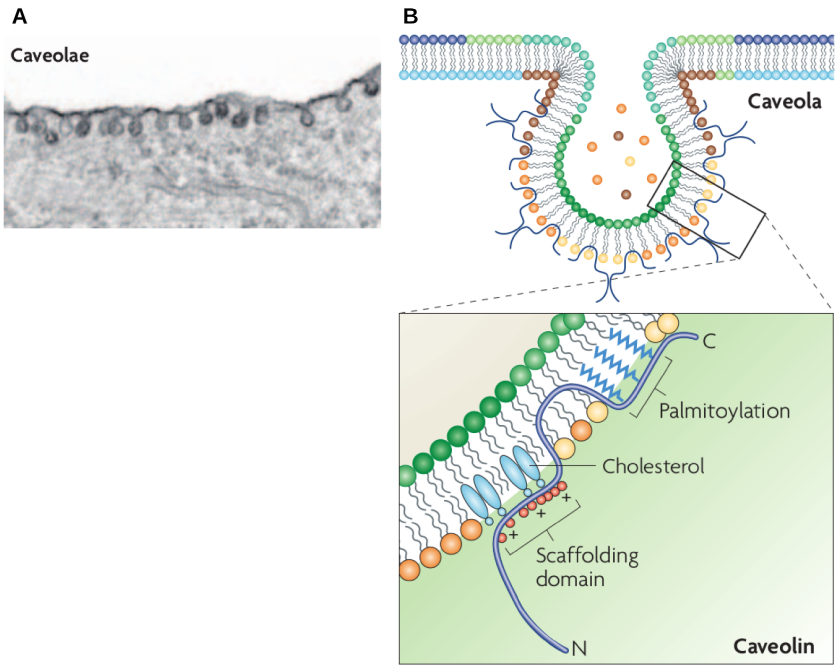

Figure 2: Features of caveolae and caveolin. **A** Electron micograph of typical flask- or cup-shaped caveolae. **B** Schematic drawing of one caveola, showing the characteristic hairpin topology of caveolin. The lower panel shows a magnified view of caveolin with the N- and C-termini, the palmitoylation sites and cholesterol binding indicated. Figure adapted from [34].

carboxy-(C-)termini of the oligomer facing the cytoplasm [37, 38]. They are multiply palmitoylated at their C-termini [39, 40], bind to sphingolipids, specifically sphingomyelin and glycosphingolipids, cholesterol and PI(4,5)P_2 [41] (Figure 2 B). Cavs are associated with the actin filament and microtubuli [42, 28], possibly via filamin, which directly binds actin and Cavs [43].

Overexpression of Cav1 in cells lacking caveolin was sufficient to induce caveola formation [44, 45]. Cav1-, Cav2-, Cav3- and Cav1/Cav3 deficient mice are viable and fertile, but show muscle, pulmonary and lipid metabolism disorders. It becomes clear that Cav1 is the most important Cav for caveola formation in all cell types except muscle cells, because disruption of Cav1 depletes caveolae, whereas in the absence of Cav2 caveolae still form [46–51].

The cavin family was also found to be associated with caveolae [52–57]. Cavin1 drives caveola formation, as loss of cavin1 reduces the amount of caveolae and renders them more mobile and associated with flat plasma membrane [53, 58, 59]. Cavin2 and Cavin3 are both substrates for protein kinase C (PKC) and might target PKC to caveolae [60, 61]. Cavin4 regulates ERK1/2 signaling and myogenesis [62, 63]. The expression profile of Cavin1-3 resembles that of Cav1, whereas the expression profile of Cavin4 is similar to Cav3 [56].

The cellular function of caveolae is not yet fully understood. Roles in endocytosis, lipid metabolism and cellular signaling have been ascribed [34]. In the

last 40 years, it was shown that stretching of cells leads to flattening of caveolae [64, 65]. This indicates a function of caveolae in buffering mechanical stress of membranes [66–71]. Recently, it was observed that stress-induced flattening of caveolae is truly passive, but reassembly of new caveolae depends on ATP and the actin filament (Figure 3) [72].

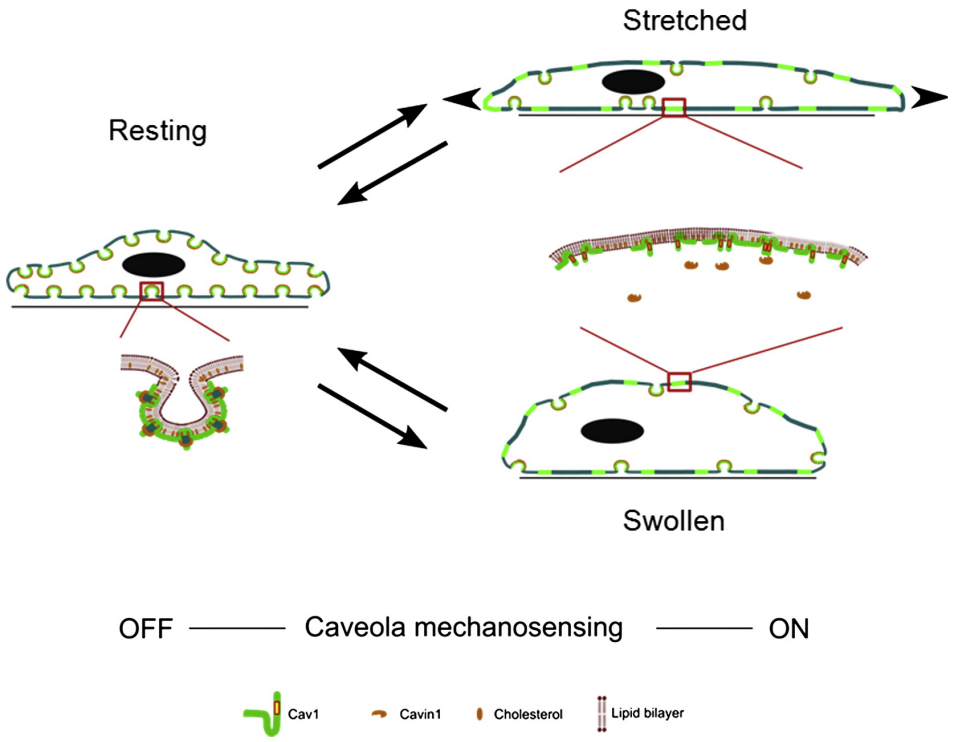

Figure 3: Schematic model of caveolae reacting as a membrane reservoir on mechanical stress. In the resting state caveolae are mostly invaginated. Upon osmotic or mechanical stress caveolae flatten out, buffering membrane tension by providing additional membrane. Figure taken from [72].

1.3 MEMBRANE REMODELING

Cellular membranes normally adopt flat shapes, and energy is needed to deform membranes into shapes competent for endocytosis [73]. At least five different mechanisms for membrane deformation were proposed (Figure 4) [74]:

A. Local alteration of the chemical properties of the acyl chains or the lipid headgroups. For example, phosphatidic acid has two acyl chains and favors negative curvature, whereas lysophosphatidic acid has one acyl chain and favors positive curvature [75].

B. Incorporation of wedge-shaped transmembrane proteins like the K^+-channel. Its shape bends the membrane by displacing more lipid molecules on the outer monolayer than on the inner monolayer [76].

c. Association of the plasma membrane with the cytoskeleton. For example, budding, branching and threadmilling of the actin filament is responsible for the formation of many highly curved membrane protrusions, including filopodia and pseudopodia. It was also shown that many vesicles move along the microtubuli network [77]. Curvature sensing and stabilizing proteins like the BAR domain proteins interact with modulators of the actin network [78].

The remaining two membrane deforming mechanisms will be discussed in more detail below.

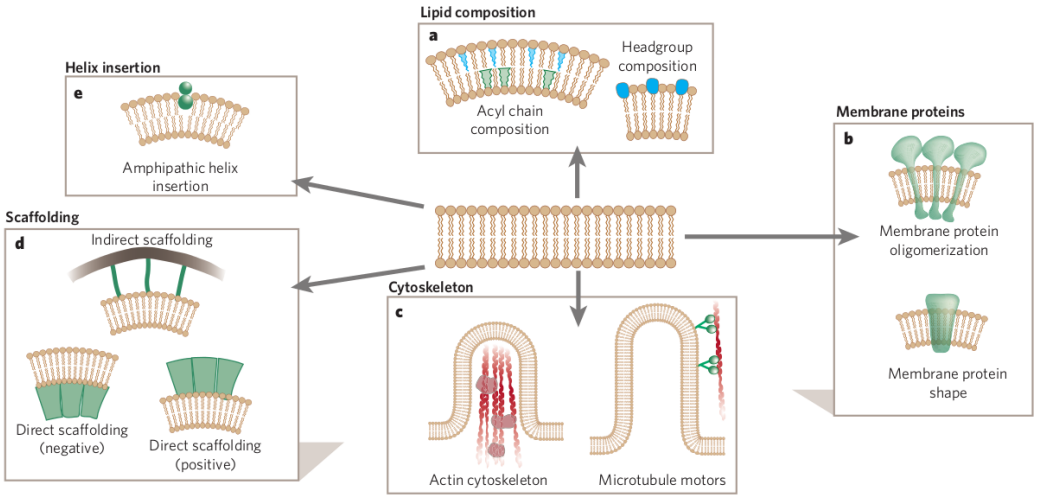

Figure 4: Mechanisms of membrane deformation. The phospholipid bilayer can be deformed causing positive or negative membrane curvature. There are five main categories: **a**, changes in lipid composition; **b**, influence of integral membrane proteins that have intrinsic curvature or have curvature on oligomerization; **c**, changes in cytoskeletal polymerization and pulling of tubules by motor proteins; **d**, direct and indirect scaffolding of the bilayer; **e**, active amphipathic helix insertion into one leaflet of the bilayer. Figure and figure legend were taken from [74].

1.3.1 *Amphipathic helices and membrane curvature*

Amphipathic helices are able to interact with membranes and to induce membrane curvature (Figure 4 e). They are found in various proteins including small GTPases, ENTH domain containing proteins like Epsin, and in N-BAR domain containing proteins (Section 1.3.2.2). They are often unstructured until they insert into the membrane. Amphipathic helices have two sides, one is hydrophilic with its residues oriented towards the aqueous phase, and the other is hydrophobic with its residues dipping into the hydrophobic phase of the membrane. This results in a displacement of the lipid headgroups and a reorientation of the acyl chains (Figure 5) [74]. Interestingly, lipid monolayers can also be curved by am-

phipathic helices [79]. This indicates that membrane binding is not only caused by the generation of bilayer asymmetry and headgroup displacement, but mainly by reorientation of the acyl chains. Theoretical calculations show that shallow insertion of side chains drives the membrane to higher curvature than deep insertion [80].

Other amphipathic helices might only insert into membranes with a certain curvature. Thereby they sense the membrane curvature. Proteins containing an amphipathic helix as a curvature sensor might fine tune their preferred curvature by slight conformational changes of their amphipathic helix.

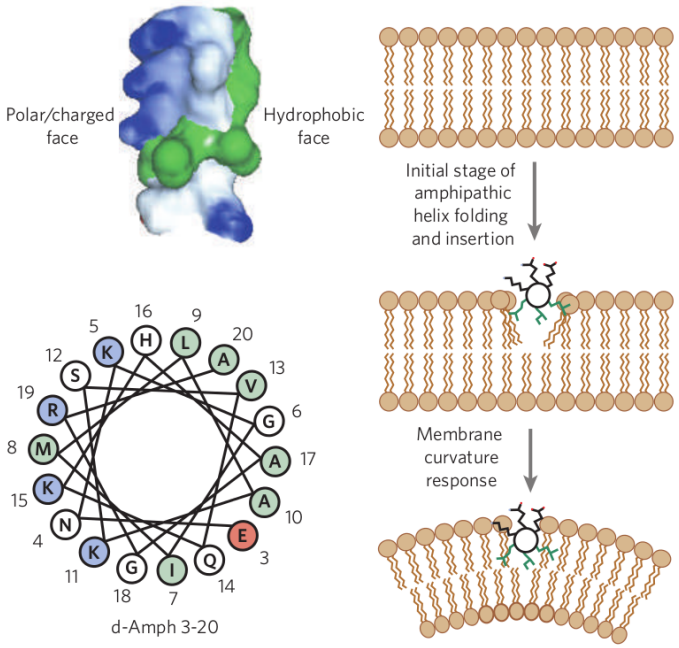

Figure 5: Amphipathic helices are typically 15 to 20 amino acids in length with one polar/charged face and one hydrophobic face (left panel top and bottom). They fold upon interaction with the membrane and displace the lipid headgroups and acyl chains, thereby introducing membrane curvature (right panel). Figure was taken from [74].

The small GTPases Sar1 and Arf1 from the Ras superfamily have an amphipathic helix at their N-termini. Both proteins rearrange their interswitch region upon GTP binding, causing a relocation of their N-terminal helices to the plasma membrane (Figure 6). Arf1 is myristoylated at the N-terminus, whereas Sar1 is not, but both bind to the membrane with highest affinity in the GTP-bound form and to a lesser extent in the GDP-bound and nucleotide-free form [81–87]. GEFs and GAPs are necessary for nucleotide exchange in small GTPases. Interestingly, the GAPs for Arf1 (ArfGAP1) and Sar1 (Sec23-24 and Sec13-31 forming the coat protein complex II) prefer curved membranes, whereas GEFs for Arf1 (GBF-1) and Sar1 (Sec12) prefer binding to flat membranes [88–90]. ArfGAP1 senses the membrane curvature with its amphipathic helix, called ArfGAP1-like lipid packing sensor (ALPS) [91].

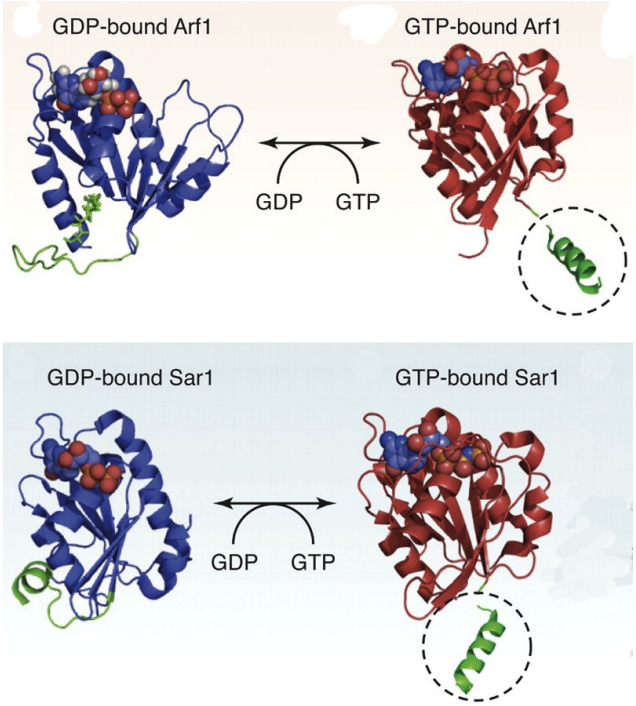

Figure 6: Cartoon representation of crystal structures of the small GTPases Arf1 (top) and Sar1 (bottom) in the GDP- (left) and GTP-bound (right) state. Both GTPases expose their N-termini in the GTP-bound state and bind membranes preferentially in the GTP-bound state. Figure taken from [92].

1.3.2 *Protein scaffolds and membrane curvature*

Protein scaffolds with a curved membrane interaction site were identified. They impose their intrinsic curvature on the membrane, thereby creating membrane curvature (Figure 4 d) [74]. For such a mechanism, these protein scaffolds have to be more rigid than the membrane and the energy gained from membrane binding has to exceed the energy required for membrane deformation [73].

Scaffolding proteins can be subdivided into two groups. a) Indirect scaffolding proteins bind the membrane via adapters and include the coat proteins clathrin, coat protein complex I (COPI) and COPII. b) Direct scaffolding proteins bind the membrane directly and include BAR domain containing proteins, caveolin1 and flotilin1. The dynamin superfamily including the EHD family of proteins can also be grouped into the direct scaffolding proteins (Section 1.4 and Section 1.5).

1.3.2.1 *Coat proteins clathrin, COPI and COPII*

In clathrin-mediated endocytosis (Section 1.1), clathrin triskelia self-assemble into empty cage-like structures that bind to membranes only via an inner layer of heterotetrameric adapter proteins [93]. COPI- and COPII-coated vesicles mediate transport from the Golgi to the ER, and vice versa. COPI coats are built of a single, multisubunit assembly, whereas COPII coats are built of two complexes, Sec13-31

and Sec23-24. Similarly to the clathrin coat, they also form empty cages, which bind to the membrane via an adapter layer [94, 95].

All three coats act as scaffolds by imposing their intrinsic curvature on the membrane, but might also limit the curvature generated by proteins, which posses an amphipathic helix. For example, epsin generates curvature with the amphipathic helix of its ENTH domain, and the scaffolding protein clathrin could control epsin's contribution to membrane fission. Also the small GTPases Sar1 and Arf1 are known to promote membrane fission by insertion of amphipathic helices, and their curvature inducing potential could be limited by the associated COP [96].

1.3.2.2 *BAR domains*

BAR (BIN/Amphiphysin/Rvs) domains are typical direct scaffolding domains and were identified as conserved domains in the yeast proteins Rvs161 and Rvs167 (reduced viability upon starvation) and the metazoan amphiphysin/BIN (bridging interactor) proteins [97–99]. The crystal structure of human arfaptin-2 [100] revealed the first structure of a BAR domain, but was recognized as a BAR domain only after structural homology to *Drosophila melanogaster* Amphiphysin [99] was revealed. BAR domains are purely α-helical and dimerize into crescent-shaped modules with a positively charged membrane interacting surface.

The BAR domain superfamily comprises classical BARs, N-BARs (with an N-terminal amphipathic helix), F-BARs (Fer/CIP4 homology, [101, 102]) and I-BARs (inverse-BAR, [103]). These BAR subfamilies prefer different curvatures, with F-BAR binding to weakly curved membranes, N-BAR binding to highly curved membranes and I-BAR binding to inversely curved (convex) membranes (Figure 7). Some BAR domain containing proteins have additional lipid binding domains, e.g. Sorting Nexin 9 (SNX9) has a PhoX (PX) domain, or additional protein-protein interaction domains, e.g. Tuba and PACSINs bear Src homology 3 (SH3) domains [104].

N-BAR proteins, and F-BAR proteins from the PACSIN (Syndapin) family generate membrane curvature with membrane binding modules located in the vicinity of the BAR domain scaffold. Amphiphysin contains an N-terminal amphipathic helix, which is known to deform lipid membranes [99]. Endophilin bears two amphipathic helices, one N-terminally, and one centrally located [106, 107]. The N-terminal amphipathic helix of endophilin might serve as a stabilizer of the oligomeric BAR domain ring by coupling with amphipathic helices from the neighboring endophilin ring. Therefore the amphipathic helix of endophilin not only binds to the membrane, but also controls tubulation [108].

Recently, the vesiculation potential of three BAR domain containing proteins was compared. Endophilin (4 amphipathic helices per dimer) showed the highest vesiculation efficiency, amphiphysin (2 amphipathic helices per dimer) showed a

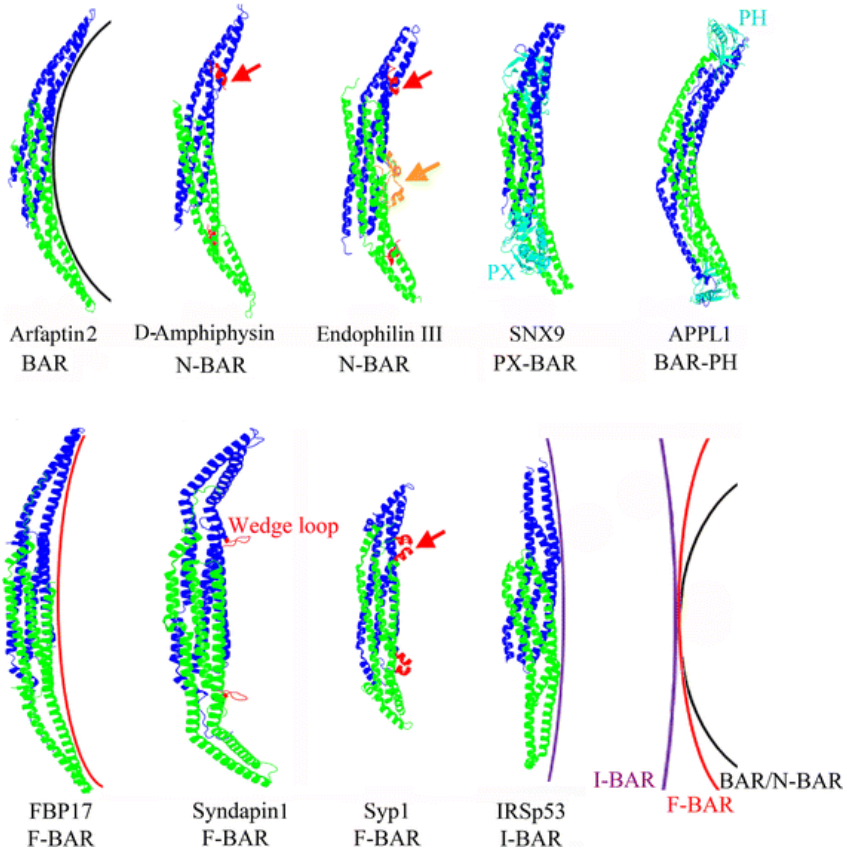

Figure 7: Cartoon representation of various BAR domains shows architectural differences between BAR, N-BAR, F-BAR, PX-BAR, BAR-PH and I-BAR domains. BAR and F-BAR domains induce positive curvature, I-BAR domains generate negative curvature. Amphipathic α-helices are indicated by a red or orange arrow. Figure adapted from [105].

reduced vesiculation efficiency and GRAF (no amphipathic helix) showed only tubulation without vesiculation. Thus, it was speculated that amphipathic helices promote fission and protein scaffolds limit membrane curvature, whereby promoting lipid tube formation [96].

The F-BAR domain containing PACSINs interact with the membrane not only via their crescent-shape positively-charged surface, but their elongated BAR domain bears a wedge loop, consisting of roughly 10 residues, which interacts with the membrane [109–111]. The membrane tubulating potential of PACSIN1, which has a shorter linker between the F-BAR domain and the SH3 domain compared to PACSIN2, is regulated by phosphorylation at two helix capping motifs of the helical bundle [112]. The PACSIN-specific, membrane interacting wedge loop might control the scaffold curvature. The flexible wedge loop of PACSIN1 and PACSIN2 might lead to curvature independent membrane binding. The rigid wedge loop of PACSIN3 influences lateral interactions of dimers, thereby explaining its preference for membranes with low curvature [113].

Endocytosis is coupled to the actin cytoskeleton, which is regulated by the Rho family of small GTPases [114]. PACSIN2 is a versatile interaction hub, its binding partners include Rac1, a member of the Rho family [115]. Furthermore it might recruit dynamin via its auto-inhibitory SH3 domain [110, 111] and interact with Eps 15 homology (EH) domains via three NPF motifs located in the linker between the F-BAR domain and the SH3 domain.

1.4 LARGE GTPASES FROM THE DYNAMIN FAMILY

Dynamin is the founding member of the dynamin superfamily of large GTPases. There are three classical dynamins in mammalian cells, dynamin1 and 3 are strongly expressed in neurons and dynamin2 is ubiquitously expressed [116]. Classical dynamins comprise five domains: The N-terminal guanine nucleotide binding (G) domain, the stalk, the bundle signaling element (BSE), the Pleckstrin Homology (PH) domain and the proline-rich domain (PRD). Dynamin-like proteins (DLPs) or dynamin-related proteins (DRPs) share only three domains with the classical dynamins, namely the G domain, the stalk and the BSE. Classical dynamins are involved in vesicle biogenesis at the plasma membrane and DLPs are required for organellar division and fusion (reviewed in [117–120]).

Dynamin was identified in 1987 as a microtubule binding protein [121, 122], only shortly before defects in endocytosis were found in the temperature-sensitive shibire *D. melanogaster* strain [123]. Two years later, the gene affected in the shibire fly was identified as dynamin [124, 125]. Electron-dense bands could be observed on the necks of accumulated invaginated pits at the plasma membrane of shibire flies. Dynamin forms rings and spirals *in vitro* [126, 127] and it can deform negatively charged liposomes into lipid tubules [128, 129].

Recently, the structure of nucleotide-free dynamin1 lacking the unstructured PRD was solved [130, 131]. The structures suggest that the classical Middle Domain (MD) and Guanine Effector Domain (GED) together with the N-terminus of the G domain form the stalk and BSE. The nucleotide-free G domain is connected via the BSE to the stalk. The PH domain is interspersed in the stalk, via two unresolved linker regions (Figure 8).

Assembly of oligomers is mediated via the stalks in a similar fashion as in the DLP MxA [132, 133]. The highly conserved interface-2 is responsible for dimerization. Interface-1 is only formed in the structure of Ford *et al.* and is predicted to be less stable than interface-2, tolerating different oligomeric conformations. Interface-3, also responsible for oligomerization, is predicted to consist of the unresolved loops L1N and L2 at the distal end of the stalk domain (Figure 8 and Figure 9 a).

By fitting the dynamin1 structures into the cryo-EM map of dynamin1 in the constricted oligomeric state [134], both groups report that adjustments in interface-1

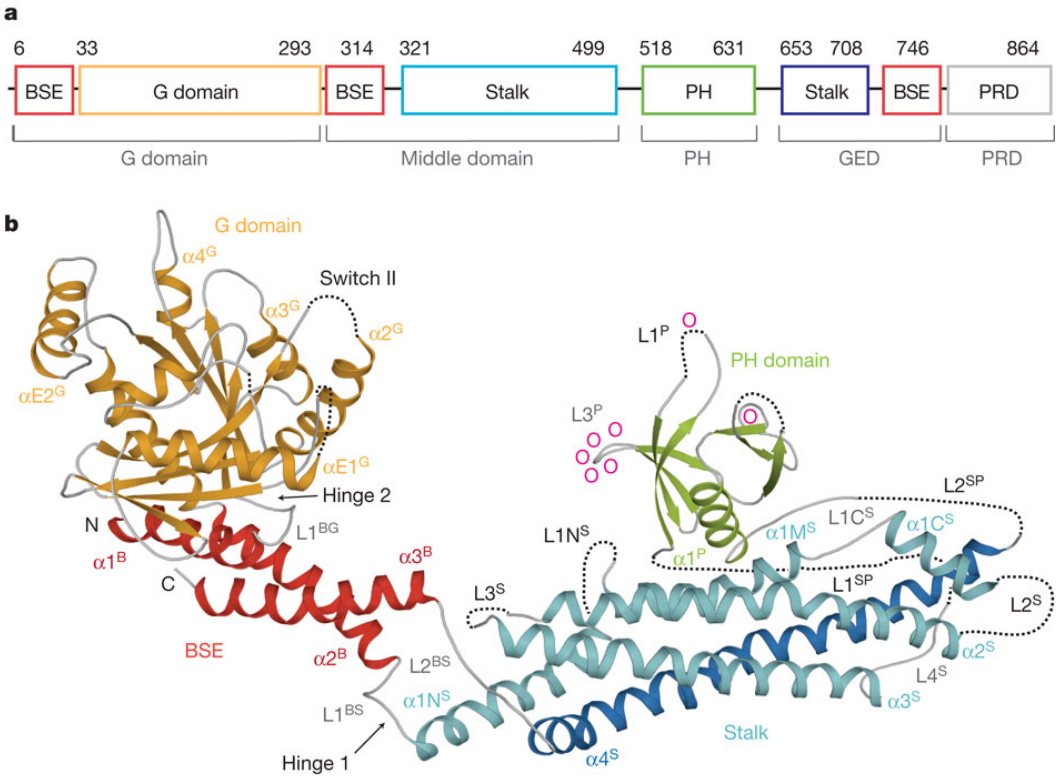

Figure 8: Structure of nucleotide-free human dynamin1. **a** Structure-based domain architecture of human dynamin 1. The classical domain assignment is indicated below. **b** Ribbon-type representation of human dynamin1. Regions not resolved in the crystal structure are indicated by dotted lines. Domains, distinct secondary structure elements and N and C termini are labeled. Lipid-binding residues are indicated as o. Figure and legend taken from [130].

and 3 allow bending of the oligomer and helix formation. Furthermore, both groups suggest that the G domains dimerize in the nucleotide-bound state [135] between adjacent rungs of the helix (Figure 9 b). The PH domains mediate the contact to the membrane.

The mechano-chemical action of dynamin was explained by four widely debated models, the "constrictase" [126], "poppase" [136], "twistase" [137] and "cycling" [138, 139] model. Faelber *et al.* propose a unifying model, where GTP-loaded dynamin molecules loosely form a ring around the neck of a vesicle. Upon closing of one turn, G domains dimerize between the adjacent rung of the helix and trigger GTP hydrolysis. This leads to constriction or compaction of the tube, observable as twisting, followed by dissociation of dynamin from the underlying lipid tube, causing it to collapse.

Dynamin is the best examined example for a mechano-chemical enzyme of the dynamin superfamily. However, it is unclear, if principles of the GTPase cycle, oligomerization and membrane remodeling apply to related members.

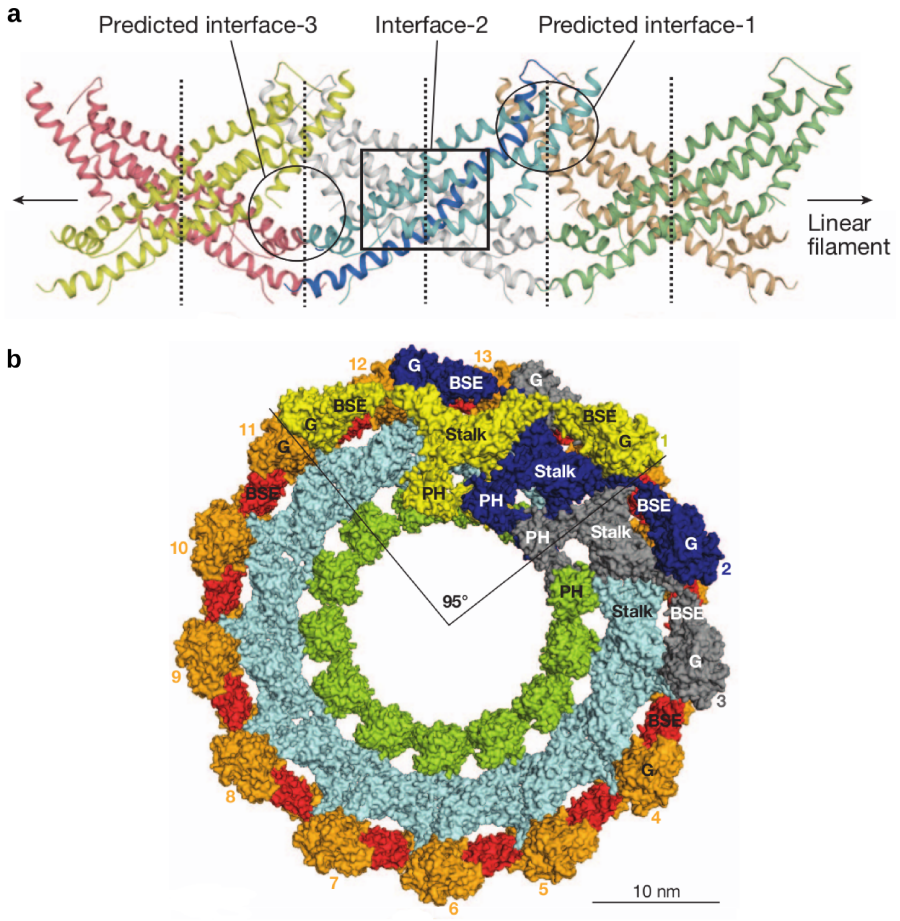

Figure 9: Oligomerization of dynamin 1. **a** In the crystals, stalks were arranged in a criss-cross fashion via crystallographic two-fold axis (black dotted lines). **b** Model of the oligomerized dynamin helix in the constricted state, in top view. Three dimers (1-3) are uniformly coloured. Whereas 13 stalk dimers complete one turn, the G domain of dimer (i) associates with the G domain of dimer (i+10). Figure and legend adapted from [130].

1.5 LARGE ATPASES OF THE EHD FAMILY

Eps15-homology domain-containing proteins (EHDs) comprise a highly conserved dynamin-related protein family in eukaryotes with four members in mammals (EHD1-4) and one in *C. elegans* (Rme-1) and *D. melanogaster* (Past-1) [140–143]. EHDs localize to the plasma membrane or internal membrane systems and regulate different trafficking pathways. EHD1/Rme-1 and EHD3 mediate the exit of proteins from the endocytic recycling compartment. EHD4/Pincher localizes to the plasma membrane and functions in macropinocytosis and Trk receptor internalization (Figure 10) [144]. EHD2 was identified as a component of caveolae in a mass-spectrometry-based screen [52].

Sarcalumenin is the closest relative of the EHDs, but it lacks the EH domain. 34 % of its amino acid sequence are identical to EHD2. Sarcalumenin is a Ca^{2+} binding glycoprotein located in the lumen of the sarcoplasmic reticulum of muscle cells [145, 146].

All four mammalian EHDs are specifically expressed in different tissues, with EHD1 found in testis, EHD2 mainly in heart and skeletal muscle, EHD3 in brain and EHD4 in heart and pancreas [140, 142]. A knock-out of EHD1 in mice resulted in slow endocytosis [147] or defects in spermatogenesis and male fertility [148]. Mice without EHD4 showed a 50 % reduced testis weight [149].

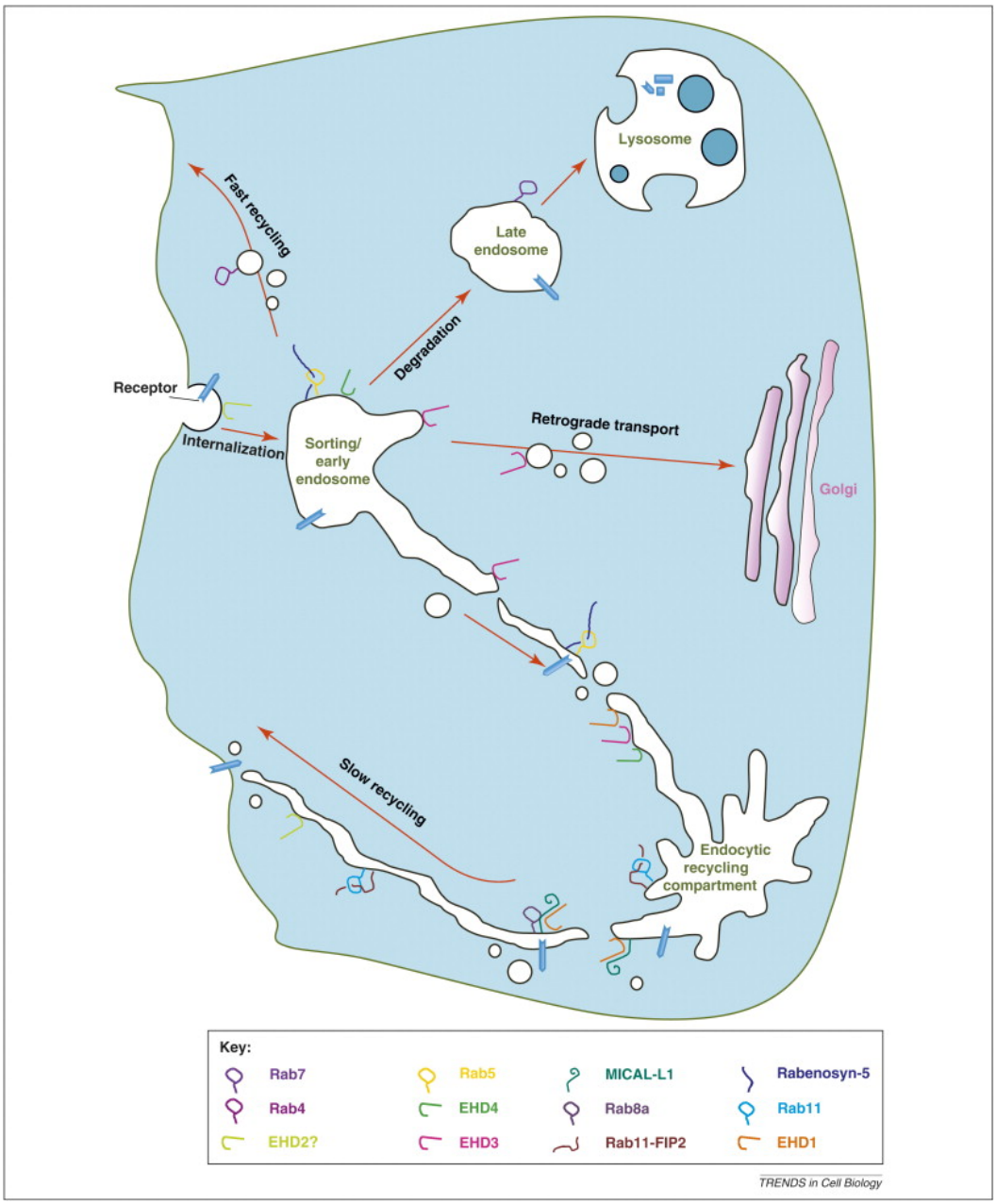

Figure 10: Regulation of endocytic transport by EHD proteins, Rabs and their effectors. Internalized receptors reach the sorting or early endosome (EE) and are trafficked through one of at least four pathways. Receptors slated for degradation are sorted to EE microdomains containing EHD4, Rab5 and Rabenosyn-5 and transported to late endosomes and lysosomes. Other internalized proteins, such as the Shiga toxin, are transported from EE to the Golgi via an EHD3 and/or EHD1-dependent retrograde pathway. Receptors that recycle back to the plasma membrane can do so directly from EE in a poorly defined manner that requires the function of Rab4 (fast recycling). Alternatively, many receptors are first directed to the perinuclear endocytic recycling compartment and then shuttled to the plasma membrane (slow recycling). Slow recycling requires the sequential function of multiple regulators including Rab5, Rab11, Rab8a, their effectors (Rabenosyn-5, Rab11-FIP2 and MICAL-L1, respectively), and EHD proteins. Figure and legend taken from [144].

1.5.1 *EHD2 and caveolae*

Apart from the mass-spectrometry data, no additional evidence for EHD2's involvement in the caveola system was available. Recently, co-localization of EHD2 with the caveolar components Cav1 and Cavin1-4 was observed in HeLa cells. PACSIN2, a previously identified caveolar component, temporarily co-localized with Cav1 and EHD2. EHD2 had a preference for surface-associated Cav1-positive structures. A movie using Total Internal Reflection Fluorescence (TIRF) microscopy showed mobile caveolae upon over-expression of EHD2 K328D (a membrane binding deficient mutant) and immobile caveolae upon over-expression of EHD2 wild-type (Figure 11 with representative still images). This indicates that EHD2 confines caveolae to the plasma membrane [150].

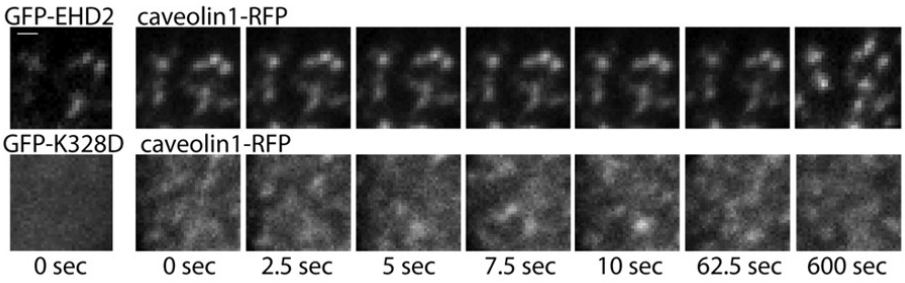

Figure 11: EHD2 regulates caveolae dynamics. Cav1-RFP-positive structures are more dynamic, when co-expressed with a membrane-binding incompatible mutant of EHD2 (GFP-EHD2 K328D), compared to co-expression with GFP-EHD2. Representative images from a TIRF microscopy movie of cells co-transfected with GFP-EHD2 and Cav1-RFP or GFP-EHD2 K328D and Cav1-RFP. Images were taken every 50 ms. Scale bars = 1 µm. Figure and figure legend were adapted from [150].

1.5.2 *EHD2 is involved in membrane repair after muscle lesions*

Muscle activity imposes permanent mechanical stress on the sarcolemma of muscle cells, leading to microinjuries of skeletal muscle [151]. Sarcolemmal repair is mediated by fusion of intracellular vesicles with the membrane in a Ca^{2+}-dependent manner [152–156]. The 230 kDa protein dysferlin forms the muscle repair complex together with Cav3, the muscle specific isoform of the integral caveolar protein caveolin [157–159, 33]. Additional components of the muscle repair complex are the annexins A1 and A2 [160] and mitsugumin 53 [161], which is anchored to the membrane by the caveola component Cavin-1 [162, 53].

EHD2 is recruited early to the site of lesions after laser-induced muscle injury in human myotubes. It is found in a peculiar structure during membrane remodeling, the repair dome (Figure 12). EHD2 co-localized as expected with Cav3, the muscle specific isoform of caveolin, in uninjured human myotubes [163].

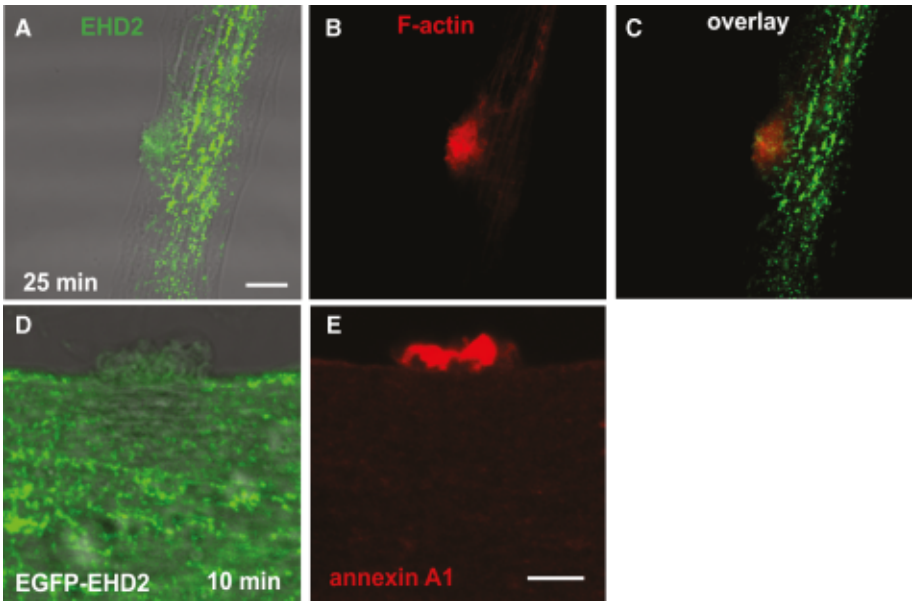

Figure 12: EHD2 translocates into the repair area after laser irradiation. **A** Immunostaining of EHD2 and bright field image of a human myotube 25 min after laser wounding. Bar 5 µm. **B** Co-staining of the same membrane area with phalloidin-atto 565. **C** Overlay from A and B without bright field image. **D** and **E** Detection of EGFP-EHD2 and annexin A1 10 min after laser wounding in a human myotube. Both proteins are localized at the dome area. Bar 5 µm. Figure and figure legend were taken from [163].

1.5.3 *Structure and function*

Members of the EHD family share a common domain architecture (Figure 13). Daumke *et al.* [164] could previously show that, similar to dynamin, EHD2 bound negatively charged liposomes and deformed these lipid templates into tubular structures. In electron micrographs, the lipid tubules are coated by an oligomeric protein coat. In the same study, the authors solved the crystal structure of the dimeric multi-domain ATPase EHD2 in the presence of the non-hydrolyzable ATP analogue, AMP-PNP. The N-terminal G domain is followed by a α-helical domain, which is connected via a flexible linker to the EH domain. The helical domain is composed of a short helical patch located at the N-terminus of the G domain and several α-helices located at the C-terminus of the G domain. The following paragraphs explain the individual parts of the structure in more detail:

AMINO-TERMINUS The N-Terminus is conserved among the EHD family (Figure 14) and might therefore play an yet to be identified role in the function of EHDs. Missing connectivity made it impossible to model the first 19 residues in the AMP-PNP-bound crystal structure.

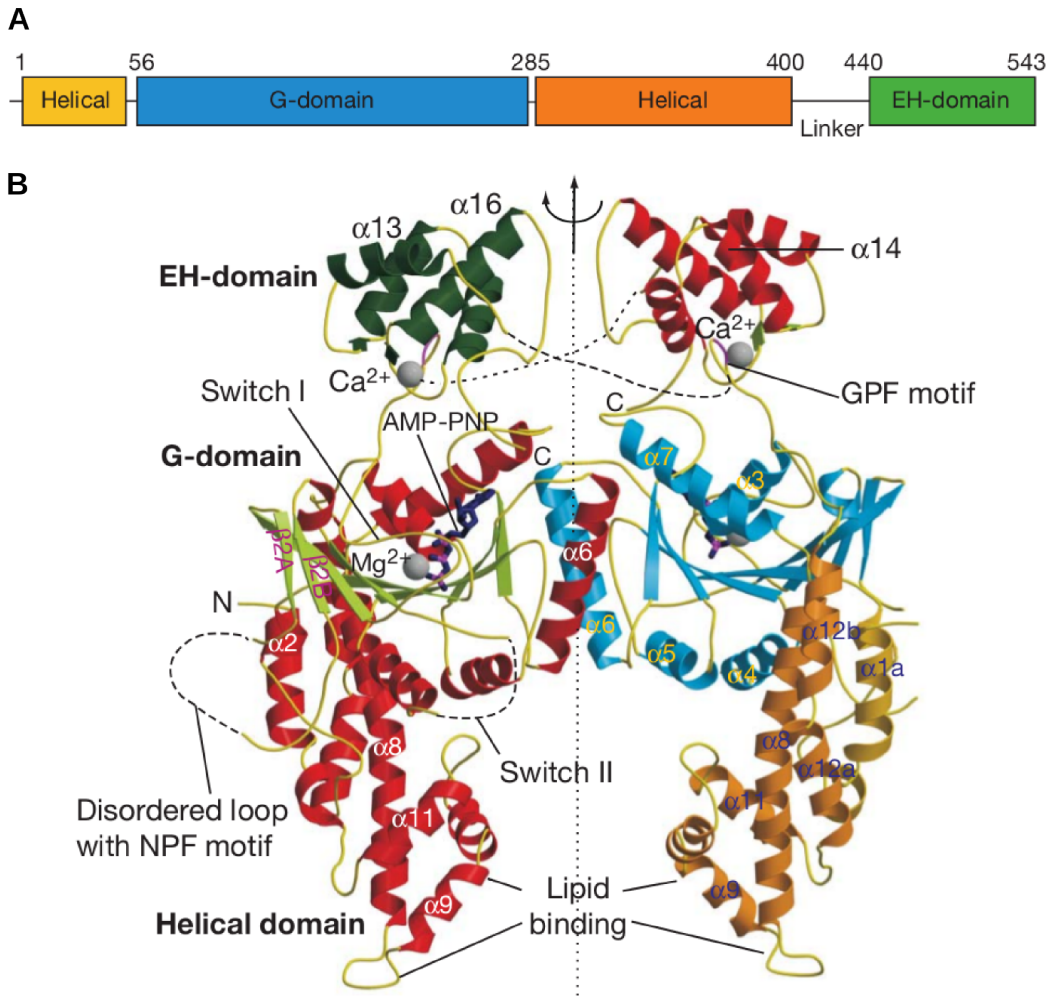

Figure 13: Domain organization and structure of *mouse* EHD2•AMP-PNP. **A** Domain organization. The helical domain consists of two parts, one is located at the N-terminus of the G domain and the other at the C-terminus of the G domain. The EH domain is connected via a linker to the helical domain. **B** The dimeric structure of EHD2•AMP-PNP (PDB: 2QPT). One monomer is colored according to the secondary structure (helices in red, β-strands in green) and the other according to the domain structure as in A. Figure and legend adapted from [164].

G DOMAIN The N-terminal G domain resembles the canonical ras-like G domain fold, where the nucleotide is bound via five distinct G motifs (G1 - G5). The switch I and switch II regions are less well defined in the crystal structure. In comparison to ras-like G domains, EHD2 as well as dynamin have two additional β-sheets inserted in the switch I region, summing up to six parallel and two antiparallel β-sheets surrounded by seven α-helices [165]. Interestingly, the G domain of EHD2 bound and hydrolyzed adenine and not guanine nucleotides, because the additional amino group of guanine cannot be accommodated in the nucleotide binding pocket for sterical reasons. Furthermore, Arg536 which points into the nucleotide binding pocket, forms a salt bridge to a residue in the G4 motif, which is normally primed to interact with the guanine base in ras-like G domains.

Figure 14: Multiple sequence alignment of residues 1-9 of the EHD family. The following sequences were aligned (expasy accession numbers in brackets): *Mus musculus* EHD1 (Q9WVK4), *Mus musculus* EHD2 (Q8BH64), *Mus musculus* EHD3 (Q9QXY6), *Mus musculus* EHD4 (Q9EQP2), *Xenopus laevis* EHD2 (Q7SYA1), *Xenopus laevis* EHD4 (Q7ZXE8), *Caenorhabditis elegans* RME1 (G5EFP1), *Drosophila melanogaster* PAST1 (Q8IGN0). Residues with a conservation of greater than 70 % are color-coded (D,E in red; R, K, H in blue; N, Q, S, T in grey; L, I, V, F, Y, W, M, C in green).

These results confirmed previous observations that EHD family proteins bind ATP instead of GTP [166].

The G domain is the dimerization and oligomerization interface of EHD2: The dimerization interface is conserved among the EHD family and comprises helix α6 containing the highly conserved Trp238 and the adjacent loop. This interface forms independently of the nucleotide and has a buried surface area of roughly 2100 Å² with mostly hydrophobic interactions. It differs from the dimerization interface of interferon-induced guanylate-binding protein 1 (GBP1), bacterial dynamin-like protein (BDLP) and the BSE-G domain fusion dimers from dynamin1 [167, 168, 135].

The oligomerization interface of EHD2 is also conserved among the EHD family. It resembles the dimerization interfaces of the aforementioned dynamin family members and comprises switch I and switch II regions. Introducing single point mutations in the oligomerization interface does not block oligomerization *in vitro*, but inhibits liposome-mediated stimulation of the ATPase function. This shows that the switch I and switch II residues in the oligomerization interface are required for liposome-mediated stimulation of the ATPase. As in other members of the dynamin family, the intrinsic nucleotide hydrolysis reaction is stimulated by membrane binding. However, in EHD2, even the 10-fold stimulated ATPase reaction (k_{obs} = 5.4 ± 0.2 h^{-1}) is still three orders of magnitude lower compared to the stimulated GTPase reaction of dynamin ($k_{cat} \approx 4\ s^{-1}$) [130].

HELICAL DOMAIN Daumke *et al.* previously showed that mutations of hydrophobic and basic residues at the tip of the helical domain interfere with liposome binding and membrane recruitment *in vivo*. Based on these observations, it was suggested that two opposing tips in the helical domain create a highly curved membrane interaction site.

In contrast to the dynamin stalk (Section 1.4), the helical domain of EHD2 does not form a criss-cross and is apparently not involved in dimerization or oligomerization. However, amino acids at the N- and C-terminal end of the G domain of EHD2 form a helical bundle, which protrudes away from the G domain, similar to the BSE in dynamin. In both proteins, the G domain is separated from the membrane via the stalk/helical region. Membrane interaction was suggested to take place via hydrophobic residues at the tip of the helical domain in EHD2, similar to the paddle in BDLP [169], and via the specialized PH domain in dynamin.

EH DOMAIN The C-terminal EH domain comprises two EF hands (helix-loop-helix motifs) and is known to bind to linear Asn-Pro-Phe (NPF) or related motifs. A structural Ca^{2+} ion is thought to stabilize the structure [170–173]. EH domains serve as protein-protein interaction domains and might play a role in trafficking of various proteins, e.g. epsin and stonin [174–176]. EHDs were shown to bind PACSINs [177] and EH domain binding protein 1 (EHBP1), which might couple endocytosis to the actin cytoskeleton [178].

The EH domains of EHD2 bind on top of the opposing G domains to an NPF motif, present in the flexible linker connecting the helical with the EH domain. They were proposed to act auto-inhibitory by sterically blocking G domain mediated oligomerization. Upon membrane binding, the EH domains were suggested to be released from their top position and to bind to an NPF-motif in the KPFxxxNPF loop at the distal side of the neighboring G domain in the EHD2 oligomer. The side position of the EH domain might stabilize oligomerization via this inter-dimer contact.

1.5.4 *ATPase cycle*

It was shown that EHD2 binds and hydrolyzes ATP to ADP. ATP hydrolysis was stimulated by membrane binding, and under stringent membrane binding conditions tubules formed only in the presence of nucleotides [164]. Cell biological experiments demonstrated that the nucleotide binding deficient mutant T72A does not bind membranes and does not localize to caveolae. The nucleotide hydrolysis deficient mutant T94A generated distorted and enlarged caveolae in addition to Cav1-negative tubules (Figure 15).

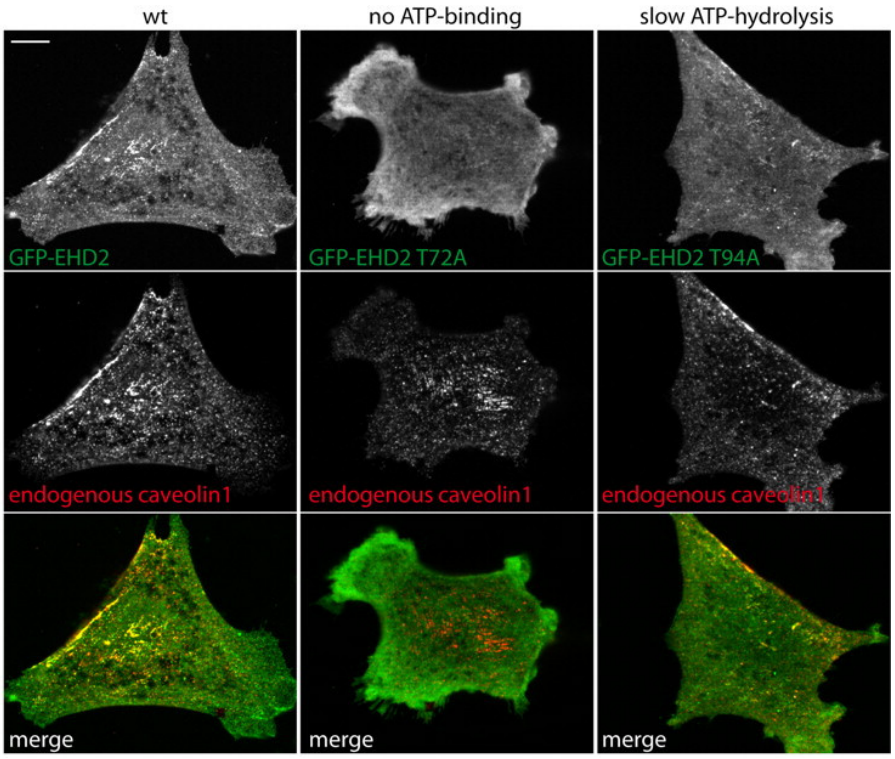

Figure 15: ATP-binding was required for EHD2 targeting, and ATP-hydrolysis regulated the membrane remodeling activity of EHD2. Fluorescent micrographs of 3T3-L1 cells expressing GFP-tagged EHD2 variants and co-stained for endogenous Cav1. Figure and figure legend were taken from [150].

1.5.5 *EHD2 is a member of the dynamin superfamily*

The structural similarities between dynamin and EHD2 suggested that EHD2 belongs to the dynamin superfamily. The G domains of dynamin1 [165, 135] and EHD2 are similar. The helical domain of EHD2 mediates binding to the membrane via the lipid binding site, in analogy to the stalk mediating membrane binding via the PH domain in dynamin. However, when compared to the stalk region of dynamin, the helical domain of EHD2 is shorter and probably not required for oligomerization. The EH domain of EHD2 interacts with NPF motifs and mediates protein-protein contacts, hence has a similar function as the PRD from dynamin, which is known to bind SH3 domains [179–181]. Structural similarities between the dynamin superfamily members MxA, BDLP, GBP1, atlastin1 and EHD2 are shown in Figure 16.

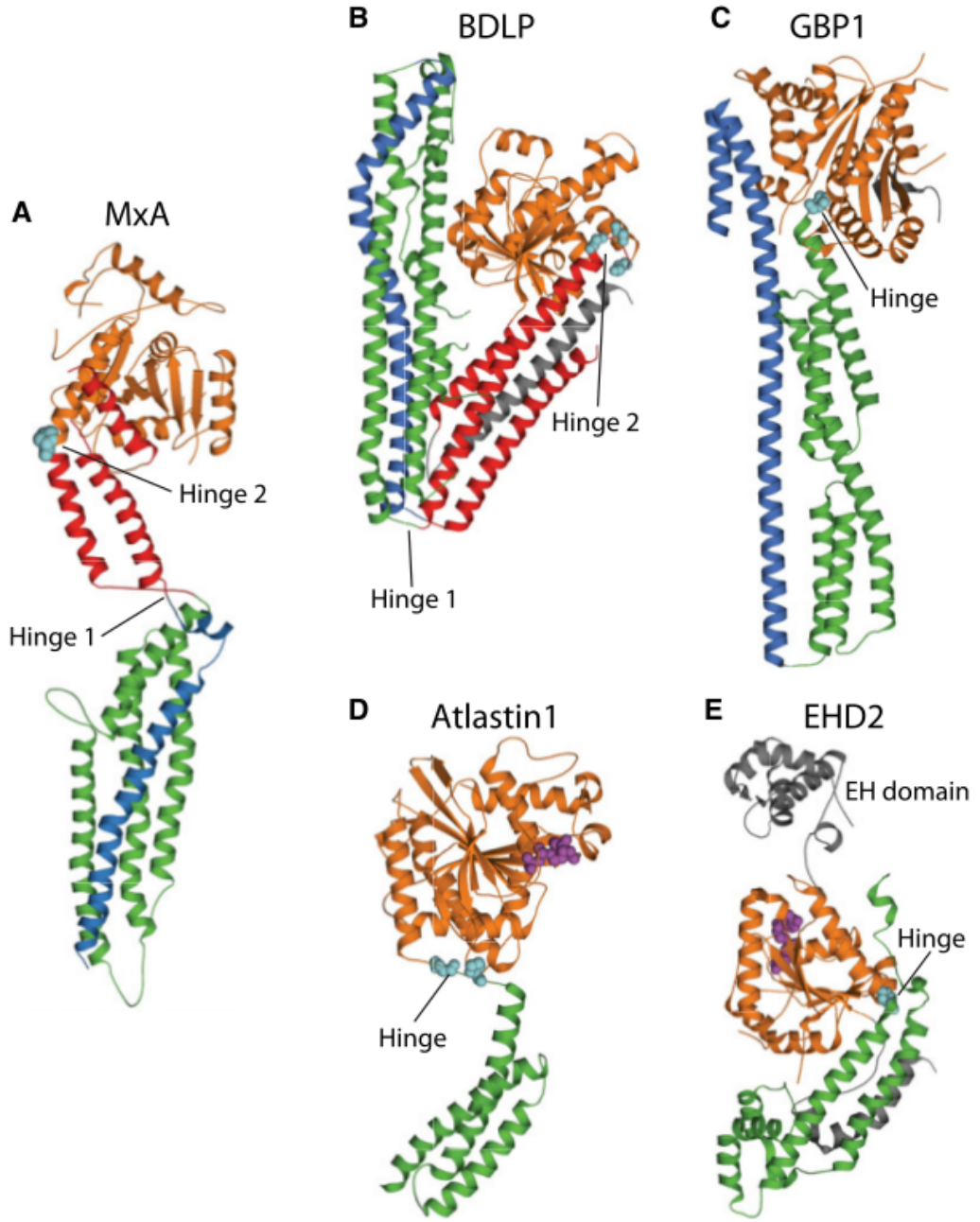

Figure 16: Structural comparison of dynamin superfamily members. Structural comparison of MxA (A) with nucleotide-free BDLP (PDB accession code 2J69) (B), nucleotide-free GBP1 (1DG3) (C), GDP-bound atlastin1 (3Q5D) (D), and EHD2 in the presence of a nonhydrolyzable ATP analog (2QPT) (E). G domains are colored in orange, stalk-like structures in green (derived from the middle domain) and blue (derived from the GED), and the BSE in red. Prolines in the hinge regions are shown as cyan spheres, and nucleotides are shown in purple. A separate BSE is apparent only in MxA and BDLP, whereas a proline residue-containing hinge region is found in all structures. Figure and legend adapted from [133].

1.6 SCOPE OF THE THESIS

EHD2 belongs to the dynamin superfamily of mechano-chemical GTPases. It was therefore assumed that EHD2 undergoes major nucleotide and membrane dependent conformational changes, which might be a prerequisite for its membrane remodeling activity. The main aim of this thesis was to elucidate these conformational changes. In BDLP, a drastic conformational rearrangement was observed between the GDP- and GMP-PNP-bound forms [182]. The kinked conformation in the GDP-bound form rearranges into an elongated GMP-PNP-bound form in the presence of liposomes. This lead to the hypothesis that EHD2 might undergo similar conformational changes. Thus, structures of ADP-bound and nucleotide-free EHD2 should be determined to understand the conformational changes associated with nucleotide binding, hydrolysis and release in the EHD family.

Furthermore, I wanted to explore the structure of lipid bound EHD2. Structures of peripheral membrane proteins bound to membranes are difficult to study with conventional X-ray crystallography since liposomes cannot be incorporated into a crystal lattice. Thus, an alternative approach using electron paramagnetic resonance (EPR) was applied. I concentrated on the characterization of the N-terminus which was not included in the previously determined EHD2 crystal structure. In small GTPases of the Arf family, the N-terminus was shown to insert into the membrane in the GTP-bound form. Thus, I wanted to explore whether the N-terminus of EHD2 undergoes a similar transition. To this end, the N-terminus was first characterized in solution using a combination of EPR and X-ray crystallography. I then followed the structural transitions of the N-terminus upon membrane binding. Therefore, changes in mobility of the N-terminal residues upon membrane binding were monitored using continuous wave EPR spectra. To discriminate between indirect and direct membrane interaction, EPR accessibility measurements were employed. The N-BAR protein endophilin requires its N-terminus to form stable and regular tubular coats. I wanted to check, if EHD2 also requires its N-terminus for stable and regular tube formation. Therefore, I used negative stain electron microscopy to compare the morphology of membrane tubules decorated with wild-type EHD2 or a variant lacking the N-terminus. Additionally, the residence time of N-terminally truncated EHD2 on caveolae was compared to wild-type EHD2. It was unknown, if the N-terminus is required for ATP-dependent membrane remodeling. Therefore, the liposome-stimulated ATPase rate of N-terminal EHD2 mutants was compared to the rate of wild-type EHD2. The membrane deforming potential of EHD2 was measured by leakage assays. Using these methods, the membrane remodeling activity of different EHD2 variants and its dependence on nucleotides was determined.

EHD2 was recently shown to reside on caveolae, as was the BAR-domain containing protein PACSIN2. To understand the reciprocal relationship of EHD2

and PACSIN2, this interaction was biochemically characterized. Using isothermal titration calorimetry (ITC), the domains and motifs responsible for this interaction were determined. It was unclear, how EHD2 is recruited to caveolae. Therefore, EHD2 variants, including one lacking the EH domain, were tested for co-localization with caveolae. Previously, the EH domain was suggested to move from the top position to a side position. I structurally characterized the side position and analyzed the impact of this movement on the residence time of EHD2 on caveolae.

2

MATERIALS AND METHODS

2.1 MATERIALS

2.1.1 *Instruments*

Instruments used in this thesis are listed in Appendix A, Table 11.

2.1.2 *Chemicals*

Chemicals were purchased from Sigma-Aldrich (St. Louis, USA), Carl Roth (Karlsruhe, D), Jena Bioscience (Jena, D), GE Healthcare (Piscataway, USA), life technologies (Carlsbad, USA) and Avanti Polar Lipids (Alabaster, USA).

2.1.3 *Enzymes*

Enzymes used in this thesis are listed in Appendix A, Table 12.

2.1.4 *Kits*

Kits used in this thesis are listed in Appendix A, Table 13.

2.1.5 *Bacteria strains*

- *E. coli* TG1 K12, genotype *supE, hsdΔ 5, thi, Δ(lac-proAB), F'[traD36, proAB$^+$, lac^q, lacZΔ M15* (Promega, Mannheim, D)
- *E. coli* Rosetta 2 (DE3), genotype *F$^-$ ompT hsdsSB (rB$^-$ mB$^-$) gal dcm (DE3)* pRARE (CmR) (Novagen, Darmstadt, D) with *pRARE* containing the tRNA genes *argU, argW, ileX, glyT, leuW, proL, metT, thrT, tyrU and thrU* and Cam^R

2.1.6 *Plasmids*

- pGEX-6P-1 (Amp^R, GE Healthcare, Piscataway, USA)

- pSKB2-LNB (Kan^R, based on pET28, Merck, Darmstadt, D; MCS exchanged against MCS from pGEX-6P-1, PreScission Protease cleavage site, O. Daumke, MDC Berlin)
- pEGFP-C3-MCS (Kan^R, based on pEGFP-C3, Clontech, Mountain View, USA; MCS exchanged against MCS from pGEX-6P-1, O. Daumke, MDC Berlin)
- pCMV-Myc (Amp^R, Clontech, Mountain View, USA)

2.1.7 *Media and Buffers*

Media used in this thesis and their composition/ordering numbers are listed in Appendix A, Table 14. Buffers and their composition are shown in Appendix A, Table 15.

2.2 MOLECULAR BIOLOGY

2.2.1 *Polymerase Chain Reaction*

DNA fragments were amplified with *Pfu* polymerase according to standard procedures [183].

2.2.2 *DNA restriction digest*

DNA was digested with restriction endonucleases (Type II) from New England Biolabs (NEB, Frankfurt am Main, D) according to the manufacturer's protocol.

2.2.3 *Agarose gel electrophoresis*

0.8 % agarose gels were prepared and run according to standard procedures [183].

2.2.4 *DNA purification*

Excised DNA bands were purified using the QIAquick Gel Extraction Kit (Qiagen, Hilden, D) according to the manufacturer's protocol.

2.2.5 *Ligation*

Concentration of plasmids and inserts was determined using the absorption at 260 nm. 10 ng plasmid and a six-fold molar excess of insert were ligated using T4 DNA Ligase from NEB according to the manufacturer's protocol.

2.2.6 *Preparation of chemically competent E. coli cells*

Chemically competent *E. coli* bacteria were prepared according to [184].

2.2.7 *Transformation of chemically competent E. coli cells*

Plasmids were transformed using the heat shock method according to standard protocols [183]. *E. coli* TG1 strain was used for plasmid propagation and *E.coli* Rosetta 2 (DE3) strain for protein expression.

2.2.8 *Storage of E. coli cells*

For long-term storage of bacteria, 1 mL of a 5 mL LB overnight bacterial culture was mixed with 0.5 mL sterile glycerol and stored at -80 °C.

2.2.9 *Site-directed mutagenesis*

Site-directed mutagenesis was carried out by QuickChange (Agilent Technologies, Santa Clara, USA) according to the manufacturer's protocol.

2.2.10 *Constructs*

An overview of the constructs used in this thesis can be found in Appendix A, Table 16.

2.3 PROTEIN EXPRESSION AND PURIFICATION

2.3.1 *Antibiotics*

Ampicillin was used at a final concentration of 100 µg/mL. Chloramphenicol was used at a final concentration of 34 µg/mL. Kanamycin was used at a final concentration of 10 µg/mL in liquid cultures and at 50 µg/mL in agar plates.

2.3.2 *24-well protein over-expression and solubility test*

Over-expression and solubility of desired constructs were tested in 1 mL auto induction medium (AIM) containing respective antibiotics in 24-well format. In each well a *E. coli* Rosetta 2 (DE3) single colony containing the respective plasmid was incubated at 37 °C, 750 rpm for 7.5 h, followed by 16 h at 20 °C, 750 rpm.

As expression levels may vary among subclones, 4 subclones per construct were tested. 300 µL of bacterial culture were centrifuged for 5 min at 13,200 rpm, room temperature (RT) and the pellet was resuspended in 120 µL cell disruption buffer (resuspension buffer with lysozyme, L6876, Sigma-Aldrich, St. Louis, USA). A sample of the crude extract (3 µL cell suspension, 17 µL cell disruption buffer and 20 µL 2 x SDS sample buffer) and a sample of the soluble fraction (20 µL of the supernatant after centrifugation of the cell suspension for 10 min at 13,200 rpm, 4 °C and 20 µL 2 x SDS sample buffer) were boiled for 10 min and subjected to SDS-PAGE.

2.3.3 *Small scale protein over-expression and solubility test*

To test the ability of the protein to bind the Immobilized Metal Ion Affinity Chromatography (IMAC) material 1 L TB medium supplemented with the respective antibiotics was inoculated 1:100 with an overnight *E. coli* Rosetta 2 (DE3) culture in LB medium. Cells were grown under shaking to an OD_{600} of 0.4 at 37 °C in buffled flasks. Bacterial cultures were cooled to 18 °C, protein expression was induced by addition of 40 µM isopropyl β-D-1-thiogalactopyranoside (IPTG) and cultures were grown for another 20 h.

Bacteria were collected by centrifugation at 5,500 rpm for 15 min in a JLA-8.1000 rotor and pellets were resuspended in 20 mL resuspension buffer per pellet from 1 L bacterial culture. The suspension was passed at least twice through a microfluidizer to disrupt the bacterial cells. The lysate was centrifuged at 35,000 rpm, 4 °C for 35 min in an Optima L-100 K ultracentrifuge using a 45Ti rotor. The supernatant was filtered through a 0.2 µm filter and applied on a 1 mL GSTrap HP or HisTrap HP chromatography column equilibrated with 5 column volumes (CV) equilibration buffer. The column was washed with 30 CV washing buffer and bound protein was eluted with 5 mL elution buffer. Samples taken at every step of the test purification were analyzed using SDS-PAGE (see 2.4.2).

2.3.4 *Large scale protein over-expression*

10 L TB medium supplemented with the respective antibiotics were 1:100 inoculated with an overnight *E. coli* Rosetta 2 (DE3) culture in LB medium containing the expression constructs. Cells were grown to an OD_{600} of 0.4 at 37 °C, 95-115 rpm. Bacterial cultures were cooled to 18 °C, protein expression was induced by addition of 40 µM IPTG and cultures were grown for another 20 h. Cells were collected by centrifugation at 5,500 rpm for 15 min in a JLA-8.1000 rotor and pellets were resuspended in 20 mL resuspension buffer per pellet from 1 L bacterial culture. The cell suspension was stored at -20 °C.

2.3.5 *Over-expression of selenomethionine- (SeMet-) derivatized protein*

To produce SeMet-labeled protein, M9 minimal medium supplemented with the respective antibiotics was inoculated with an overnight LB culture of the respective expression clone in a 1:100 dilution. Cells were grown to an OD_{600} of 0.4 at 37 °C. Then, an amino acid supplement (L-lysine, L-phenylalanine, L-threonine to a final concentration of 100 mg/L, L-isoleucine, L-leucine, L-valine and L-SeMet to a final concentration of 50 mg/L) was added to inhibit endogenous methionine biosynthesis and trigger SeMet incorporation [185]. 15 min later the bacterial culture was cooled to 18 °C and protein expression was induced by the addition of 0.4 mM IPTG. Further growth and harvesting of the cells was conducted in the same way as for the native protein.

2.3.6 *E. coli cell lysis and preparation of soluble fraction*

The bacterial cell suspension was thawed on ice, stirred thoroughly and passed at least twice through a microfluidizer to disrupt the cells. The lysate was centrifuged at 35,000 g and 4 °C for 35 min in a Optima L-100 K ultracentrifuge using a 45Ti rotor. The supernatant was filtered through a 0.2 µm filter.

2.3.7 *GSH affinity chromatography and GST-tag cleavage*

All chromatographic procedures were conducted at 4 °C. The filtered supernatant was applied on a chromatography column loaded with 15 mL GSH Sepharose beads equilibrated with 5 CV of equilibration buffer. The column was washed with 2 CV equilibration buffer, followed by 20 CV washing buffer to remove protein contaminations (e.g. Hsp70) and 2 CV equilibration buffer. GSH sepharose beads were resuspended in 1 CV equilibration buffer and transferred to a 50 mL tube. 1 mg GST-PreScission protease was added to cleave the amino-terminal GST-tag during incubation for 15 min on a roller and for further 20 h at 4 °C without agitation.

Five amino acids, Gly-Pro-Leu-Gly-Ser, remained as cloning artifact at the N-terminus after proteolytic cleavage. The column was re-packed and cleaved recombinant protein was collected by eluting with equilibration buffer.

2.3.8 *NiNTA affinity chromatography and hexahistidine-tag cleavage*

All chromatographic procedures were conducted at 4 °C. The filtered supernatant was applied on a chromatography column loaded with 10 mL NiNTA Sepharose beads equilibrated with 5 CV equilibration buffer. The column was washed with

2 CV equilibration buffer, followed by 20 CV washing buffer to remove protein contaminations (e.g. Hsp70) and 2 CV equilibration buffer. Recombinant protein was eluted with elution buffer and 1 mg GST-PreScission protease was added to cleave the amino-terminal hexahistidine-tag during incubation for 20 h at 4 °C without agitation. Five amino acids, Gly-Pro-Leu-Gly-Ser, remained as cloning artifact at the N-terminus after proteolytic cleavage.

2.3.9 *Size-exclusion chromatography (SEC)*

The elution fraction from Section 2.3.7 or Section 2.3.8 was concentrated to 2 mL (see Section 2.3.10), and possible precipitate was removed by centrifugation for 10 min at 13,200 rpm, 4 °C.

The supernatant was applied on a pre-equilibrated Superdex 200 SEC column at a flow rate of 1-2 mL/min running with SEC buffer. The peak fractions containing the protein of interest were pooled and concentrated to approximately 35 mg/mL. GST-PreScission Protease present in elution fractions from Section 2.3.8 was removed by a GSTrap HP chromatography column before the UV-detector.

2.3.10 *Protein concentration*

Protein solutions were concentrated using Amicon centrifugal filter devices with a 50 kDa cutoff according to the manufacturer's protocol.

2.3.11 *Protein concentration determination*

Total protein content in lysates or mixed protein solutions were determined using the Bradford assay [186]. For purified proteins, concentration was determined by measuring E_{280} and calculated extinction coefficients [187].

2.3.12 *Protein storage*

Pooled, concentrated peak fractions from SEC were divided into 30 µL aliquots and flash-cooled by plunging them into liquid N_2. Aliquots were stored at -80 °C.

2.4 BIOCHEMISTRY

2.4.1 *Right Angle Light Scattering (RALS)*

A 100 µL protein sample at a concentration of 4 g/L in RALS buffer was injected on a Superdex 200 10/300 GL column, operated at 0.5 mL/min. Samples of

EHD2•ATPγS were measured in RALS buffer supplemented with 300 µM ATPγS. The Refractive Index (RI) and RALS signal was detected on a right angle light scattering photometer (Viscotek RImax, Malvern, Malvern, UK) installed after the UV detector of the fast protein liquid chromatography (FPLC) system. Data analysis was performed with the software package OmniSEC (Malvern, Malvern, UK).

2.4.2 *Sodium dodecyl sulfate polyacrylamide gel electrophoresis (SDS-PAGE)*

Proteins were separated on NuPAGE Novex 4-12 % Bis-Tris gels (life technologies, Carlsbad, USA) with 1x MES running buffer (life technologies, Carlsbad, USA) or 12 % polyacrylamid SDS gels with 1x SDS running buffer [183] in the Xcell Sure Lock system at 180 V until the bromophenol blue dye reached the bottom of the gel. Gels were stained with coomassie brilliant blue R-250 solution.

2.4.3 *Circular Dichroism (CD) Spectroscopy*

10 µM protein was transferred in CD buffer and a CD spectrum ranging from 260 nm to 180 nm was recorded. The strongest signal for α-helical content is observed at 222 nm. The melting temperature was determined by following the CD signal at 222 nm upon ramping the temperature from 4 °C to 94 °C with a speed of 1 °Cmin.

2.4.4 *Determination of ATP hydrolysis rate in the presence and absence of liposomes*

The single turnover ATPase rates of EHD2 constructs were determined in liposome buffer I containing 10 µM EHD2 and 1 g/L large uni-lamellar vesicles (LUVs, see Section 2.4.6) or an equal volume of liposome buffer II, incubated at 30 °C, 400 rpm. The ATP hydrolysis reaction was started by adding ATP at a final concentration of 100 µM. 25 µL samples were taken after 0 min, 15 min, 30 min and 60 min and flash-frozen in liquid N_2. The remaining ATP was determined on a high pressure liquid chromatography (HPLC) system equipped with a reversed-phase ODS-2 hypersil column equilibrated with HPLC buffer according to [188]. Runs were conducted at a flow rate of 1.5 mL/min. Denatured proteins were adsorbed at a nucleosil 100 C18 pre-column. Nucleotide peaks were detected by measuring E_{259}. The column was calibrated using standard nucleotide solutions at a concentration of 100 µM in SEC buffer and no nucleotide was observed in EHD2 preparations. The k_{obs} was derived by plotting the concentration of remaining ATP against the time and dividing the obtained slope by the concentration of EHD2.

2.4.5 *Isothermal titration calorimetry (ITC)*

ITC experiments were carried out at 10 °C in a VP-ITC at a protein concentration of 50 to 100 µM in the cell and at least 10-fold molar excess of ligand in the syringe. ATPγS was used in 20-fold molar excess. 8 µL injections were repeated every 280 s. Optimal binding conditions were achieved by supplementing the SEC buffer with 2 mM $MgCl_2$, 1 mM $CaCl_2$. Binding isotherms were fitted and a equilibrium dissociation constant was calculated using the MicroCal ORIGIN software.

2.4.6 *Liposomes*

Folch fraction I bovine brain lipids (Sigma-Aldrich, St. Louis, USA) were dissolved in 1:4 methanol:chloroform, dried under a gentle Ar stream and desiccated over night. Multi-lamellar vesicles (MLVs) at a final concentration of 4 g/L were obtained by hydrating 0.5 mg dried lipids in 125 µL liposome buffer II or 20 mM HEPES (pH 7.5), followed by 30 s sonication in a bath-sonifier. Small uni-lamellar vesicles (SUVs) were obtained by sonication of hydrated lipids with a tip-sonifier until the solution turned clear. Large uni-lamellar large vesicles (LUVs) were obtained by filtering MLVs in the mini-extruder 11 times with 800 nm pore-size polycarbonate membranes.

2.4.7 *Co-sedimentation Assay*

10 µM protein was mixed with 1 mg/mL Folch-LUV or the same volume of liposome buffer II in 50 µL liposome buffer I and incubated for 10 min at RT. The suspension was separated at 70,000 rpm (Beckman TLA-100) for 10 min at RT. Supernatant and pellet was analysed by SDS-PAGE. Liposome-bound protein co-sedimented with the liposome fraction, whereas unbound protein remained in the supernatant.

2.4.8 *Leakage Assay*

A fluorescent dye ANTS (8-aminonaphthalene-1,3,6-trisulfonic acid) and its contact quencher DPX (p-xylene-bis-pyridinium bromide) were incorporated into LUVs and leakage of the dye into the solution was followed by measuring fluorescence increase, induced by fluorescence de-quenching. 5 mg Folch fraction I bovine brain lipids were hydrated in 200 µL liposome buffer II containing 9 mM ANTS and 25 mM DPX, flash-frozen 5 times, extruded with 800 nm pore-size polycarbonate membranes and separated from outer vesicle dye/quencher mix-

ture on a 3 mL Sephadex G-100 column. Fluorescence increase was measured in 200 µL liposome buffer I containing 40 µg Folch-ANTS/DPX-LUVs and 20 µg (1.6 µM) EHD2 in the presence or absence of 1 mM ATP over 2 h and normalized against complete leakage caused by 1 % Triton X-100. Excitation wavelength was set to 353 nm, 5 nm slit and emission wavelength was set to 520 nm, 10 nm slit. Data points were recorded every min with high PMT sensitivity and an Averaging Time of 0.5 s on a fluorescence spectrophotometer (Cary Varian Eclipse). The assay was adapted from [189, 190].

2.4.9 *Monomer Exchange*

Determination of intra-oligomeric distances by electron paramagnetic resonance (EPR, see Section 2.5.4) on lipid templates required the dilution of spin-labeled dimers with unlabeled cysteine-less dimers. Therefore, it was crucial to estimate the monomer exchange rate. A Förster Resonance Energy Transfer (FRET) signal was observed after the formation of mixed dimers from donor and acceptor labeled dimers [191, 192].

The maleimide-activated Alexa 488 donor (A488, life technologies, Carlsbad, USA) was coupled to the single cysteine mutant EHD2 C96 (the two other internal cysteines were exchanged to serines). The maleimide-activated Alexa 555 acceptor (A555, life technologies, Carlsbad, USA) was coupled to the single cysteine mutant EHD2 L303C (the three internal cysteines were exchanged to serines). Dithiothreitol (DTT) was removed from protein stock solutions with a PD-10 desalting column according to the manufacturer's protocol. 100 µM dye were coupled to 10 µM mutant EHD2 in SEC buffer over night at 4 °C. To avoid precipitation, the 10 mM dye stock solution was diluted prior to incubation with protein. Excess dye was removed by dilution and concentration using 50 kDa MWCO centrifugal filter devices (see Section 2.3.10) and protein was separated from remaining uncoupled dye on a PD-10 desalting column. The dye-labeled protein eluted between 0.8 mL and 1.8 mL and was kept on RT for 20 min. Mixed dimer formation was initiated by mixing 0.1 g/L (1.8 µM) donor-labeled EHD2 C96, 0.1 g/L (1.8 µM) acceptor-labeled EHD2 L303C and 0.3 g/L BSA. A fluorescence decrease at the emission maximum of the acceptor dye correlated with increasing FRET and was recorded together with emission scans on a fluorescence spectrophotometer (Cary Varian Eclipse) with the following settings:

EMISSION SCANS: Excitation 494 nm with slit 5 nm, Emission 500 - 650 nm with slit 5 nm, Scan speed medium, PMT sensitivity medium

KINETICS: Excitation 494 nm with slit 5 nm, Emission 519 nm with slit 5 nm, Scan speed medium, PMT sensitivity medium, Averaging time 2 s, 12 h time course, data points every 15 min

The fluorescence intensity decrease was plotted against the time and the half-time for monomer exchange was derived from a first-order exponential fit:

$$f(t) = a + be^{-\lambda t} \qquad \text{and } t_{1/2} = \frac{\ln 2}{\lambda}$$

The mathematical derivation of this function can be found in Appendix B.

2.4.10 *Electron Microscopy*

Liposome deformation was monitored by transmission electron microscopy (TEM). A suspension of 2 g/L Folch-MLVs and 1 g/L (16 µM) EHD2 was incubated for 1 min at RT and spotted on a carbon-film stabilized, formvar-coated copper grid (FCF150-Cu, Electron Microscopy Sciences, Hatfield, USA). It was critical to equilibrate EHD2 on RT for 15 min prior mixing with MLVs. Grids were negative-stained by adding and immediately blotting 5 % uranylacetate, followed by 45 s incubation with 5 % uranylacetate and a final wash step with ddH_2O. Grids were air-dried and imaged at 4,000 x to 20,000 x magnification on a Zeiss EM910. Further methodological details can be found in [193].

2.5 ELECTRON PARAMAGNETIC RESONANCE (EPR)

EPR is a spectroscopic method and requires at least one paramagnetic spin label containing an unpaired electron present in the protein of interest. A short explanation of the theoretical background of EPR is attached as Appendix C.

In this thesis, a site-directed spin labeling (SDSL) approach was followed, where the spin label [1-oxy-2,2,5,5-tetramethyl-pyrroline-3-methyl]-methane-thiosulfonate (MTSL, Toronto Research Chemicals, North Yorck, CDN) was attached via a disulfide bond to a cysteine [194, 195]. Internal cysteines in EHD2 at positions 96, 138 and 356 were mutated to serines, generating a cysteine-less EHD2 mutant. Cysteine point mutations were introduced at chosen positions using site-direct mutagenesis (see Section 2.2.9 and mutants expressed and purified as described under Section 2.3).

2.5.1 *Spin Labeling*

Prior to spin labeling DTT was removed from single and double cysteine mutants of EHD2 using PD-10 desalting columns with SEC buffer lacking DTT. MTSL was added in 5-fold molar excess to the protein and incubated at 4 °C overnight. The un-reacted spin label was removed using PD-10 columns and the spin labeled proteins were stored at -80 °C.

2.5.2 *Continuous Wave*

Continuous Wave (CW) EPR spectra of both solution and SUV bound EHD2 single mutants were recorded on a X-band CW EPR spectrometer fitted with ER4119HS resonator at 12.7 mW incident microwave power. For solution EPR experiments, the spin labeled samples were directly filled into capillary tubes and EPR spectra were recorded. For vesicle bound EPR experiments, 50 µg of spin labeled protein was mixed with 1.5 mg Folch-SUV (1:30 (w/w) protein:lipid ratio, see Section 2.4.6) and incubated at RT for 20 min. Unbound protein was separated from SUV bound protein by ultra centrifugation (70,000 rpm, Beckman TLA-100) for 20 min at 22 °C. The pellet was resuspended in SEC buffer lacking DTT, filled into capillary tubes and EPR spectra were recorded. Information about the secondary structure of the particular spin-labeled residue could be derived by comparing its spectra with reference spectra from residues with known secondary structures.

2.5.3 *Power Saturation*

Power saturation experiments were performed on a X-band CW EPR spectrometer fitted with ER4123D dielectric resonator to obtain accessibilities to O_2 (from air, Π_{O_2}) and 10 mM NiEDDA (Π_{NiEDDA}). The contrast parameter Φ was calculated using the relationship $\Phi = \ln \frac{\Pi_{O_2}}{\Pi_{NiEDDA}}$ as described previously [196, 197].

Insertion depth calibration was carried out with unlabeled EHD2 mixed with Folch-SUV containing 1 % (w/w) of spin-labeled lipids. For position 0 1,2-dipalmitoyl-*sn*-glycero-3-phospho(tempo)choline (gift from Kyoung Joon Oh), for position 5, 7, 10 and 12 the respective 1-palmitoyl-2-stearoyl-(*n*-doxyl)-*sn*-glycero-3-phosphocholine (Avanti Polar Lipids, Alabaster, USA) was used. Each spin label position corresponds to an insertion depth [196]. The Φ-values obtained from the depth calibration were fitted with a polynomial regression $y = 0.0063x^2 + 0.0249x + 0.0881$ (see Figure 28 B). Subsequently, experimental Φ values were converted into insertion depths (see Figure 28 A, right scale).

2.5.4 *Pulsed EPR distance measurements*

Spin labeled double cysteine mutants were used for distance measurements. The sample was mixed with cysteine-free EHD2 in a 1:1 (w/w) ratio to reduce background and with 15 – 20 % sucrose as a cryoprotectant. Measurements were conducted in quartz capillaries at 78 K. Four pulse double electron electron resonance (DEER) [198] experiments were performed on a X-band pulse EPR spectrometer fitted with a 3 mm split ring (MS-3) resonator, a continuous-flow helium

cryostat (CF935, Oxford Instruments, Abingdon, UK), and a temperature controller (ITC503S, Oxford Instruments, Abingdon, UK). The data were fitted using Tikhonov regularization [199] as implemented in DeerAnalysis2011[1] [200].

2.5.5 *Position of L5R1*

The position of the N-terminus and particular of residue Leu5 was determined by the distance relationship of 4 anchoring points in the helical domain, namely L28C, L294C, L303C and Y313C. A set of 4 double mutants L5C-L28C, L5C-L294C, L5C-L303C, L5C-Y313C was labeled (see Section 2.5.1) and analyzed by DEER (see Section 2.5.4).

The conformation of R1 and thus the putative position of the paramagnetic spin label at the anchoring points in the context of the crystal structure was modeled with MMM 2011[2] [201] or PRONOX[3] [202].

The position of residue L5R1 coincides with the intersection of 4 spheres, which are defined by the spin label positions at the anchoring points as midpoints and the distances determined by DEER as radii. The intersection was calculated with the following Python[4] script (requires the packages NumPy and SciPy), written by Gregor Moenke from the group of PD Dr. Martin Falcke:

```
#!/usr/bin/python
from math import *
from sys import *
from scipy.optimize import fsolve
from scipy.optimize import fmin

## input 4 spheres, midpoints from 120118-mean-weighted-position.ods, radii
    from DEER experiments

p1=[46.546,-36.472,-20.081]
r1=28

p2=[37.744,-40.334,-25.341]
r2= 27

p3=[26.850,-34.206,-18.324]
r3=33

p4=[29.099,-13.308,-22.228]
r4=48
```

1 http://www.epr.ethz.ch/software/index
2 http://www.epr.ethz.ch/software/index
3 http://rockscluster.hsc.usc.edu/research/software/pronox/pronox.html
4 http://www.python.org

```
## define functions

# guess location of intersection
def d(vec):
    return [
        (vec[0]-p1[0])**2 + (vec[1]-p1[1])**2 + (vec[2]-p1[2])**2 - r1**2,
        (vec[0]-p2[0])**2 + (vec[1]-p2[1])**2 + (vec[2]-p2[2])**2 - r2**2,
        (vec[0]-p4[0])**2 + (vec[1]-p4[1])**2 + (vec[2]-p4[2])**2 - r4**2,
        (vec[0]-p3[0])**2 + (vec[1]-p3[1])**2 + (vec[2]-p3[2])**2 - r3**2
        ]
# permutate all 4 sphere-functions
# sphere 1, 2 and 3
def d1(vec):
    return [(vec[0]-p1[0])**2 + (vec[1]-p1[1])**2 + (vec[2]-p1[2])**2 - r1
        **2,
            (vec[0]-p2[0])**2 + (vec[1]-p2[1])**2 + (vec[2]-p2[2])**2 - r2
                **2,
            (vec[0]-p3[0])**2 + (vec[1]-p3[1])**2 + (vec[2]-p3[2])**2 - r3
                **2]
# sphere 1, 2 and 4
def d2(vec):
    return [(vec[0]-p1[0])**2 + (vec[1]-p1[1])**2 + (vec[2]-p1[2])**2 - r1
        **2,
            (vec[0]-p2[0])**2 + (vec[1]-p2[1])**2 + (vec[2]-p2[2])**2 - r2
                **2,
            (vec[0]-p4[0])**2 + (vec[1]-p4[1])**2 + (vec[2]-p4[2])**2 - r4
                **2]
# sphere 1, 3 and 4
def d3(vec):
    return [(vec[0]-p1[0])**2 + (vec[1]-p1[1])**2 + (vec[2]-p1[2])**2 - r1
        **2,
            (vec[0]-p3[0])**2 + (vec[1]-p3[1])**2 + (vec[2]-p3[2])**2 - r3
                **2,
            (vec[0]-p4[0])**2 + (vec[1]-p4[1])**2 + (vec[2]-p4[2])**2 - r4
                **2]
# sphere 2, 3 and 4
def d4(vec):
    return [(vec[0]-p2[0])**2 + (vec[1]-p2[1])**2 + (vec[2]-p2[2])**2 - r2
        **2,
            (vec[0]-p3[0])**2 + (vec[1]-p3[1])**2 + (vec[2]-p3[2])**2 - r3
                **2,
            (vec[0]-p4[0])**2 + (vec[1]-p4[1])**2 + (vec[2]-p4[2])**2 - r4
                **2]

l = fsolve(d,[0,0,0,0],xtol=1.e-11)#[:2]
```

```
l1=fsolve(d1,l[:3])
l2=fsolve(d2,l[:3])
l3=fsolve(d3,l[:3])
l4=fsolve(d4,l[:3])

print
print "Schwerpunkt:"
S=[1/4.*(l1[0]+l2[0]+l3[0]+l4[0]),1/4.*(l1[1]+l2[1]+l3[1]+l4[1]),1/4.*(l1[2]+
    l2[2]+l3[2]+l4[2])]
print S
print
print "Fehlerquadrate je Punkt:"
print d(S)
```

2.6 CRYSTALLOGRAPHY AND STRUCTURE DETERMINATION

2.6.1 *Protein crystallization*

Before crystallization, proteins were diluted to 20 mg/mL with SEC buffer. Magnesium chloride and nucleotides in highest purity were added to a final concentration of 4 mM and 2 mM, respectively. Crystallization conditions from [164] were optimized by varying the buffer substance and the pH-value and screening different precipitants. Crystallization attempts for EHD2 Q410A in the ADP-bound form were performed in hanging drop vapor-diffusion 24 well setups. The reservoir contained 0.5 mL solution and crystallization drops were composed of 2 µL EHD2 Q410A•ADP and 2 µL reservoir solution. The crystallization attempts for EHD2 L5M Q410A in the AMP-PNP- and ADP-bound form were performed in sitting drop vapor-diffusion 96 well setups. The reservoir contained 80 µL solution and crystallisation drops were composed of 300 nL EHD2 L5M Q410A•nucleotide and 300 nL reservoir solution. All crystallization attempts were carried out at 4 °C.

Single crystals of EHD2 Q410A in the ADP-bound form grew in 100 mM HEPES pH 8.0, 20 mM $MgCl_2$, 8 % PEG 3350, 7 % 2-Methylpentane-2,4-diol (MPD). Crystals were prepared for cryo-cooling by a brief transfer to 50 mM MES (pH 6.4), 75 mM NaCl, 4 mM $MgCl_2$, 2 mM nucleotide, 14 % MPD, followed by a brief transfer to the same cryo condition containing 27 % MPD and finally flash-frozen in liquid nitrogen.

SeMet-derivatized EHD2 L5M Q410A in the AMP-PNP-bound form crystallized in 100 mM MES pH 6.5, 20 mM $MgCl_2$, 4 % PEG 3350, 5 % MPD. Crystals were cryo-cooled as described for EHD2 Q410A in the ADP-bound form. SeMet-derivatized EHD2 L5M Q410A in the ADP-bound form crystallized in 100 mM

MES pH 7.0, 20 mM $MgCl_2$, 6 % PEG 2000 MME, 5 % MPD. Crystals were cryo-cooled as described for EHD2 Q410A in the ADP-bound form.

2.6.2 *Data collection*

Datasets of single crystals were recorded using the rotation method with a ϕ increment of 1° (EHD2 L5M Q410A•nucleotide) or 0.5° (EHD2 Q410A•ADP) at a temperature of -173 °C. The MD2 microdiffractometer at Beamline 14.1, BESSY II, Berlin, Germany, was used with a Rayonics MX-225 CCD detector, except for the EHD2 Q410A•ADP crystal, for which a dataset was recorded at the Beamline PX06SA, SLS, Villigen, Switzerland, equipped with a high resolution diffractometer and a Pilatus 6M detector. A fluorescence scan of SeMet-derivatized EHD2 L5M Q410A•nucleotide crystals was conducted using a Bruker AXS/Roentec X-ray fluorescence detector. Peak energy for the SeMet-derivatized EHD2 L5M Q410A•nucleotide crystals was determined as 12.6555 keV with f′ and f″ values of -7.38 and 4.68 for the AMP-PNP bound form, and 12.6550 keV and f′ and f″ values of -8.96 and 6.43 for the ADP-bound form. Initial indexing and determination of an optimal data collection strategy was done using iMOSFLM [203]. Recorded intensities were integrated and scaled with the program XDS [204].

2.6.3 *Protein structure solution*

Unit cell constants and symmetry of the new datasets were identical to the dataset of EHD2 Q410A•AMP-PNP [164]. Therefore, all structures were solved using the coordinates of EHD2 Q410A in the AMP-PNP bound form (PDB Code: 2QPT) as a template. SeMet-substituted crystals were isomorphous to the native crystals but diffracted X-rays to slightly higher resolution. A single anomalous dispersion (SAD) protocol was applied to obtain improved phases as implemented in the program autoSHARP [205]. 15 out of 16 selenium sites were identified.

2.6.4 *Atomic model building and refinement*

Stretches of missing atomic models were built and fitted into electron density maps using the program Coot [206]. Iterative cycles of TLS refinement (translation, libration and screw-rotation, [207]) and restrained refinement were carried out with Refmac5 [208]. To allow cross validation for all structures, the test set was inherited from the dataset of EHD2 Q410A in the AMP-PNP bound form (PDB Code: 2QPT). The N-terminus (residues 1-7) and additional residues at the KPFxxxNPF loop were built using the intensities and phases from the SeMet-derivatized dataset without solvent flattening.

2.6.5 *Protein structure validation and alignment*

All-atom contacts and geometry of the atomic models were evaluated using the Molprobity server [209]. Amino acid sequences were aligned using ClustalW [210, 211].

2.7 EUKARYOTIC CELL BIOLOGICAL METHODS

The cell biological work was performed in cooperation with the group of Dr. Richard Lundmark, Umeå University, Medical Biochemistry and Biophysics, Umeå, Sweden.

2.7.1 *Fluorescence recovery after Photobleaching (FRAP)*

N-terminal GFP-tagged EHD2 wild-type and N-terminal variants of EHD2 were overexpressed together with Cav1-RFP in 3T3-L1 cells and were bleached for 10 seconds with 100 % laser power in the 488nm and 568nm channel. Recovery was measured over 10 minutes. At certain timepoints the percentage of recovery was calculated.

3

RESULTS

3.1 SAMPLE PREPARATION

Most experiments required a high amount of pure protein. Bacterial expression clones were used as described previously [164], and new constructs were obtained by standard cloning procedures (Section 2.2). EHD2 variants optimized for crystallization were generated, as well as over 60 single and double cysteine-mutants for experiments requiring labeled protein. For such experiments, the internal cysteines had to be replaced by serines, resulting in a cysteine-less background. PACSIN2 interaction studies required different PACSIN2 variants.

Proteins expressed from the plasmid pSKB2-LNB resulted in N-terminal hexahistidine-tag fusions, whereas proteins expressed from the plasmid pGEX-6P-1 resulted in N-terminal GST-tag fusions. Both types of fusion proteins contained a PreScission Protease cleavage site and a 7 to 9 residue long linker between the tag and the insert.

New constructs were tested for expression and solubility as described in Section 2.3.2 and Section 2.3.3. Positively tested constructs were purified as exemplified here on hexahistidine-tagged EHD2 and as described in Section 2.3.4 - Section 2.3.12. Samples for SDS-PAGE (Section 2.4.2) were taken at different purification steps. His-EHD2 was separated from *E. coli* contaminants by affinity chromatography. With size exclusion chromatography (SEC), remaining contaminants were removed and the protein was transferred in SEC buffer. Enrichment of EHD2 over the course of the purification process to almost homogeneity was observed (Figure 17). The typical yield of an EHD2 preparation varied between 5 and 20 mg purified protein per 12 L TB culture. Purification of GST-tagged PACSIN2 yielded 50 mg PACSIN2 per 5 L TB culture with almost no contaminants.

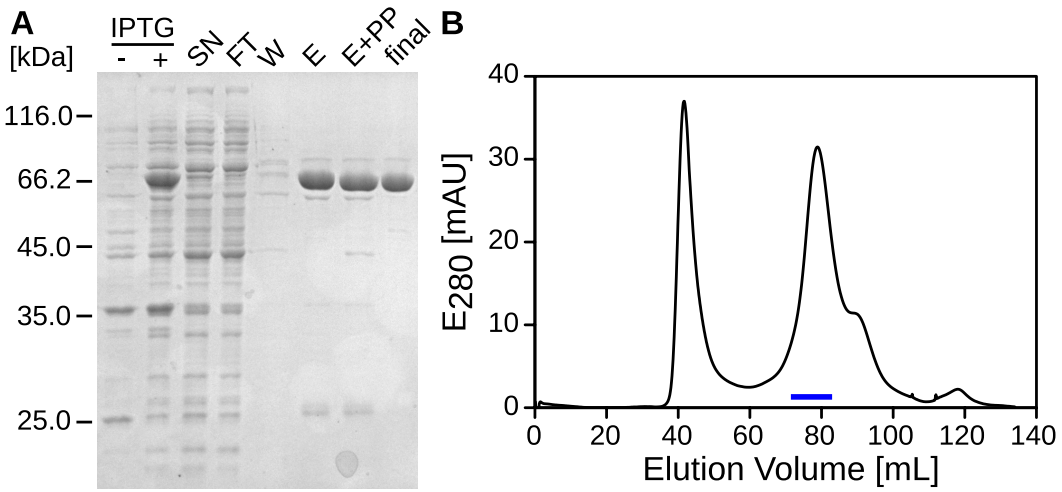

Figure 17: Typical EHD2 purification procedure. **A** 12 % SDS PAGE of various samples taken during the purification. -/+ IPTG, whole-cell bacteria lysates before and after induction; SN, supernatant of bacterial lysates after ultracentrifugation; FT, Flow-Through of NiNTA-sepharose column; W, wash fraction of the same column; E, imidazole eluate containing the EHD2 construct; E+PP, imidazole eluate after incubation with PreScission Protease, showing EHD2 after removal of the hexahistidine-tag, the GST-tagged protease and contaminants, which bind unspecifically to the column material; final, EHD2 after combining and concentrating the indicated fractions in B. **B** Superdex200 size-exclusion chromatogram. Fractions pooled and concentrated for further experiments are indicated.

3.2 THE ATPASE CYCLE OF EHD2

A possible mechano-chemical function of EHD2 could be explained best by revealing the complete ATPase cycle. The structure of EHD2 in the presence of the non-hydrolyzable ATP analogue AMP-PNP was solved previously by X-ray crystallography [164]. The structures of EHD2 in the ADP-bound and in the nucleotide-free state would reveal the complete ATPase cycle. To this end, the folding state and oligomerization state of EHD2 in the nucleotide-free and nucleotide-bound form was structurally and functional characterized.

3.2.1 *Determination of the folding state*

Crystallization requires natively folded proteins. Therefore the folding state of EHD2 in the nucleotide-free and in the ADP-bound form was analyzed by circular dichroism (CD) spectroscopy as described in Section 2.4.3. Spectra were truncated at 210 nm, because the Photo Multiplier Tube (PMT) voltage at wavelengths below 210 nm rose to very high values. The rise in the PMT voltage can be explained by interfering signal absorption by remaining Cl^- or HEPES molecules, or hardware limitations. Nevertheless, both spectra superimposed well between 260 nm and 225 nm, indicating that EHD2 in the nucleotide-free and ADP-bound form has a

similar fold. The local minimum in the spectrum of EHD2 at 222 nm indicates α-helical content, in line with the mainly α-helical structure of EHD2•AMP-PNP. The spectrum of EHD2•ADP shows a strong rise of the signal below 220 nm, probably caused by absorption of light by ADP (Figure 18 A). The melting point was 41 °C and 42 °C for EHD2 and EHD2•ADP, respectively (Figure 18 B). From the CD spectra, it can be concluded that the purified protein was properly folded and that ADP neither severely affects the overall folding of EHD2, nor the melting point.

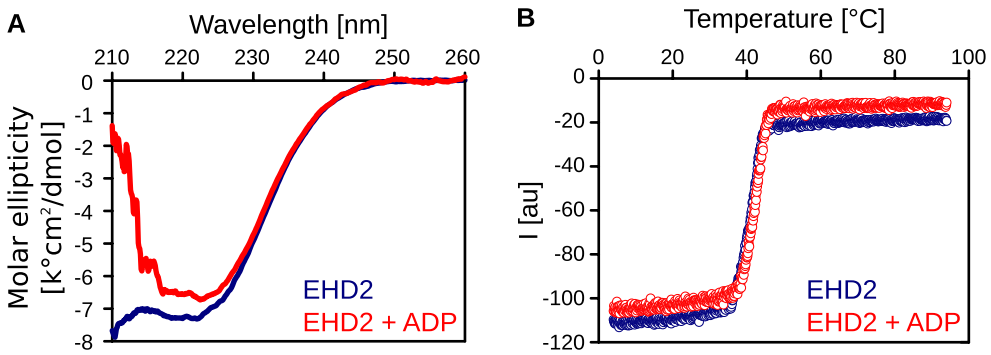

Figure 18: Analysis of EHD2 and EHD2•ADP by CD spectroscopy. **A** Superposition of the CD spectra of EHD2 wt in the absence or presence of 1 mM ADP. The spectra were truncated at 210 nm. The local minimum at 222 nm indicates α-helical content, suggesting proper folding of EHD2 wt and EHD2 wt•ADP. Buffer spectra were subtracted from the sample spectra. Addition of ADP did not alter the fold substantially. **B** Determination of the melting point of EHD2 in the absence or presence of 1 mM ADP. The signal intensity at 222 nm is plotted against the temperature. The melting point of 41 °C was elevated by 1 °C upon addition of ADP.

3.2.2 *Determination of the oligomeric state*

A monodisperse protein sample favors crystallization. Therefore the oligomeric state of EHD2 in solution in the absence or presence of ATPγS was analyzed. Right Angle Light Scattering (RALS) together with the Refractive Index (RI) determines the molecular weight (MW). In contrast, conventional SEC with an UV detector relates the hydrodynamic radius of the sample to radii from proteins with known MW. Thus, with RALS the MW is directly accessible, whereas with SEC the hydrodynamic radius is obtained. The experiment was performed as described in Section 2.4.1 with EHD2, in the absence and in the presence of ATPγS. In both cases the RI peak was observed at similar retention volumes. Interestingly, the MW distribution of EHD2 in the absence of nucleotide was inhomogeneous, whereas the MW distribution of EHD2 in the presence of ATPγS was homogeneous. This indicates that a monomer-dimer equilibrium for EHD2, and a stable dimer for EHD2•ATPγS was observed. Peak retention volumes and molecular

weights are summarized in Table 1 and the RI and MW were plotted against the retention volume in Figure 19. In conclusion, ATPγS-loaded EHD2 is monodisperse and might favor crystallization, whereas nucleotide-free EHD2 forms a monomer-dimer equilibrium which might counteract crystallization.

Table 1: Right Angle Light Scattering Data

	EHD2	EHD2•ATPγS
Peak Retention Volume [mL]	13.70	13.75
MW [kDa]	108.6	118.6

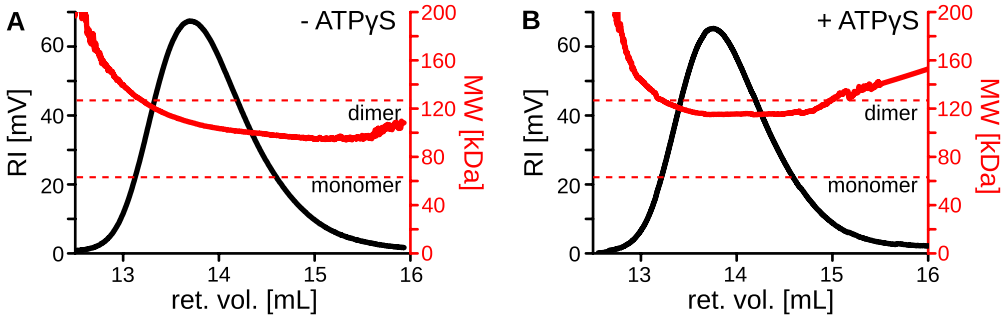

Figure 19: The oligomeric state of EHD2 in solution was determined by Right Angle Light Scattering (RALS). **A** Refractive Index (RI) and molecular weight (MW) of EHD2 and **B** EHD2•ATPγS plotted against the Retention Volume. A monomer-dimer equilibrium in the absence of nucleotide, and a stable dimer in the presence of ATPγS was observed.

3.2.3 *Structure of EHD2 in the ADP-bound form*

The ADP-bound structure of EHD2 is required for the elucidation of the ATPase cycle of EHD2. Therefore, crystallization trials with ADP-bound EHD2 were carried out. Tetragonal crystals of EHD2 Q410A•ADP grew after 4 days and a dataset from a single crystals was recorded (Figure 20, Table 2, Section 2.6). The dataset was isomorphous to the dataset of EHD2•AMP-PNP (PDB Code: 2QPT) and molecular replacement was used to solve the phase problem of ADP-bound EHD2. Alternating manual model building with TLS and restrained refinement lead to final R-values of R_{work} = 30 % and R_{free} = 25 %. The refinement statistics are summarized in (Table 3).

The ADP-bound EHD2 structure resembled the EHD2•AMP-PNP structure, exhibiting an N-terminal helical patch, followed by the G domain, the helical domain, a flexible linker and the EH domain. Comparing switch I in the AMP-PNP- and ADP-bound structures revealed that in the latter case, switch I moved out of the nucleotide binding pocket, adopting a more relaxed conformation (Figure 21). The structures of EHD2 in the ADP- and AMP-PNP-bound form aligned

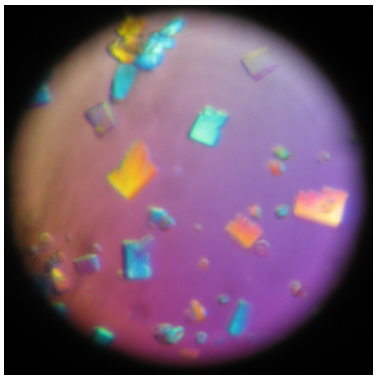

Figure 20: EHD2•ADP Q410A crystals could be fished with 0.1 - 0.2 mm loops.

with an rmsd of 0.46 Å. Taken together, no substantial conformational changes were observed between the two different nucleotide loading states. This indicates that nucleotide hydrolysis does not provide a mechanical force, which is observable by X-ray crystallography. Other mechanisms causing membrane remodeling were taken into account, including the possibility that conformational changes occur after nucleotide release.

Table 2: Data collection statistics for EHD2•ADP.

DATA COLLECTION	EHD2 Q410A•ADP
Date	24.11.2008
Beamline	SLS PX06SA
Wavelength [Å]	0.9184
Temperature [K]	100
Space group	C2
Cell dimensions	
a [Å]	99.24
b [Å]	135.18
c [Å]	56.61
α [°]	90.0
β [°]	106.08
γ [°]	90.0
V_M [Å^3/Da] †	2.97
Resolution [Å] ‡	48 (3.28) - 3.2
No. of observed reflections	44528 (3127)
No. of unique reflections	11802 (849)
R_{obs} [%]	4.8 (56.9)
R_{meas} [%] §	5.6 (66.8)
I/σ(I)	18.49 (2.61)
Completeness [%]	99.2 (98.6)
Redundancy	3.8
Overall B-factor (Wilson) [Å^2]	81.9

† According to [212].
‡ Numbers in parentheses apply for the highest resolution shell.
§ According to [213].

Table 3: Refinement statistics for the EHD2•ADP structure.

REFINEMENT	EHD2 Q410A•ADP
Resolution [Å]	48 - 3.2
No. of reflections used	11216
R_{work}[†] / R_{free}[‡] [%]	25.6 / 30.1
No. of atoms	3798
Protein	3769
Nucleotide	27
Mg^{2+}	1
Ca^{2+}	1
Water	0
Averaged B-factor protein [Å^2]	96.7
RMSD	
Bond length [Å]	0.005
Bond angles [°]	0.890
Ramachandran Statistics	
Favored [%]	96.8
Outliers [%]	0.2

† $R_{work} = \frac{\sum |F_{obs} - F_{calc}|}{\sum |F_{obs}|}$

‡ R_{free} was calculated with the same set of test reflections as in 2QPT [164].

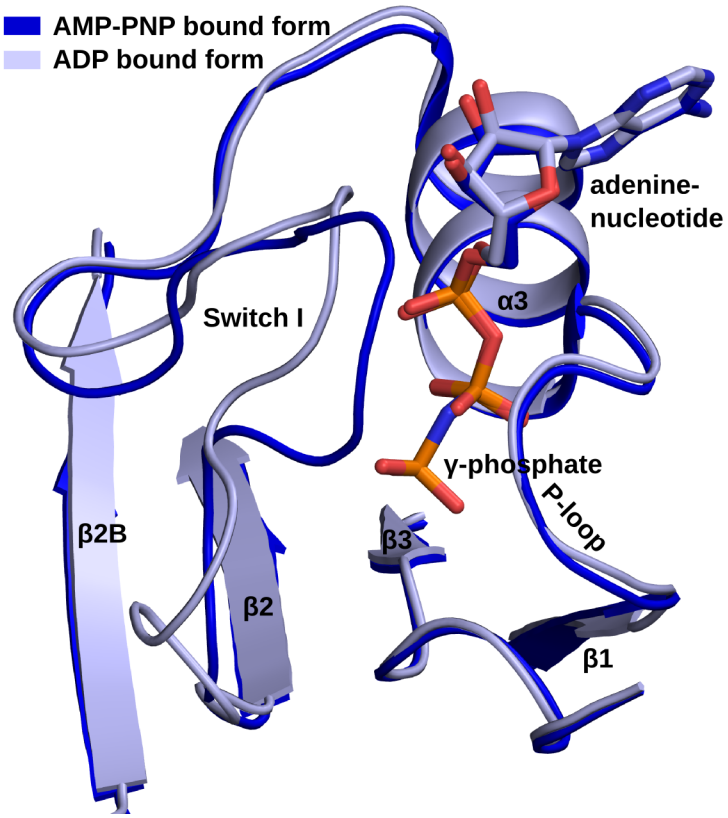

Figure 21: The nucleotide binding pocket of EHD2 in cartoon representation with important secondary structure elements and sequence motifs indicated. A superposition of EHD2•AMP-PNP (blue, PDB Code: 2QPT) and EHD2•ADP (lightblue) reveals slight conformational changes upon nucleotide hydrolysis. The switch I region between β-sheet 2 (β2) and α-helix 3 (α3) adopts a relaxed conformation in the ADP bound form.

3.2.4 *Crystallization trials of EHD2 in the nucleotide-free form*

Comparison of the ADP- and AMP-PNP-bound structures of EHD2 indicated that nucleotide hydrolysis does not trigger substantial conformational changes. However, EHD2 might adopt a different conformation in the nucleotide-free form. From a previous experiment, it was known that EHD2 is folded in the nucleotide-free form (Section 3.2.1).

Initial crystallization attempts with nucleotide-free EHD2 Q410A failed. Therefore, various constructs with enhanced crystal contacts were designed manually. Additionally, constructs with reduced surface entropy were designed with the help of the Surface Entropy Reduction prediction Server[1] (SERp) [214–216]. Those constructs were tested for expression and solubility according to Section 2.3.2 and Section 2.3.3.

Soluble constructs were subjected to crystallization trials in 96-well format (Section 2.6.1). The screen contained buffer at various pH, $MgCl_2$ and different precipitants (MPD, PEG 400, PEG 2000 MME, PEG 3350, PEG 8000, $(NH_4)_2SO_4$, NaCl, 2-propanol or malonate pH 7.1). Results from expression, solubility and crystallization trials are summarized in Table 4.

Furthermore, 96-well crystallization trials with EHD2 wild-type and the commercial screens PACT, PEG and PEGII diluted 1:2 and 1:10 with ddH_2O were performed. Stable degradation products with promising crystallization tendency might be obtained by limited proteolysis. However, the addition of a protease cocktail of trypsin and chymotrypsin to the crystallization screen did not yield stable degradation products suitable for crystallization.

In summary, no crystals from nucleotide-free EHD2 could be obtained with the indicated crystallization screens. A previous experiment revealed that ADP-bound EHD2, which crystallized successfully, was dimeric. In contrast, nucleotide-free EHD2 formed a monomer-dimer equilibrium, which might interfere with crystal formation.

1 http://services.mbi.ucla.edu/SER/

Table 4: Summary of crystallization attempts of nucleotide-free full-length mouse EHD2 constructs. For each construct overexpression (Exp), solubility (Sol) and crystallizability (Xtal) is indicated. n.d. - not determined

EHD2	EXP	SOL	XTAL
wild-type	yes	yes	no
Mutants predicted to form enhanced crystal contacts			
QR13,14YY, Q410A	yes	yes	n.d.
E91Y, Q410A	yes	yes	n.d.
VF321,322YY, K328A, Q410A	yes	yes	no
K375Y, K377YY, Q410A	n.d.	-	-
EDGEE432-437YYGYY, Q410A	yes	yes	n.d.
E518Y, Q410A	yes	yes	n.d.
QR13,14YY, E91Y, K328A, Q410A	n.d.	-	-
QR13,14YY, E91Y, K328A, K375Y, K377Y, Q410A	yes	yes	n.d.
QR13,14YY, E91Y, K328A, Q410A, E518Y	yes	yes	no
QR13,14YY, E91Y, K328A, K375Y, K377Y, Q410A, E518Y	yes	yes	n.d.
QR13,14YY, E91Y, VF321/322YY, K328A, K375Y, K377Y, Q410A, E518Y	yes	yes	n.d.
QR13,14YY, E91Y, K328A, Q410A, EDGEE432-437YYGYY, E518Y	yes	yes	n.d.
QR13,14YY, E91Y, K328A, K375Y, K377Y, Q410A, EDGEE432-437YYGYY, E518Y	yes	no	-
QR13,14YY, E91Y, VF321/322YY, K328A, K375Y, K377Y, Q410A, EDGEE432-437YYGYY, E518Y	n.d.	-	-
Mutants with reduced surface entropy			
EK119,120AA, Q410A	yes	yes	no
KKE315-317AAA, Q410A	n.d.	-	-
KENK324-327AANA, Q410A	yes	yes	no
EELE400-403AALA, Q410A	yes	yes	no
EEGSE435-439SSGSS, Q410A	yes	yes	no
KENK324-327AANA, EELE400-403AALA, Q410A	yes	yes	n.d.
KENK324-327AANA, EEGSE435-439SSGSS, Q410A	yes	yes	no

3.2.5 *Crystallization trials of isolated domains from the EHD family*

Crystallization of the multi-domain ATPase EHD2 in the nucleotide-free form was unsuccessful. However, the structure of the isolated G domain in different nucleotide loading states might help understanding the ATPase cycle of EHD2.

The structure of the isolated helical domain might provide new insights into the oligomerization mode, in a similar manner to the structure of the MxA-stalk [132].

In total, 24 His- or GST-tagged G domain and helical domain constructs from various species listed in Appendix A, Table 16 were tested for overexpression and solubility as described in Section 2.3.2. None of the constructs was soluble. Optimization of the G domain constructs with point mutations in the dimer interface, promoting a purely monomeric state, might be a promising strategy.

3.3 THE AMINO-TERMINUS OF EHD2 IS REQUIRED FOR MEMBRANE REMODELING

The N-terminal 16 residues could not be modeled in the ADP- and AMP-PNP-bound crystal structures, due to missing density or connectivity. Interestingly, these N-terminal residues of EHD proteins, in particular amino acids 2-9, are highly conserved (Figure 14). A multi-method approach including electron paramagnetic resonance (EPR), crystallography, negative-stain electron microscopy, leakage assays and cell biology was used to study the structural and functional properties of the N-terminal residues. EPR required a cysteine-less EHD2 mutant, with the three internal cysteins mutated to serine. Subsequently, amino acids 2-9 in this N-terminal stretch were individually replaced by a single cysteine. Labeling of the cysteine with a nitroxide spin label (1-oxyl-2,2,5,5-tetramethylpyrroline-3-methyl)methanethiosulfonate, MTSL) results in the side chain R1 (Section 2.5).

3.3.1 *The amino-terminus adopts two conformations in solution*

EPR continuous wave (CW) spectra provide information on the mobility of the spin label (Section 2.5.1, Section 2.5.2). Narrow, sharp lines indicate flexible spin labels, and distant, broad lines indicate immobile spin labels. Spectra of spin labels attached to single cysteine mutants of residues 2-9 were recorded in solution-state. The spectra were deconvoluted and the ratio between mobile and immobile components was determined. Surprisingly, the CW spectra showed mostly immobile components (Figure 22, Table 5), indicating an ordered stabilized state. This was unexpected and suggested that the N-terminus in solution occupies a defined position. A second, flexible state, as predicted from the absence of the first 18 amino-acids in the crystal structures, might be possible. Substitution of hydrophobic residues Phe2, Trp4, Leu5 with the cysteine-linked spin label resulted in higher fractions of mobile components, when compared to the other N-terminal amino acids. This points to a function of Phe2, Trp4, Leu5 in the stabilization of the N-terminus in solution.

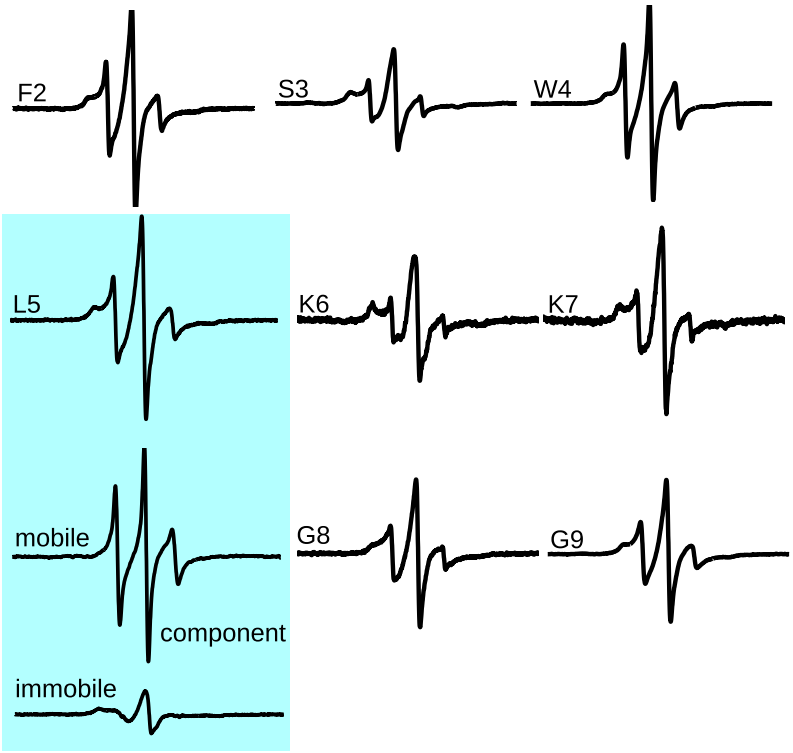

Figure 22: CW spectra of EDH2 residues 2-9 in solution. The immobile and mobile components of a spectrum was separated as shown for L5R1 in the blue area. Table 5 lists the fraction of mobile component for each spectrum.

Table 5: Fraction of mobile component in CW spectra of EHD2 residues 2-9 in solution.

MUTANT	MOBILE COMPONENT [%]
F2R1	26
S3R1	10
W4R1	33
L5R1	21
K6R1	10
K7R1	18
G8R1	10
G9R1	17

3.3.2 *Localization of the amino-terminus in solution*

The CW spectra suggested a defined position of the N-terminus in solution. In order to better understand the mechano-chemical function of EHD2, the spatial position of the N-terminus was determined by two independent experiments. With distance restraints obtained from EPR experiments the position of the N-terminus could be approximated. This position was corroborated by high-resolution crystallographic data.

3.3.2.1 *Determination of the approximate position of the amino-terminus*

To locate the position of the N-terminus in solution, pulsed EPR (double electron electron resonance, DEER) distance measurements were performed using EHD2 variants spin labeled at Leu5 and an additional residue in the helical domain (Figure 23, Section 2.5.4). Distances between residues 5-28, 5-294, 5-303 and 5-313 were between 27 Å and 48 Å. As a control, the distance between residues 28 and 303 within the helical domain was determined (Table 6). The nitroxide spin label can adopt various different conformations, leading to a positional ambiguity of roughly 7 Å. This makes it difficult to relate EPR distances to crystallographically determined distances. However, the possible positions of the spin labels in a crystal structure are sterically restricted. Using the PRONOX[2] [202] algorithm, the position of the spin labels in the crystal structure of EHD2 were determined. The control measurement between crystallographically defined positions resulted in a distance of 18 Å, which is consistent with the predicted distance in the crystal structure. In order to determine the location of Leu5, four spheres with the distances as radii were drawn around the predicted position of the spin labels (Figure 24). The distances intersected at a position close to the G domain, thereby defining the rough position of Leu5. A detailed explanation, how the position of L5R1 was calculated can be found in Section 2.5.5.

Table 6: Distances between the indicated positions measured by pulsed EPR are listed in column DEER. For comparison, the distances between the crystallographically determined position of Leu5 (see Section 3.3.2.3) and the spin-labeled residues in the helical domain are listed in column Crystal. The position of the spin labels was modeled using PRONOX.

DOUBLE MUTANT	DISTANCE [Å]	
	DEER	CRYSTAL
L5R1 - L28R1	28	33
L5R1 - L294R1	27	29
L5R1 - L303R1	32	20
L5R1 - Y313R1	48	39
L28R1 - L303R1	18	26

2 http://rockscluster.hsc.usc.edu/research/software/pronox/pronox.html

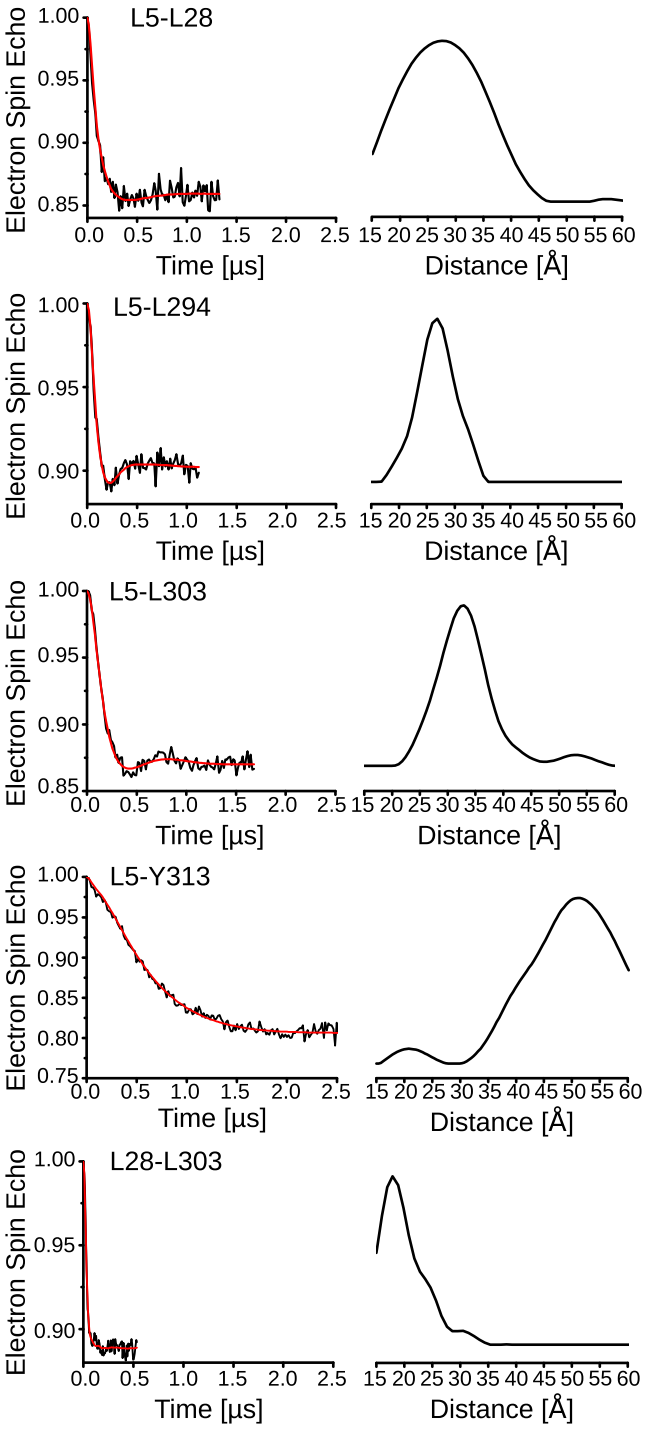

Figure 23: DEER raw data, fits and distance distributions for 5-28, 5-294, 5-303, 5-313 and 28-303. The 28-303 measurement served as control. The obtained distance corresponds well with the crystal structure.

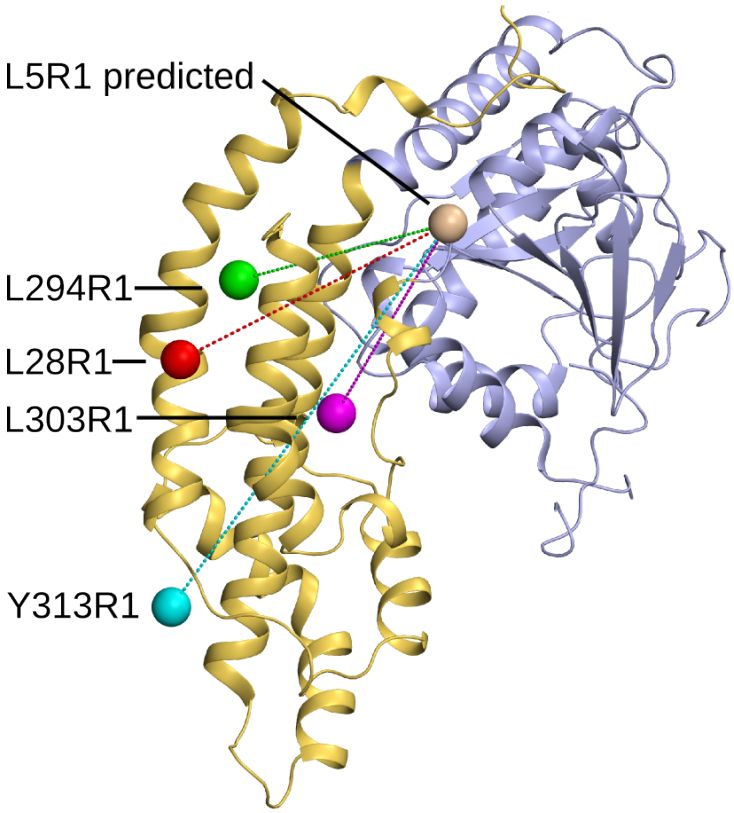

Figure 24: The colored spheres show the predicted positions of the spin labels as modeled by PRONOX. The position of L5R1 close to the G domain is the intersection of spheres drawn around the spin label positions as midpoints and the distances from Table 6 as radii.

3.3.2.2 *Determining distances by EPR in the oligomer*

Structural changes of EHD2 upon membrane binding cannot be observed by X-ray crystallography. EPR can be used theoretically to study the structure of membrane bound oligomers. In an oligomer, many spin labels would come into vicinity, leading to the measurement of several different distances. Therefore, spin labeled dimers are typically diluted with unlabeled dimers. As a prerequisite for distance measurements by EPR in the oligomer, the monomer exchange rate was determined.

Here, dimers were tested for monomer exchange and the exchange rate was determined. To this end, one single cysteine mutant was labeled with a donor dye (Alexa 488, A488) and another single cysteine mutant was labeled with an acceptor dye (Alexa 555, A555). Upon mixing the two labeled mutants, the Förster Resonance Energy Transfer (FRET) was followed (Section 2.4.9). If exchange occurs, the donor and acceptor dyes come into vicinity and a FRET signal can be detected. The reversibility of this process was tested by addition of a 5-fold molar excess of a cysteine-less EHD2 mutant, which should extinguish the energy transfer by formation of unlabeled or singly labeled dimers.

At time t_0 donor- and acceptor labeled EHD2 dimers were mixed and a fluorescence spectrum was recorded. 20 h later, at t_1, a second spectrum was recorded, showing a fluorescence intensity decrease at the donor emission wavelength 519 nm and a fluorescence intensity increase at the acceptor emission wavelength 568 nm. Addition of a 5-fold molar excess of unlabeled, cysteine less EHD2 and further incubation over 20 h (t_2) reverted the shape of the spectrum. Due to a loss of fluorescence intensity over time, the spectra in Figure 25 A were normalized to the area under the curve. In order to derive the exchange rate, the kinetics of the spectral changes were followed (Figure 25 B). The fluorescence decrease was fitted to a first-order exponential decay function with a half-time of $t_{1/2}$ = 184 min at room temperature.

The observed spectral changes at time t_0 and t_1 show that energy is transferred from the donor to the acceptor dye, indicating the formation of mixed dimers. Dimer formation was reversible, because the spectrum at time t_2 after addition of unlabeled, cysteine-less EHD2 resembles the spectrum at t_0. The monomer exchange rate presented here will allow the generation of lipid-bound EHD2 oligomers, where only one monomer of the dimer is labeled. Therefore it will will be possible to measure distances by EPR on oligomeric lipid-bound EHD2.

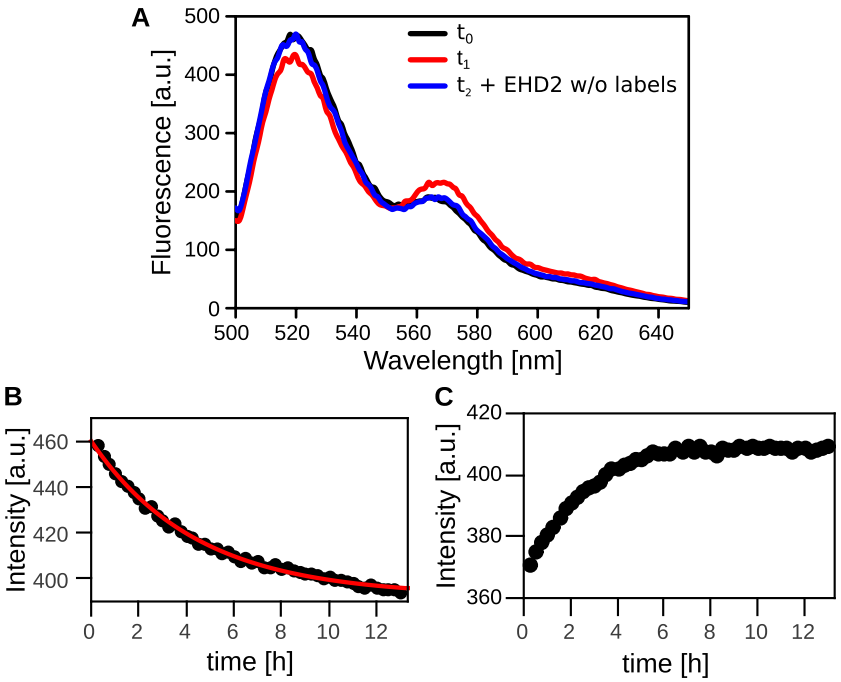

Figure 25: Exchange of monomers in dimeric EHD2 observed with FRET. **A** Fluorescence emission scans ranging from 500 nm to 650 nm upon excitation at 494 nm. Donor (A488) labeled single-cysteine EHD2 C138 and acceptor (A555) labeled single-cysteine EHD2 L303C were mixed at t_0 and incubated for 20 h (t_1). After addition of a 5-fold molar excess of cysteine-less EHD2 and further incubation for 20 h a third spectrum was recorded (t_2). Note, that the spectra were normalized to the same area under the curve. **B** The rate of EHD2 monomer exchange was determined by following the fluorescence emission at 519 nm upon excitation at 494 nm over 13 h. FRET causes an intensity loss after mixing donor-labeled single-cysteine EHD2 C138 and acceptor labeled single-cysteine EHD2 L303C. **C** The addition of 5-fold molar excess of a cysteine-less EHD2 mutant extinguished FRET, and thus disrupted the donor-acceptor-labeled dimers. A first-order exponential decay function was fitted to the experimental data (red line, see Section 2.4.9).

3.3.2.3 *Determining the accurate position of the amino-terminus*

To accurately determine the position of Leu5, X-ray crystallography was employed. Previously, the N-terminus was not modeled in the ADP- or AMP-PNP-bound crystal structures, due to missing density or connectivity. The introduction of an anomalous scatterer at position 5 might produce an anomalous signal, sufficient to verify the EPR derived location of Leu5. To this end, Leu5 was mutated to methionine and a selenomethionine (SeMet)-substituted variant of this mutant in the ADP- and AMP-PNP-bound form was crystallized as described in Section 2.3.5 and 2.6.1 - 2.6.5. The EHD2 L5M crystals diffracted to slightly higher resolution, compared to the previously obtained data for EHD2 Q410A. Data collection and refinement statistics are summarized in Table 7 and 8. In total, 15 out of 16 Se were identified. With either nucleotide bound an additional anomalous signal was identified. This signal was the only signal, which did

not superpose with anomalous signals from the previously determined anomalous substructure of SeMet EHD2 Q410A. Thus, the additional anomalous signal corresponds to SeMet5 (Figure 26 A). The electron density was improved by providing experimentally derived phases from EHD2 L5M Q410A•AMP-PNP to Refmac. However, only in the case of EHD2 L5M•AMP-PNP electron density for the N-terminal 7 residues showed up (Figure 26 B). The orientation of the amino-terminus was defined by side-chain density for Phe2, Trp4 and the anomalous signal. It is unlikely that the anomalous signal belongs to SeMet1, because the Trp4 side-chain density is spaced by one residue from the anomalous signal. Furthermore, the SeMet1 signal was not observable in EHD2 Q410A, indicating that the new signal arises from L5M. The N-terminal stretch was located in a hydrophobic groove at the distal side of the G domain (Figure 26 C). The position is in agreement with the EPR derived location of Leu5. These data, together with the immobile components observed in the CW spectra, indicate that the amino-terminal stretch of the helical domain including residues 1-7 packs in a hydrophobic pocket of the G domain in solution.

Table 7: Data collection statistics for crystals of nucleotide-bound EHD2 L5M.

DATA COLLECTION	EHD2•ADP L5M Q410A SEMET	EHD2•AMP-PNP SEMET
Date	24.11.2010	
Beamline	BESSY II 14.1	
Wavelength [Å]	0.9797	
Temperature [K]	100	
Space group	C2	
Cell dimensions		
a [Å]	99.91	98.77
b [Å]	134.77	133.59
c [Å]	56.15	55.88
α [°]	90.0	90.0
β [°]	106.34	106.10
γ [°]	90.0	90.0
V_M [Å^3/Da] †	2.96	2.89
Resolution [Å] ‡	42 (3.18) - 3.0	41 (3.1) - 3.0
No. of observed reflections	52615 (6745)	42946 (4095)
No. of unique reflections	26444 (3509)	26426 (2552)
R_{obs} [%]	4.1 (38.9)	4.7 (33.9)
R_{meas} [%] §	5.7 (54.2)	6.7 (47.8)
I/σ(I)	14.66 (2.19)	10.5 (1.8)
Completeness [%]	93.5 (77.5)	95.9 (98.0)
Redundancy	2.0	1.6
Overall B-factor (Wilson) [Å^2]	76.2	79.6

† According to [212].
‡ Numbers in parentheses apply for the highest resolution shell.
§ According to [213].

Table 8: Refinement statistics for nucleotide-bound EHD2 L5M.

REFINEMENT	EHD2•ADP L5M Q410A SEMET	EHD2•AMP-PNP L5M Q410A SEMET
Resolution [Å]	42 - 3.0	41 - 3.0
No. of reflections used	13157	13423
R_{work}† / R_{free}‡ [%]	26.6 / 30.8	24.5 / 28.4
No. of atoms	3769	3984
Protein	3736	3947
Nucleotide	27	31
Mg^{2+}	1	1
Ca^{2+}	1	1
Water	4	4
Averaged B-factor protein [Å²]	83.2	82.1
RMSD		
Bond length [Å]	0.007	0.005
Bond angles [°]	1.105	0.830
Ramachandran Statistics		
Favored [%]	96.1	95.3
Outliers [%]	0.4	0.2

† $R_{work} = \frac{\sum |F_{obs} - F_{calc}|}{\sum F_{obs}}$

‡ R_{free} was calculated with the same set of test reflections as in 2QPT [164].

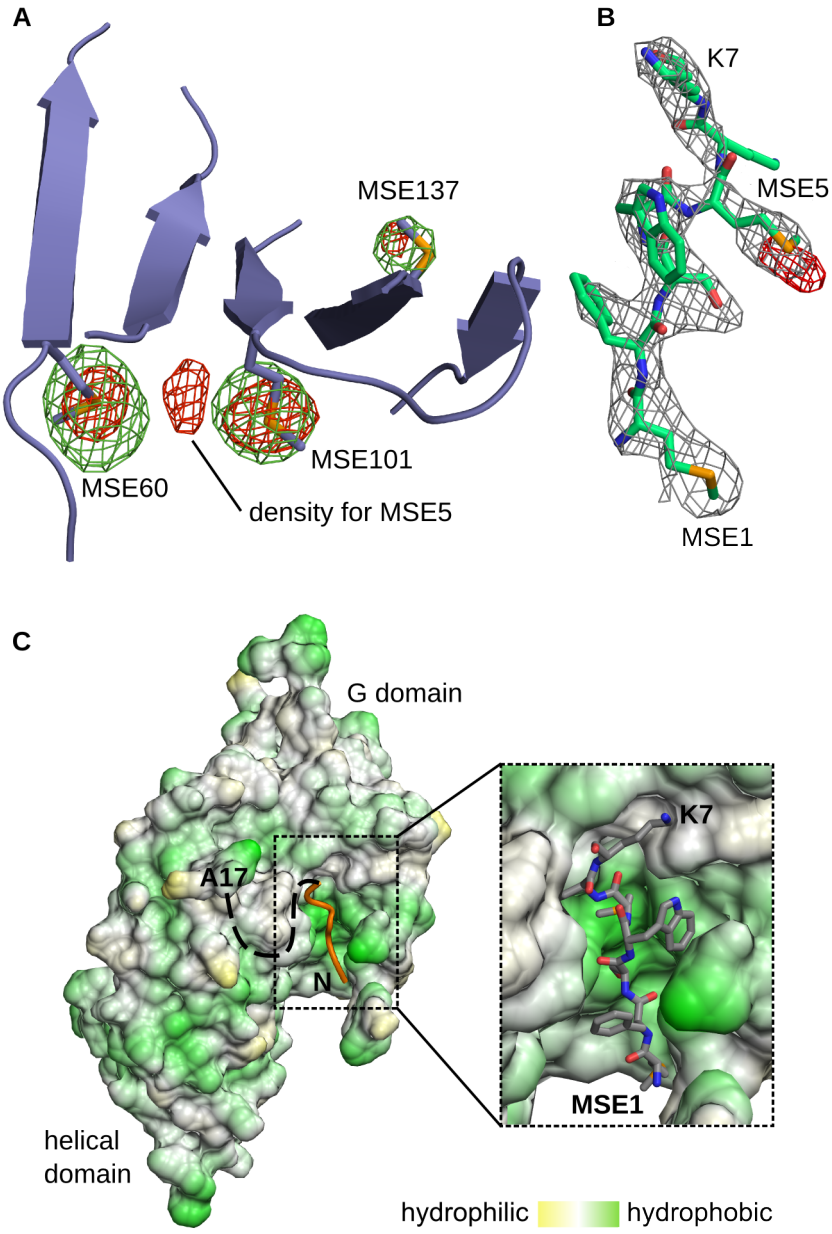

Figure 26: The N-terminus is located in a hydrophobic pocket of the G domain. **A** Anomalous density (contoured at 4 σ) from AMP-PNP-bound mmEHD2 Q410A (green, PDB Code: 2QPT) and AMP-PNP-bound mmEHD2 L5M Q410A (red). Additional anomalous density for SeMet5 (MSE5) is visible. **B** Modeled N-terminal stretch (residue 1-7) in the $2F_O$-F_C density, contoured at 1 σ. The anomalous signal for SeMet5 (contoured at 4 σ) is indicated. **C** Hydrophobic surface representation of the G and helical domain of EHD2, where green represents hydrophobic and yellow polar surface residues. The amino-terminal stretch is shown in orange and locates into a hydrophobic pocket.

3.3.3 *The amino-terminus gets immobilized upon membrane binding*

In small G proteins of the Arf family, an N-terminal helix is inserted into the membrane inducing membrane remodeling [92]. To elucidate whether the N-terminus of the large, dynamin-like EHD2 has a similar function, CW spectra of EHD2 variants singly spin labeled at the N-terminal residues were recorded in the presence of small uni-lamellar vesicles derived from bovine brain lipids (Folch-SUV) as described in Section 2.5.2. Surprisingly, the spectra of all N-terminal residues showed immobilization upon membrane binding (Figure 27). The immobilization could be caused by direct or indirect membrane binding. As a control, residue 277 in the G domain and residue 328 from the previously described lipid binding site were labeled. In the presence of liposomes, residue 277 did not show immobilization, whereas residue 328 showed strong immobilization.

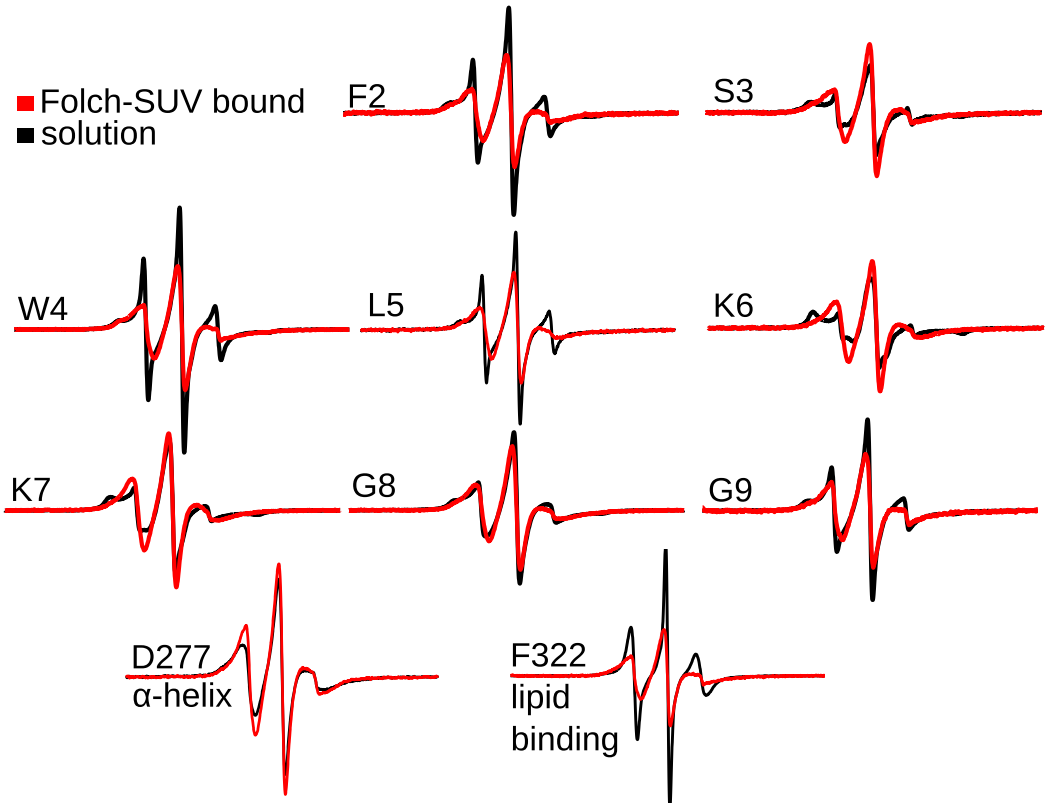

Figure 27: Continuous Wave (CW) spectra in the absence (black) and presence (red) of Folch-SUV. All spectra showed an immobilization upon membrane binding.

3.3.4 *The amino-terminus switches into the lipid bilayer*

To determine whether immobilization of the N-terminal residues was caused by direct membrane interaction, accessibility of the spin labels to paramagnetic colliders O_2 (partitions in the membrane phase) and NiEDDA (partitions in the soluble phase) was measured by EPR (Section 2.5.3). Φ is defined as the natural logarithm of the ratio between the accessibility to oxygen Π_{O_2} and the accessibility to NiEDDA Π_{NiEDDA}, i.e. $\Phi = \ln \frac{\Pi_{O_2}}{\Pi_{NiEDDA}}$. Negative Φ values are typical for spin-labeled residues in aqueous environments, whereas positive Φ values indicate membrane interaction of the spin-labeled residue [196, 217].

In the absence of membranes, Φ values of residues 2-9 were negative, as expected for surface exposed residues. In the presence of liposomes Φ values of residues 2 and 5-9 became positive (Figure 28 A). This clearly demonstrates that these residues interact directly with the membrane.

Residues of the previously described membrane interaction site were also tested for direct membrane interaction. In the absence of liposomes, residues 277, 320-323 and 328 showed negative Φ values, as expected for surface exposed residues. In the presence of liposomes, residues 320, 321, 322 and 328 showed positive Φ values, indicating direct membrane interaction. In contrast, residue 323 in the membrane interaction site and residue 277 in the G domain displayed negative Φ values in the presence of liposomes (Figure 28 A).

So far the insertion depth of the tested residues was unknown. Residues inserting into the membrane between 3 and 10 Å interact with the phosphate moiety, whereas residues inserting deeper into the membrane interact with the acyl chains [80, 107]. The previously obtained positive Φ values can be converted into an insertion depth. To this end, liposomes were generated, which contain spin labeled lipids. The spin label is linked to the lipid at positions between 3 and 16 Å from the lipid head group. The accessibility of the spin labeled lipids in the presence of unlabeled, cysteine-free EHD2 was measured. These data were fitted with a polynomial regression (Figure 28 B). Using this fitting function, an insertion depth of 3 to 16 Å was assigned to the tested residues (Figure 28 A). Taken together, the accessibility measurements confirmed a direct membrane interaction of the previously described lipid binding site [164] and newly assigned an interaction with the phosphate headgroups to residues 2 and 5-9.

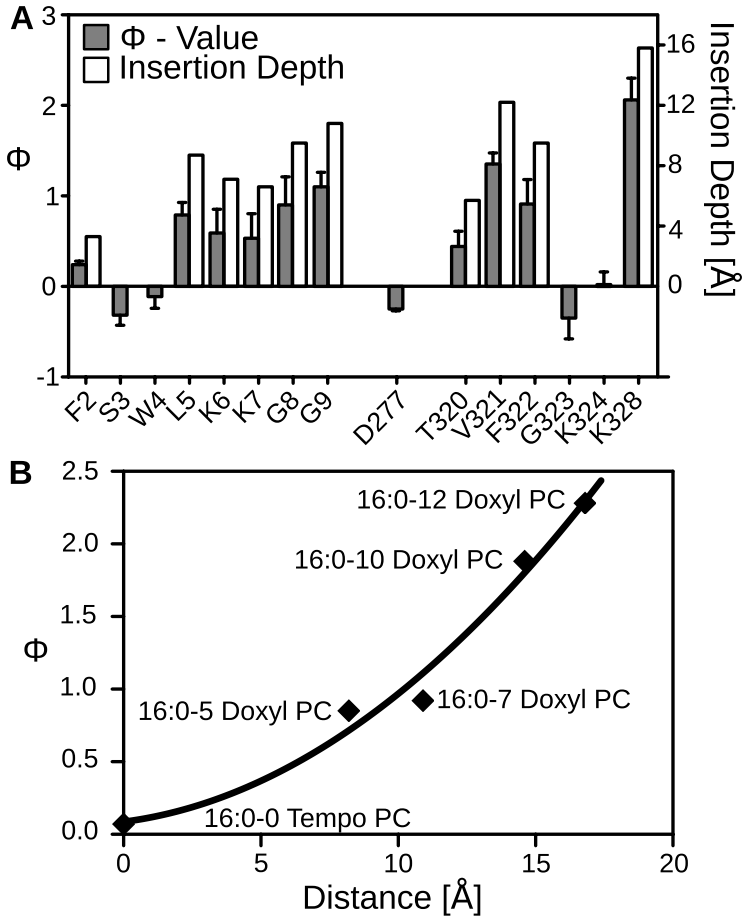

Figure 28: Residues 2-9, 320-323 and 328 were tested for direct membrane interaction via accessibility measurements. **A** Positive Φ indicates direct membrane interaction. Residue 277 served as a control. Residue 277 is located in the G domain and should not interact with the membrane. Residues 320-328 are located in the previously described membrane binding site [164]. **B** Calibration of insertion depths with spin-labeled lipids with known insertion depths. The Φ values from A were converted into insertion depths (see A, right scale).

3.3.5 *The amino-terminus is not required for binding of EHD2 to liposomes*

How important is the N-terminus for liposome binding of EHD2? Binding of wild-type EHD2 and amino-terminal variants of EHD2 to Folch large uni-lamellar vesicles (Folch-LUV) was compared by co-sedimentation assays as described in Section 2.4.7. The amino-terminal variants comprise a variant lacking amino acids 1-18 (EHD2$^{19\text{-}543}$) and a double point mutant, where two lysines that interact with the phosphate headgroups (Figure 28) were replaced by aspartates (EHD2 KK6,7DD). All three EHD2 variants bound Folch-LUV with similar efficacy (Figure 29), indicating that the N-terminal stretch is not essential for membrane binding.

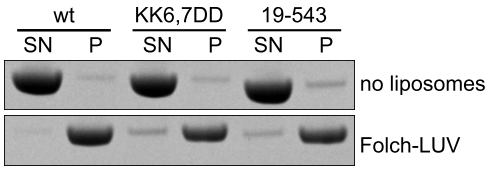

Figure 29: Co-sedimentation assay with EHD2 and Folch-LUV. EHD2 wild-type bound with same efficacy to Folch-LUV as EHD2 KK6,7DD and EHD2$^{19\text{-}543}$. SN - supernatant, P - pellet.

3.3.6 *The integrity of the oligomeric EHD2 coat depends on the amino-terminus*

Previously, liposome binding for all three tested EHD2 variants was observed (Section 3.3.5). However, the amino-terminal mutants might affect the integrity of the tubular protein coat observed in negative-stain EM. Tubulation assays with wild-type EHD2 and the amino-terminal mutants EHD2$^{19\text{-}543}$ and EHD2 KK6,7DD were performed as described in Section 2.4.10.

Wild-type EHD2 tubulated Folch-MLVs and oligomerized in ring-like structures with clearly visible striations around the liposomes. EHD2$^{19\text{-}543}$ also tubulated liposomes but did not show characteristic striations pointing to an alternative assembly at the membrane surface. The N-terminal double point mutant EHD2 KK6,7DD showed an intermediate morphology: Liposomes were tubulated with only a few characteristic striations visible. A gallery of four micrographs for each mutant is shown in Figure 30. The electron microscopic data suggest that the N-terminus contributes to a proper organization of the EHD2 oligomer with its characteristic striations.

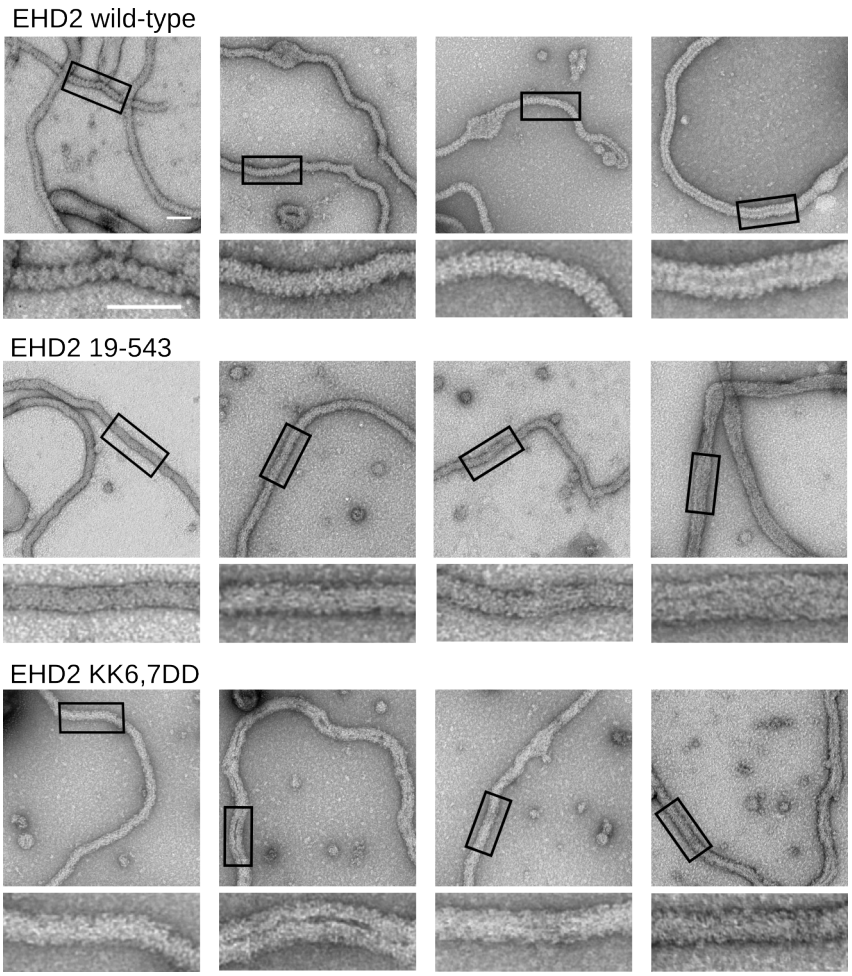

Figure 30: Negative stain electron microscopy of three EHD2 variants in the presence of Folch-MLVs. Wild-type EHD2 tubulated liposomes with characteristic striations. EHD2$^{19\text{-}543}$ generated tubules without striation and EHD2 KK6,7DD showed an intermediate tube morphology with a few striated tubes. All images 12,500 x magnification, lower panels show enlargements of the boxed areas, scale bar represents 100 µm.

3.3.7 *The amino-terminus is required for liposome-stimulated ATPase reaction*

The N-terminal EHD2 mutants EHD2$^{19\text{-}543}$ and EHD2 KK6,7DD bound liposomes with similar efficacy as the wild-type, but showed a different tube morphology. How do the N-terminal mutants affect the intrinsic ATPase rate? How does the different oligomerization pattern caused by the N-terminal mutants affect the stimulated ATPase rate? Previous experiments showed that the intrinsic ATPase rate of EHD2 wild-type of 0.66 ± 0.02 h^{-1} can be stimulated 8-fold to 5.4 ± 0.2 h^{-1} by the addition of Folch-SUV [164].

Here, the ATPase rate was determined by incubating EHD2 wild-type, EHD2 KK6,7DD and EHD2$^{19\text{-}543}$ with 100 µM ATP in the absence or presence of Folch-LUVs. Remaining ATP after 0, 15, 30, 45 and 60 min was measured as described in Section 2.4.4. The plotted data (Figure 31) was fitted with a linear regression

and the ATPase rates could be derived (Table 9). The ATPase rate for EHD2 wild-type was very similar to the previously reported value. Strikingly EHD2$^{19\text{-}543}$ showed no stimulated ATPase rate, pointing to a function of the amino-terminus in ATPase regulation. The double point mutant KK6,7DD showed efficiently stimulated ATPase rate, similar to wild-type.

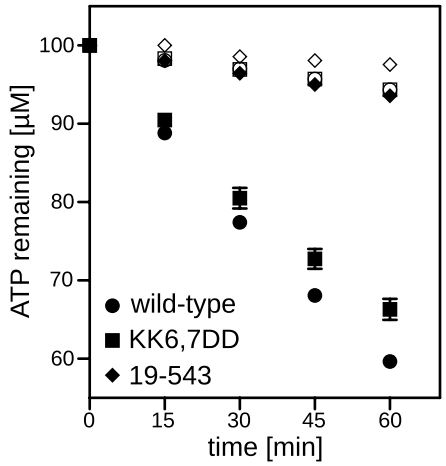

Figure 31: Remaining ATP after 0, 15, 30, 45 and 60 min was measured by HPLC in three independent experiments. Open (closed) symbols represent data points in the absence (presence) of liposomes. The ATPase rate of EHD2$^{19\text{-}543}$ was not stimulated by the addition of liposomes. Error bars represent standard deviation of the three experiments. Where no error bar is shown, the error bar was smaller than the data symbol.

Table 9: ATPase rates of EHD2 wild-type, EHD2 KK6,7DD and EHD2$^{19\text{-}543}$ in the absence (intrinsic rate) or presence (stimulated rate) of Folch-LUVs.

EHD2	INTRINSIC RATE [h^{-1}]	STIMULATED RATE [h^{-1}]
wild-type	0.55 ± 0.01	4.06 ± 0.09
KK6,7DD	0.56 ± 0.01	3.41 ± 0.13
19-543	0.27 ± 0.00	0.64 ± 0.13

3.3.8 *Amino-terminal residues contribute to ATP-dependent membrane remodeling*

Quantification of membrane remodeling by electron microscopy is often misleading, because the quality of the sample on each grid and within different grids varies dramatically. Therefore, a time-resolved batch assay was employed, in which membrane remodeling is averaged over multiple EHD2 decorated liposomes. A fluorescent dye and a contact quencher were incorporated into Folch-LUVs and leakage of the dye into the solution was followed over time by measuring the fluorescence increase induced by fluorescence de-quenching (Sec-

tion 2.4.8). Membrane remodeling caused by EHD2 wild-type, EHD2$^{19\text{-}543}$ and EHD2 KK6,7DD in the presence or absence of ATP was followed.

In the absence of nucleotides, EHD2 wild-type induced slow leakage, which could be efficiently (12-fold) stimulated by addition of ATP. Addition of the non-hydrolyzable ATP analogue ATPγS also stimulated membrane remodeling, but not to such an extent as ATP (only 6-fold). These data indicate that the ATPase reaction of EHD2 is closely linked to membrane remodeling events. Interestingly, membrane remodeling of EHD2$^{19\text{-}543}$ was not significantly stimulated by addition of ATP, consistent with a function of the N-terminus in the regulation of ATPase activity. Membrane remodeling of EHD2 KK6,7DD was 5-fold slower compared to wild-type EHD2 in the presence of ATP pointing again to the importance of the two positively charged N-terminal residues for ATPase regulation and membrane remodeling. The fluorescence traces are depicted in Figure 32.

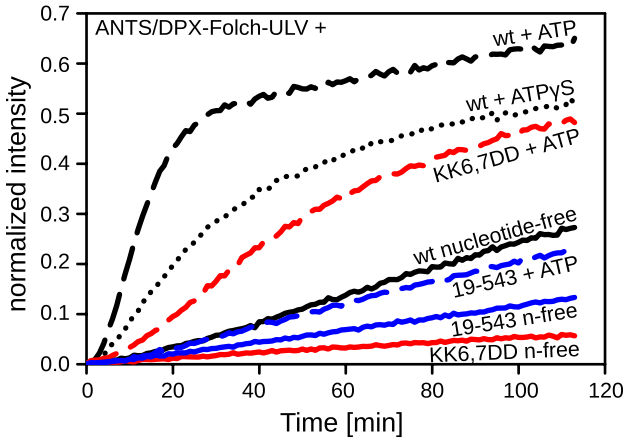

Figure 32: Folch-LUVs filled with a dye/quencher mixture were incubated with the indicated EHD2 variants in the presence or absence of nucleotide. Fluorescence dequenching induced by membrane leakage was followed over time. Traces were normalized to maximum leakage induced by the addition of 1 % Triton X-100. Folch-LUVs without the addition of EHD2 did not show leakage.

3.3.9 *EHD2$^{19\text{-}543}$ recovers as fast as the wild-type after photobleaching*

In the previous experiment the membrane deformation potential of the N-terminal variants was compared to EHD2 wild-type. The *in vitro* findings were complemented with Fluorescence Recovery After Photobleaching (FRAP) data from 3T3-L1 cells. Changes in the recovery rate reflect defects in membrane binding or targeting of EHD2. N-terminally GFP-tagged EHD2$^{19\text{-}543}$ showed a recovery rate similar to the wild-type, whereas EHD2 KK6,7DD recovered faster from photobleaching (Figure 33). This indicates that the N-terminus is not required for binding of EHD2 to caveolae.

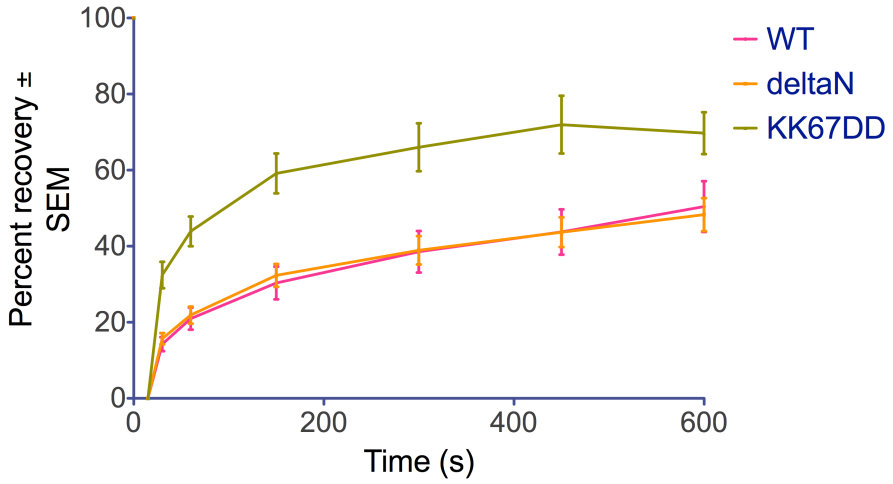

Figure 33: FRAP data from 3T3-L1 cells overexpressing N-terminally GFP-tagged EHD2 wt, EHD2$^{19\text{-}543}$ or EHD2 KK6,7DD. EHD2$^{19\text{-}543}$ recovered as fast as the wild-type, whereas EHD2 KK6,7DD recovered faster than the wild-type after photo bleaching. Figure kindly provided by Björn Morén.

3.4 TARGETING OF EHD2 TO THE MEMBRANE

In cell biological experiments, EHD2 co-localized with caveolin1 (Cav1) [52, 218, 150, 219]. Together with the cavin family of proteins [52–57], PACSIN2 was also identified as a caveolar component [218, 111, 150]. GST-pulldown experiments showed that EHDs and PACSINs may interact [177]. Most likely the proteins caveolin, cavin, EHD2 and PACSIN are functionally related.

To date it was unclear, how EHD2 is targeted to caveolae. PACSIN2 might recruit EHD2 via an interaction of the NPF motifs of PACSIN2 with the EH domain of EHD2. This interaction was analyzed in detail and other targeting mechanisms were elucidated. Possibly, a predicted movement of the EH domain from the top position to the side position is implicated in oligomer formation and targeting.

3.4.1 *EHD2 binds the F-BAR protein PACSIN2*

PACSIN2 carries three NPF motifs located in the linker between the F-BAR domain and the SH3 domain. The EH domain of EHD2 binds NPF motifs. The interaction between PACSIN2 and EHD2 was characterized by isothermal titration calorimetry (ITC) as described in Section 2.4.5. Preparations of PACSIN2 yielded active protein, because PACSIN2 tubulated liposomes in EM studies.

An interaction between EHD2 and PACSIN2 could be confirmed (Figure 34 A). The dissociation constant K_D was 37 ± 9 µM. The stoichiometry n was 0.5 ± 0.1, suggesting that one PACSIN2 dimer binds two EHD2 dimers (Table 10). Note that both proteins form stable dimers in solution [164, 109].

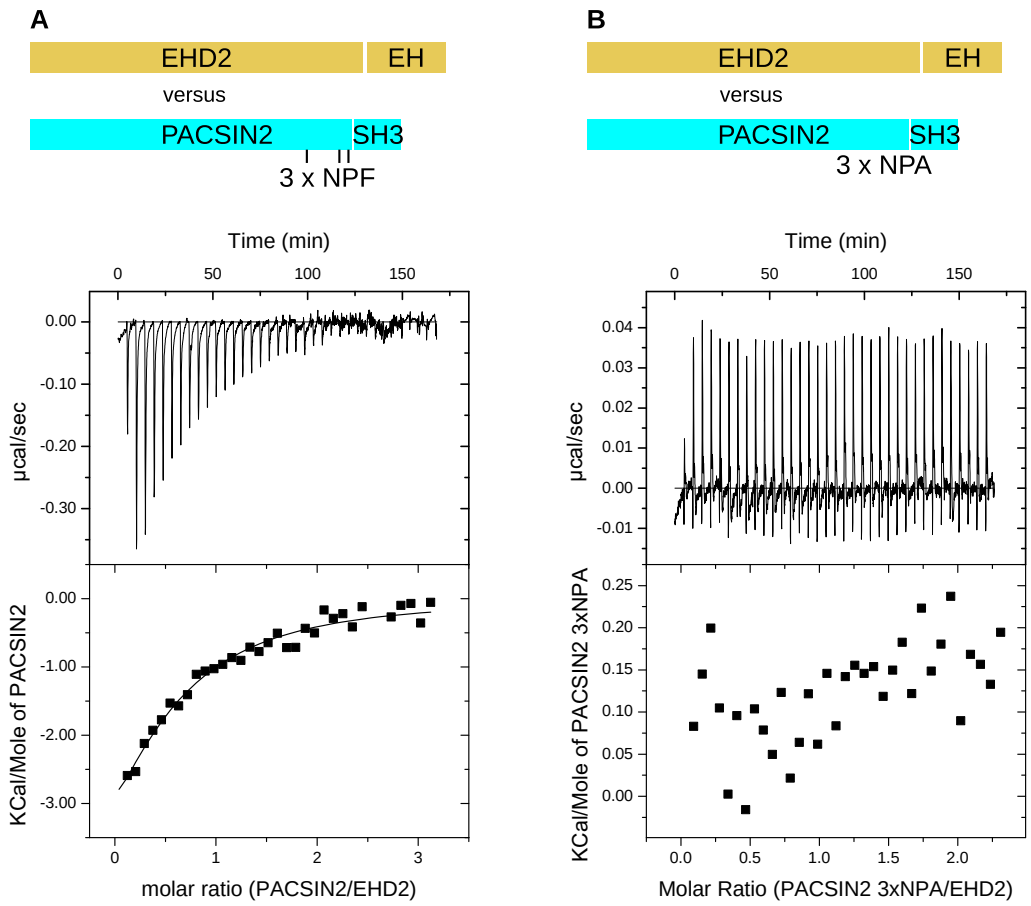

Figure 34: EHD2 bound directly to NPF motifs from PACSIN2. Solutions containing 750 µM PACSIN2 (**A**) or 600 µM PACSIN2 F364A, F407A, F419A (PACSIN2 3xNPA) (**B**) were injected stepwise into the reaction cell containing 50 µM EHD2 and the resulting heat changes were monitored. The lower panel shows the integrated heating power normalized to the concentration of injected PACSIN2. The fit of the data is indicated, fitted values are shown in Table 10. No binding was detected for EHD2 vs. PACSIN2 3xNPA.

Next, I wanted to verify that the interaction between EHD2 and PACSIN2 is indeed mediated by the NPF motifs. Therefore, I measured the affinity between EHD2 and a PACSIN2 variant with all three NPF motifs mutated to NPA (F364A, F407A, F419A: PACSIN2 3xNPA). No interaction was observed between EHD2 and PACSIN2 3xNPA (Figure 34 B), strongly suggesting that the NPF motifs are crucial for EHD2-PACSIN2 binding.

To exclude that the SH3 domain of PACSIN2 interacts with EHD2, binding of a truncated PACSIN2 variant ($PACSIN2^{1\text{-}425}$, PACSIN2 ΔSH3) to EHD2 was measured (Figure 35 A). PACSIN2 ΔSH3 bound EHD2 with comparable affinity as the wild-type (Table 10), indicating that the SH3 domain is dispensable for the interaction between EHD2 and PACSIN2.

To proof that the EH domain binds to the NPF motifs, an ITC experiment with the isolated EH domain and PACSIN2 was performed. Four EH domains

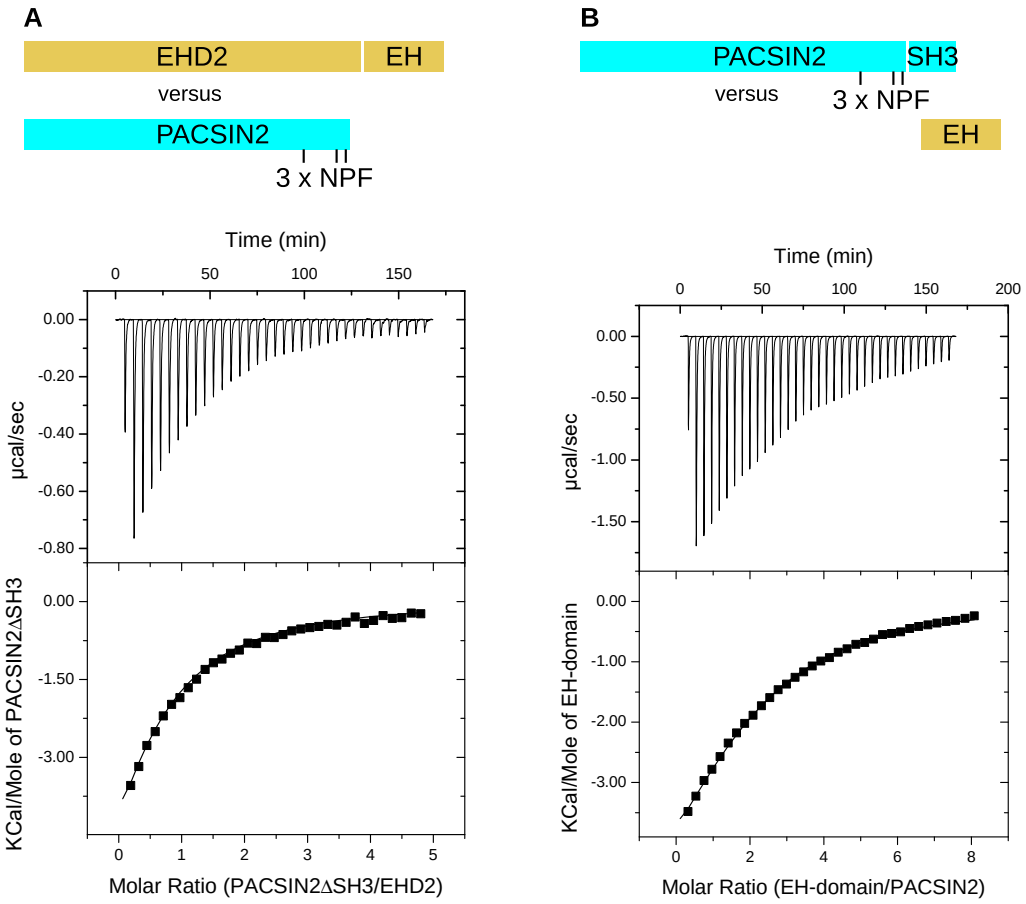

Figure 35: EHD2 bound PACSIN2 lacking its SH3 domain and the EH domain alone was sufficient to bind PACSIN2. **A** EHD2 vs. PACSIN2$^{1\text{-}425}$ (PACSIN2 ΔSH3, 1.1 mM) was measured as described in Figure 34. The affinity was comparable to the wild-type, indicating that the SH3 domain is not involved in the EHD2-PACSIN2 interaction. **B** Aliquots of 2.1 mM of the isolated EH domain of EHD2 were injected stepwise into the reaction cell containing 50 µM PACSIN2. The EH domain alone interacted with PACSIN2.

bound one PACSIN2 dimer (Figure 35 B, Table 10). The stoichiometry is consistent with the data on full-length EHD2. However, the affinity is reduced two-fold compared to the interaction of the full-length proteins. The lower affinity of the isolated EH domain towards its substrate can be explained by the reduced avidity of monomeric EH domains compared to dimeric EHD2.

Furthermore, it was hypothesized that the affinity of the EH domain towards PACSIN2 changes, if internal (G/N/K)PF motifs were mutated. The mutations might lead to tighter or weaker fixation of the EH domain in *cis*. Surprisingly, neither mutations in the GPF motif present in the linker on the top-site, nor mutations in the KPFxxxNPF loop in the interswitch region changed the affinity to PACSIN2. For EHD2 G420N, EHD2 F422A, EHD2 K120N and EHD2 F128A the dissociation constant K_D and the stoichiometry n was around 20 µM and 0.5 (Table 10).

Table 10: Dissociation constants and stiochiometry obtained by isothermal titration calorimetry for the interaction of EHD2 with PACSIN2

CELL	SYRINGE	K_D [µM]	STOICHIOMETRY
EHD2	PACSIN2	37 ± 9	0.50 ± 0.1
EHD2	PACSIN2 3xNPA	no binding	no binding
EHD2	$PACSIN2^{1\text{-}425}$ (ΔSH3)	53 ± 3	0.52 ± 0.1
PACSIN2	$EHD2^{440\text{-}543}$ (EH domain)	94 ± 4	1.95 ± 0.1
EHD2 K120N	PACSIN2	22 ± 1	0.49 ± 0.02
EHD2 F128A	PACSIN2	25 ± 1	0.47 ± 0.02
EHD2 G420N	PACSIN2	17 ± 3	0.55 ± 0.06
EHD2 F422A	PACSIN2	26 ± 2	0.55 ± 0.04

Cell biological experiments with N-terminally GFP-tagged EHD2 mutants carrying the single point mutations G420N and F422A were performed. In Fluorescence Recovery After Photobleaching (FRAP) no rate change compared to EHD2 wild-type was observed (Figure 36). This indicates that top-site binding of the EH domain to the GPF motif in the linker neither influences membrane binding nor a possible recruitment of EHD2 to the membrane by PACSIN2. These observations corroborate the ITC data.

EHD2•AMP-PNP and PACSIN2 crystallized in very similar conditions [164, 109]. Therefore I tried to co-crystallize both proteins. The proteins alone crystallized in control drops, but neither PACSIN2 nor $PACSIN2^{1\text{-}425}$ (PACSIN2 ΔSH3) formed crystals together with EHD2 in the different nucleotide-loading states.

In summary, the data shows that two EHD2 dimers bind one PACSIN2 dimer by the interaction of the NPF motifs with the EH domain. The affinity is in the low micromolar range and binding is independent from the SH3 domain.

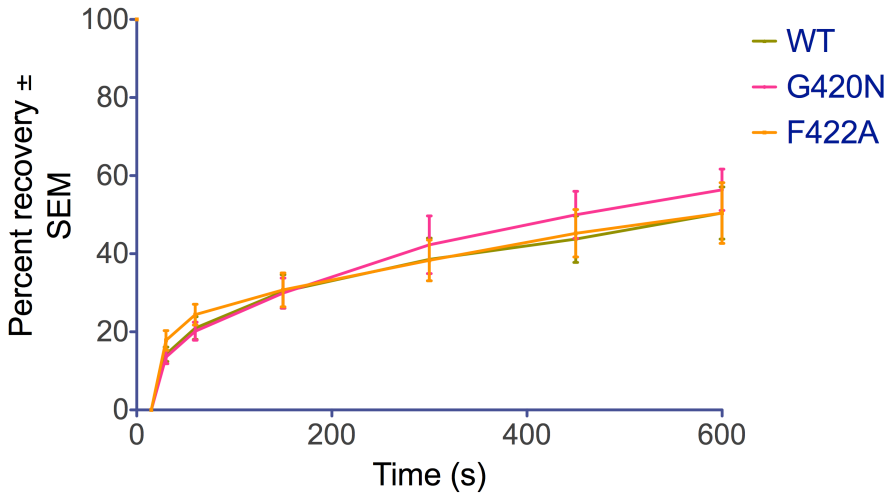

Figure 36: Mutations of the GPF motif in the linker between the helical domain and the EH domain did not affect FRAP. 3T3-L1 cells overexpressing N-terminally GFP-tagged EHD2 G420N and EHD2 F422A were bleached for 10 s. Both mutants recovered as fast as the wild-type. Error bars are ± SEM. Figure kindly provided by Björn Morén.

3.4.2 *The EH domain might switch to the membrane*

EH domains contain two helix-loop-helix motifs forming two NPF-binding pockets: a classical NPF-binding pocket termed NPF-binding pocket 1 [170] and a NPF-binding pocket 2 as seen in the Eps15-stonin2 complex [176]. In dimeric EHD2, the EH domain sits on top of the G domain from the neighboring monomer, bound to a GPF motif via its NPF binding pocket 1 (top-site). This GPF motif is part of a flexible linker between the helical domain and the EH domain. It was already speculated previously that the loose attachment of the EH domain allows a movement of the EH domain to the side of the G domain, thereby regulating oligomerization (Figure 37 B) [164]. However, the exact location of the EH domain at the side-site was not known.

The SeMet dataset of EHD2 L5M Q410A in the AMP-PNP-bound form resulted in an improved electron density map of EHD2 (Section 3.3.2.3). An additional feature of this map was an extension of a loop region at the side of the G domain. The atomic model was extended, and now included parts of the interswitch region containing the KPFxxxNPF motif (Figure 37 A). In the crystal, the newly build loop bound into the NPF binding pocket 2 of a symmetry related EH domain. This implied that the EH domain might bind via binding pocket 2 to the side of the G domain (Figure 37 C, D).

Furthermore, the C-terminal EH domains of EHD1 and EHD4 and the second EH domain (EH2) of Eps15 have been shown to bind phosphatidylinositols via conserved amino acids [220]. Homologous residues in EHD2 are Arg488, Lys491 and Arg497. Interestingly, the EH domain of EHD2, when located at the side-site,

is ideally positioned to interact with the membrane bilayer through the conserved residues (Figure 37 D).

Accessibility measurements were carried out for residues Arg488, Lys491 and Arg497 as described in Section 2.5.3. Arg488 ($\Phi = 0.14$) bound to the membrane, but Lys491 ($\Phi = -0.42$) and Arg497 ($\Phi = -1.15$) did not interact with the membrane.

Taken together, it is most likely that the EH domain adopts a second conformation. In solution, it localizes to the top of the G domain, with its primary NPF binding pocket bound to the GPF motif present in the linker between the helical domain and the EH domain. In the presence of liposomes, the EH domain might switch to the side position, binding to the NPF motif in the KPFxxxNPF loop via its secondary NPF binding pocket. Specific residues mediate membrane binding. The possible implication of this finding on the regulation of nucleotide hydrolysis, oligomerization and its relation to the N-terminus will be discussed in Chapter 4.

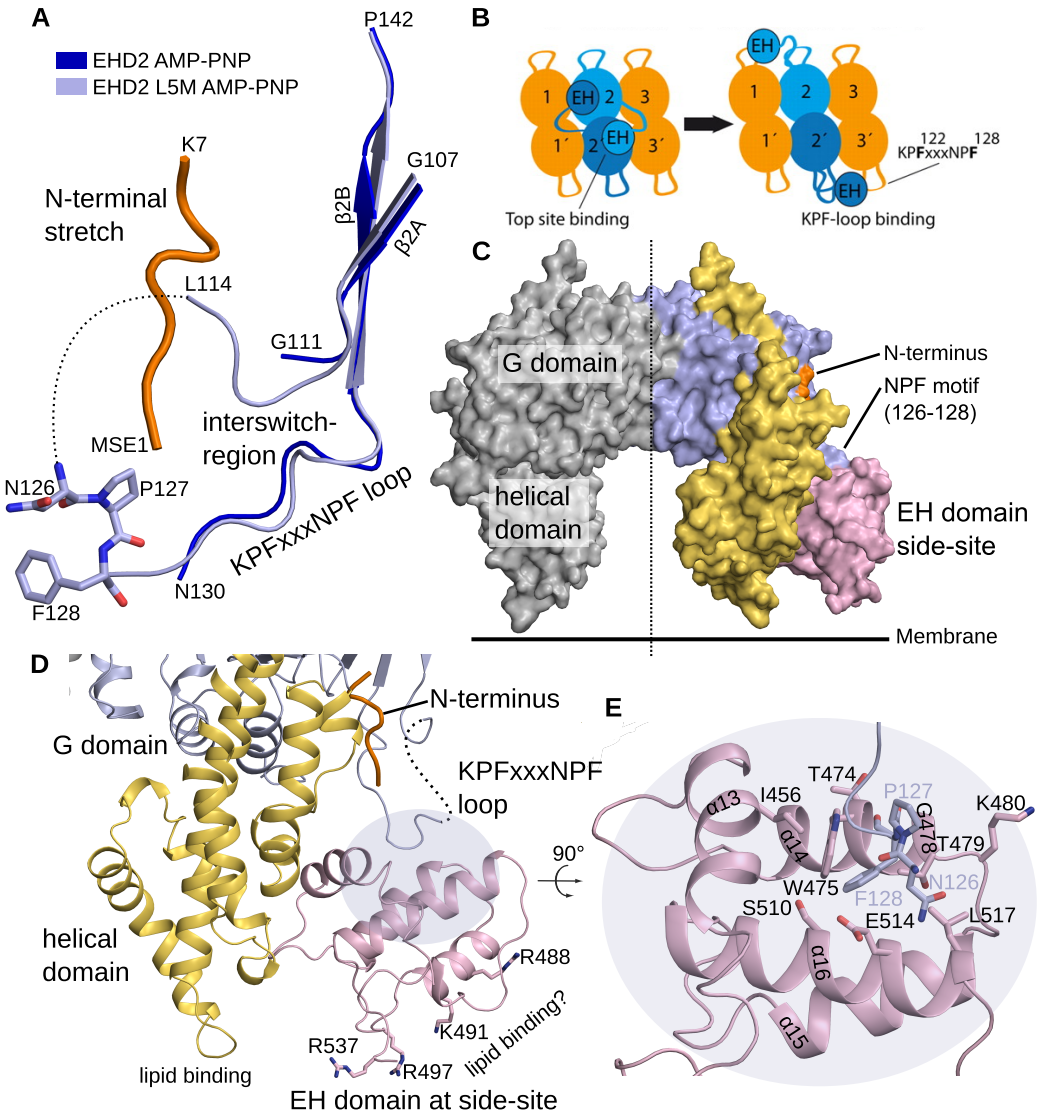

Figure 37: The EH domain at the side-site. **A** Superposition of the interswitch regions of AMP-PNP-bound EHD2 Q410A (blue, PDB Code: 2QPT) and AMP-PNP-bound EHD2 L5M Q410A (lightblue) in cartoon representation. The amino-terminus is shown in orange. Extra density, compared to the previously obtained data, allowed modeling of the NPF motif (amino acids 126-128, shown in stick representation). **B** Schematic illustration shows three EHD2 dimers in top view and the proposed transition of the EH domains to the side-site. Monomers comprising one dimer are labeled 1 and 1′ etc. **C** Surface representation of the EHD2 dimer with the EH domain at the side-site. One monomer is colored in grey, the other according to the domains (helical domain: yellow, G domain: blue, EH domain at the side-site: pink). The amino terminus (orange) and the NPF motif (126-128) binding to the second NPF binding site are indicated. **D** The EH domain located at the side-site interacts with the NPF motif (126-128) present in the G domain and possibly with the lipid bilayer. The cartoon representation is colored as in A. Residues Arg488, Lys491, Arg497 and Arg537 are at similar positions to residues known to interact with PIP2 in EH2 from Eps15. They are oriented towards the lipid bilayer, similar to the residues of the lipid binding site of the helical domain. Binding of NPF (126-128) to the second NPF binding pocket is highlighted (blue circle). **E** Magnification of the blue area from D. Conserved side chains interacting with NPF (126-128) are shown as sticks.

3.4.3 *Mutations in the EH domain affect recovery after photobleaching*

To investigate the function of the conserved residues Arg488, Lys491 and Arg497 in 3T3-L1 cells, the amino acids were replaced by negatively charged Asp. Inverting the charge of the side chains makes binding to the negatively charged lipid headgroups unlikely. The mutation Gly487Leu was predicted to sterically close the primary NPF binding pocket. FRAP experiments were performed with these single point mutants as described in Section 2.7.1.

Arg488Asp showed faster recovery, whereas Lys491Asp and Arg497Asp showed only slightly elevated recovery rates compared to wild-type EHD2. Note that the point mutant Gly487Leu, predicted to close the primary NPF binding pocket, showed a similar phenotype as the neighboring Arg488Asp (Figure 38). Possibly, Arg488Asp also closed the primary NPF binding pocket and thereby accelerated the recovery rates.

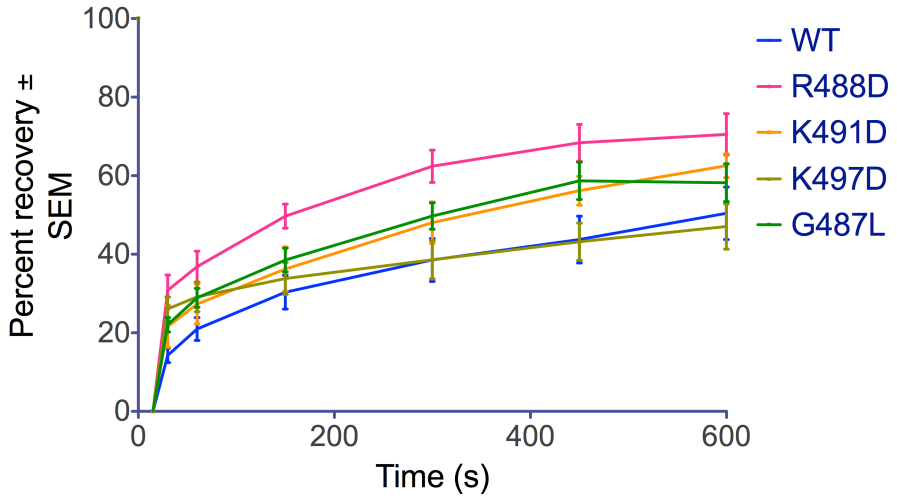

Figure 38: Mutations of the conserved residues R488D, K491D, R497D in the EH domain showed faster FRAP. 3T3-L1 cells overexpressing N-terminally GFP-tagged EHD2 R488D, EHD2 K491D, EHD2 R497D and EHD2 G487L were bleached for 10 s. R488D recovered faster, K491D and R497D only slightly faster than wild-type EHD2. G487L, which is predicted to close the primary NPF binding pocket, recovered as fast as the neighboring R488D. Error bars are ± SEM. Figure kindly provided by Björn Morén.

3.4.4 *The KPFxxxNPF loop and not the EH domain targets EHD2 to caveolae*

In order to find out, if the EH domain is required for targeting of EHD2 to caveolae, co-localization of Cav1 with a construct lacking the EH domain ($EHD2^{1\text{-}416}$, EHD2 ΔEH) was analyzed. Surprisingly, this construct localized to caveolae similar to the wild-type (Figure 39). Thus, the EH domain is dispensable for the recruitment of EHD2 to caveolae.

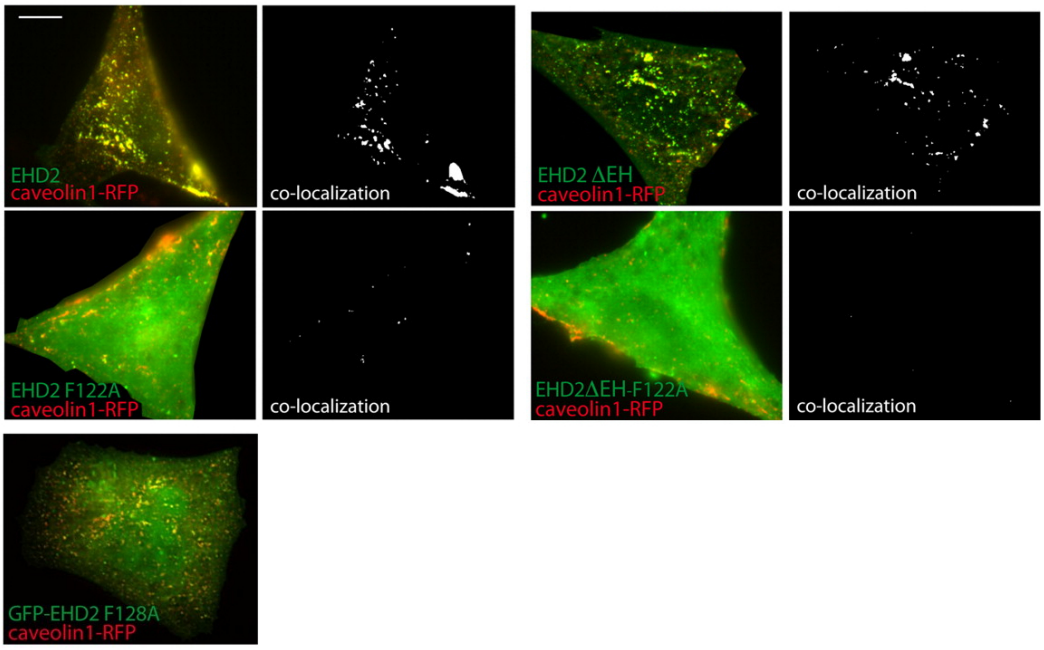

Figure 39: The KPFxxxNPF loop in EHD2 mediates targeting to caveolae. Fluorescent micrographs of 3T3-L1 cells co-expressing GFP-tagged EHD2 variants and Cav1-RFP. EHD2 ΔEH comprises residues 1-416. Figure and figure legend were taken from [150].

As already mentioned before, the EH domain most likely adopts two conformations. If located at the side-site, the EH domain binds via its second NPF-binding pocket to the KPFxxxNPF loop. This loop is located between switch I and II of the G domain.

Two single point mutations in the KPFxxxNPF loop were tested for co-localization with Cav1. Surprisingly, EHD2 F122A (KPAxxxNPF) did not co-localize with Cav1, whereas EHD2 F128A (KPFxxxNPA) still co-localized with Cav1 (Figure 39). In conclusion, the integrity of the KPF motif is required for proper targeting.

The cytosolic staining of EHD2 F122A might be explained by an impaired binding of the EH domain to the side-site, thereby inhibiting oligomerization. In order to test this, a variant lacking the EH domain and carrying the mutation F122A (EHD2 F122A ΔEH) was constructed. This mutant showed a similar cytosolic staining as EHD2 F122A and proofed that Phe122 is required for targeting even in the absence of the EH domain (Figure 39).

The NPF motif, which was not required for targeting, bound to the second NPF-binding pocket of the EH domain. In order to test whether this interaction regulates caveola dynamics, FRAP experiments with F128A (KPFxxxNPA) and S510E were conducted. S510E was predicted to close the second NPF-binding pocket of the EH domain. Indeed, F128A recovered much faster and S510E slightly faster than the wild-type (Figure 40). This indicates that switching of the EH domain regulates caveola dynamics.

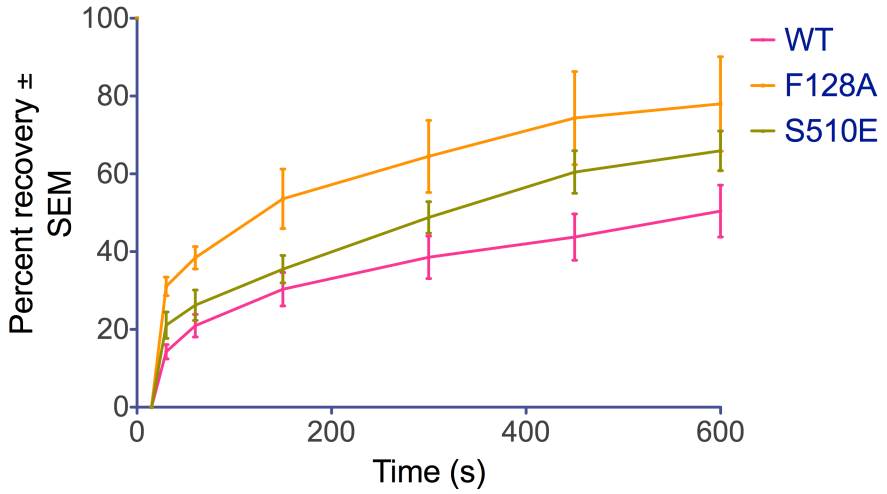

Figure 40: The interaction between the KPFxxxNPF loop and the EH domain regulates the recovery rate after photobleaching in 3T3-L1 cells. Overexpressed EHD2 F128A (KPFxxxNPA) and EHD2 S510E (predicted to close the second NPF binding pocket) were bleached for 10 s. Both mutants recover faster than the wild-type, indicating increased mobility. Figure kindly provided by Björn Morén.

3.4.5 *Binding of ATPγS is independent of the KPFxxxNPF loop*

EHD2 F122A (KPAxxxNPF) showed cytoplasmic staining, similar to EHD2 T72A, which is impaired in nucleotide binding. Therefore, the cytoplasmic staining of F122A might be explained by impaired nucleotide binding. To test this, the binding of EHD2 F122A to ATPγS was measured by isothermal titration calorimetry (ITC) as described in Section 2.4.5. At the end of the titration experiment, binding isotherms no longer decreased, indicating that saturation was reached. The binding isotherms were fitted with the one set of sites model without fixed parameters. The fit revealed K_D values for EHD2 vs. ATPγS and EHD2 F122A vs. ATPγS of 27 ± 1 and 39 ± 2 µM, respectively (Figure 41). The stoichiometry of $N = 1$ showed that one nucleotide bound one EHD2 monomer. The ITC experiments indicate that the single point mutation F122A in the KPFxxxNPF loop does not grossly affect nucleotide binding and thus impaired nucleotide binding cannot explain the cytoplasmic localization of EHD2 F122A.

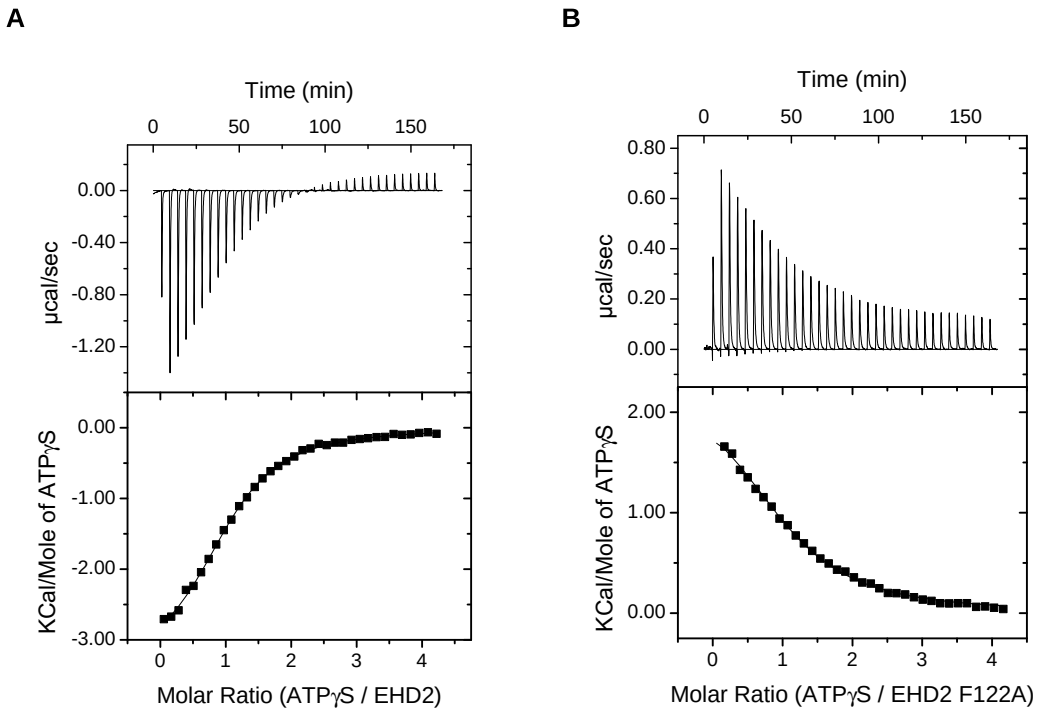

Figure 41: EHD2 bound ATPγS in the low micromolar range. **A** EHD2 wild-type bound ATPγS with a K_D of 27 ± 1 µM and **B** EHD2 F122A bound ATPγS with a K_D of 39 ± 2 µM. The stoichiometry in both cases equaled 1. Binding of ATPγS to EHD2 and EHD2 F122A is comparable. It is unclear, why the binding reaction in A is exothermic, whereas in B it is endothermic.

4

DISCUSSION

EHD2 shares a similar domain organization with other members of the dynamin superfamily of large GTPases. The dimeric, multi-domain ATPase EHD2 deforms liposomes into lipid tubules, which are decorated with an oligomeric protein coat. In the laboratory of Prof. Dr. Daumke, the ATPase cycle, a possible mechano-chemical function and the interaction between EHD2 and PACSIN2 were investigated. In cooperation with Dr. Ralf Langen, Zilkha Neurogenetic Institute, Los Angeles, California, USA, I analyzed the structural features of membrane-bound EHD2 by electron paramagnetic resonance (EPR). Membrane remodeling activity was assigned to the N-terminus, which was previously not modeled. In cooperation with Dr. Richard Lundmark, Umeå University, Medical Biochemistry and Biophysics, Umeå, Sweden, the requirements for caveolae targeting of EHD2 were dissected.

4.1 THE NUCLEOTIDE HYDROLYSIS CYCLE

Small GTPases act as molecular switches. They cycle between an GTP-bound On- and an GDP-bound Off-state. The intrinsic GTP hydrolysis rate is slow. However, GTPase-activating proteins (GAPs) stimulate the hydrolysis of GTP to GDP, thereby switching the GTPase off. Guanine Exchange Factors (GEFs) exchange GDP against GTP nucleotides, thereby switching the GTPase on. The On- and Off-state is reflected in the conformation of their switch I and II regions [221]. In the GTP-bound state the switch I region contacts the γ-phosphate. This conformation corresponds to the loaded spring conformation. After hydrolysis of GTP to GDP, the switch I region moves away from the nucleotide binding pocket, adopting the relaxed spring conformation. Most small GTPases are signaling molecules and their On- or Off-state is recognized by downstream effectors.

In machano-chemical enzymes including the dynamin family or the family of ATPases associated with various cellular activities (AAA ATPases), energy from the cleavage of the γ-phosphoanhydride bond is used in mechano-chemical processes. A good example is the AAA containing dynein, a motor protein traveling along microtubuli.

The nucleotide hydrolysis cycle of small and large GTPases was dissected by X-ray crystallography. Snapshots of the different nucleotide-loading states are recorded, eventually leading to a detailed understanding of the nucleotide hy-

drolysis cycle. Often large-scale conformational changes are observed during nucleotide hydrolysis.

4.1.1 *The ADP-bound EHD2 structure*

In this thesis, no large-scale conformational changes between the AMP-PNP- and ADP-bound form of EHD2 Q410A were observed by X-ray crystallography. However, in the ADP-bound state the switch I region moved away from the nucleotide binding pocket, when compared to the AMP-PNP-bound structure. This is consistent with the loaded spring mechanism of small GTPases [221].

Careful comparison of the crystal structures of SeMet-derivatized EHD2 L5M Q410A in the AMP-PNP- and ADP-bound forms showed two additional details, besides the previously mentioned conformational change in the switch I region. Only in the AMP-PNP-bound form, electron density for residues 1-7 and for a part of the KPFxxxNPF loop was observable. Interestingly, the anomalous signal for L5M was present in the AMP-PNP- and ADP-bound form. Possibly, the AMP-PNP-induced conformational change of the switch I region favors the EH domain - G domain interaction in the crystal, leading to an improved visibility of KPFxxxNPF loop. It remains unclear why the density for the N-terminus is more pronounced in the AMP-PNP-bound form, because strong evidence exists that the N-terminus is displaced from its hydrophobic pocket into the membrane upon liposome-mediated oligomerisation, and that ATP is required for membrane remodeling. ATP or its non-hydrolyzable analogue ATPγS is necessary for oligomerisation under stringent *in vitro* [164] and *in vivo* conditions [150]. The small conformational changes induced by AMP-PNP might be sufficient to stabilize the EH domain at the side-position and thus stabilize the oligomer. In the presence of liposomes the N-terminus retracts from its hydrophobic pocket. Additionally, retraction of the N-terminus might be coupled to nucleotide-hydrolysis. The structure of nucleotide-free EHD2 is not yet available. It is possible that the most drastic conformational changes will be found between the nucleotide-free and nucleotide-bound forms.

With the methods used in this thesis, it is not possible to exclude a mechano-chemical function of EHD2. In contrast, nucleotide stimulated release of a fluorescent dye trapped in liposomes was observed for EHD2. Improvements on sample handling for EPR (Section 5.4) and ongoing success in cryo-EM of EHD2 on lipid tubules (Section 5.1) will elucidate the mechano-chemical function.

4.1.2 *Comparison with BDLP*

The crystal structure of BDLP was solved in the nucleotide-free and GDP-bound form. Both structures superpose well, only the paddle region with the lipid-binding residues shows a rearrangement [168]. A cryo-EM reconstruction of a tubular fragment of GMP-PNP-bound BDLP lead to spectacular insights into conformational changes upon membrane- and nucleotide-binding [169]. The kinked conformation, as seen in both crystal structures, undergoes major conformational changes upon nucleotide binding and forms an elongated structure (Figure 42). Fitting of the G domain was facilitated by modeling the GMP-PNP-bound G domain using the existing GMP-PNP-bound crystal structure of the G domain of GBP1. The model of the GMP-PNP-bound G domain of BDLP reveals a tilted, tighter dimer interface.

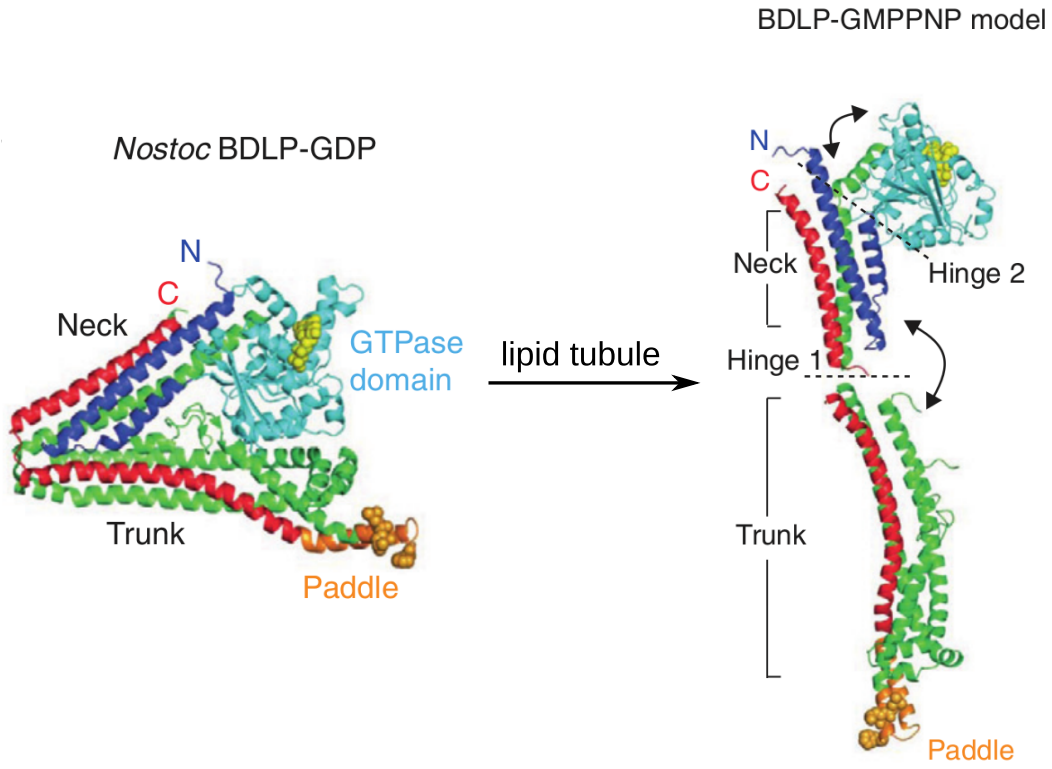

Figure 42: The crystal structure of bacterial dynamin-like protein (BDLP) from *Nostoc punctiforme* reveals a compact fold that radically extends upon lipid and GTP binding. A model of GMP-PNP- and lipid tubule associated BDLP was derived from cryo-EM data. Hinges 1 and 2, and the trunk tip represent regions of high flexibility. Figure and legend adapted from [182].

However, in the crystal structures of EHD2 in the AMP-PNP- and ADP-bound form no such changes of the G domain were observed. Note that the G domain interface in BDLP corresponds to the oligomer interface in EHD2 and therefore conformational changes might not affect the dimer interface. Nevertheless, a conformational change of the oligomer interface might affect the helices, located

N- and C-terminally of the G domain. Similar to BDLP, conformational changes caused by nucleotide hydrolysis might only be observable in the lipid-bound state.

The stalk of full-length BDLP was fitted into the cryo-EM map in a parallel fashion. However, the crystal structures of dynamin1 and MxA suggest a criss-cross arrangement of the stalk [169, 132, 133, 130, 131]. Possibly, the parallel organization of the helical regions in Atlastin1, BDLP and EHD2 is an alternative to the criss-cross organization in classical dynamins [222].

4.1.3 *Comparison with Dynamin*

The crystal structures of the isolated G domain of *Dictyostelium discoideum* dynamin A in the nucleotide-free and GDP-bound form did not show large-scale conformational changes [223]. The nucleotide-free form of the G domain from *Rattus norvegicus* dynamin1 was predicted to resemble the GTP-bound state [165]. However, new insights were gained from the structure of a minimal GED-G domain fusion of human dynamin1. The structure of this construct was solved in the presence of the non-hydrolyzable ground state analogue GMP-PCP and in the presence of the transition state analogue GDP•AlF_4^- [135, 224]. The α-helices from the GED are a part of the BSE, which connects the G domain to the stalk. Strikingly, when comparing both structures, the α-helices from the BSE are rotated by roughly 70°. This points to a power-stroke, where energy from GTP hydrolysis is transferred to the BSE.

Cryo-EM based 3D reconstructions of nucleotide-free and GMP-PCP-bound dynamin1 coated lipid tubules are available [225, 226, 224]. These reconstructions revealed conformational changes, which lead to a constricted (GMP-PCP-bound) and non-constricted (nucleotide-free) dynamin model [134]. However, conformational changes were first observed in cryo-EM based 3D reconstructions and later explained by the X-ray structures of the G domain-GED fusion.

When comparing dimerization and oligomerization of dynamin with EHD2, two major differences become clear. Dynamin dimerizes via the stalk, whereas dimerization of EHD2 involves the G domain. Oligomerization in dynamin also occurs via the stalk, and connections between adjacent rungs are mediated via dimerization of the G domains. In EHD2, oligomerization takes place via the G domain, involving the interface which is responsible for dimerization in dynamin. EHD2 crystallizes as a dimer, because oligomerization is auto-inhibited by the EH domain. Thus, the oligomer interface is not observable in the crystal structures, and nucleotide-dependent conformational changes might not be visible. A cryo-EM map of EHD2 in the ADP- and AMP-PNP-bound form could possibly reveal conformational changes, because oligomers are observed directly.

In conclusion, no fundamental changes between nucleotide-free and nucleotide-bound dynamin were foreseen from crystallographic data. Only recently, the nucleotide-bound structure of human dynamin1 GED-G domain fusion in the transition state and in the ground-state revealed a movement of the BSE. It is tempting to investigate, if co-crystallization of EHD2 with a transition state analogue reveals nucleotide-dependent conformational changes.

4.2 THE AMINO-TERMINUS OF EHD2

Membrane remodeling by N-terminal amino acid stretches, specially by those which form amphipathic helices upon membrane contact, is widely known in the literature. Also membrane interacting loops like the wedge loop in the PACSIN family contribute to membrane remodeling. In this thesis, the structure, localization and function of the N-terminus of EHD2 were analyzed. The N-terminus was integrated into the concept of membrane remodeling by shallow interactions with the membrane. In another scenario the N-terminus of EHD2 might work as a membrane curvature sensor to target dimeric EHD2 to membrane areas with a specific curvature, as proposed by Bhatia *et al.* [227] and observed for the ALPS in ArfGAP1 [91].

4.2.1 *Membrane remodeling requires the N-terminus and ATP*

It was unclear, if nucleotides and the N-terminus are required for membrane remodeling by EHD2. Liposome binding and tube formation was observed in the absence of nucleotides and with either full-length or N-terminally truncated EHD2. However, the characteristic striated protein coat around lipid tubules was predominantly observed for full-length EHD2. A similar finding was reported for endophilin, where the N-terminus is required for sharply defined striated protein coats around lipid tubules [108]. The striated pattern might indicate a regular arrangement of the oligomeric rings, indicating a function of the N-terminus of EHD2 in organization of the oligomers.

In EM, no nucleotide-dependent difference in tube morphology was found. However, quantification by EM is difficult, because certain species adhere preferentially to the EM grid. Additionally, the quality within a grid and among different grids varies. Therefore, a leakage assay for the comparison of EHD2 and EHD2$^{19\text{-}543}$ in the presence of ATP was used (Section 3.3.8). EHD2 wild-type showed ATP-dependent dye leakage, whereas EHD2$^{19\text{-}543}$ did not. This result was corroborated by the observation that the ATPase rate of full-length EHD2, but not of EHD2$^{19\text{-}543}$, was stimulated by the addition of liposomes.

Both assays show that membrane remodeling by EHD2 requires ATP and the N-terminus. However, it is not entirely clear what causes dye/quencher leakage in the leakage assay. Is leakage caused by tubulation, vesiculation or fusion? Volume and surface conservation considerations indicate that leakage occurs in all three cases [228]. So far no evidence for fusion exists. Tubulation occurs, but showed no ATP-dependence in EM under similar conditions. Thus, the most likely process observed by the leakage assay is vesiculation. Taken together, membrane remodeling by EHD2 requires the N-terminus and ATP.

In 3T3-L1 cells, an N-terminally GFP-tagged EHD2 construct lacking the N-terminus recovered after photobleaching as fast as the wild-type. This was consistent with the liposome binding assays and indicates that membrane binding in 3T3-L1 cells is not altered upon removal of the N-terminus. However, the KK6,7DD double point mutant recovered much faster, indicating that inverting the charge at the N-terminus affects membrane binding in 3T3-L1 cells. *In vitro*, EHD2 KK6,7DD and EHD2$^{19\text{-}543}$ bound lipsomes equally well as EHD2 wild-type. Taken together, knowledge from *in vitro* experiments has to be carefully transferred to cell biological experiments. In cell biology, KK6,7DD accelerates recovery of EHD2, whereas complete removal of the N-terminal stretch does not.

4.2.2 *Comparison to the small GTPases Arf1 and Sar1*

Arf1 and Sar1 possess an N-terminal amino acid stretch, which is known to induce curvature in membranes [229, 86, 84, 87]. In both cases, a movement of the interswitch region upon GTP binding displaces the N-terminus from the core of the protein. The N-terminus subsequently binds the membrane as an amphipathic helix. Using an EPR approach, a similar behavior for the N-terminus of EHD2 was observed. The N-terminus folds into a hydrophobic pocket in solution. Upon mixing with liposomes, the N-terminus of EHD2 switches to the membrane. Membrane remodeling was greatly enhanced in the presence of ATP, hinting to a nucleotide-dependent release of the N-terminus from its hydrophobic pocket. Comparing the AMP-PNP- and ADP-bound structures, a minor movement of the switch I region was observable. Under *in vivo* conditions this slight conformational change might be sufficient to release the N-terminus from its hydrophobic pocket and to displace it to the membrane.

4.2.3 *Comparison to GIMAP2*

GTPases of immunity-associated proteins (GIMAPs) are a distinctive family of large GTPases, related to the septin family. The G domain of GIMAP2 contains a C-terminal extension, an unique amphipathic helix α7. Helix α7 packs against

switch II in the nucleotide-free and GDP-bound form. Only in the absence of helix α7 and in the presence of GTP, an oligomerization interface forms in the crystals. GTP binding triggers structural rearrangements in switch II, which are predicted to weaken the association of helix α7 and the G domain, leading to the formation of the oligomerization interface [230]. Taken together, oligomerization of GIMAP2 is possibly auto-inhibited, and inhibition is released by GTP binding and displacement of helix α7.

In this thesis, it was shown that the EH domain of EHD2 binds to the KPFxxxNPF loop at the side position. Interestingly, this interaction between the second NPF binding pocket of the EH domain and the KPFxxxNPF loop was only observable in the AMP-PNP-bound crystal structure. This suggests that the structural rearrangement of switch I, caused by ATP binding, might stabilize the interaction between the EH domain and the KPFxxxNPF loop. Therefore, the previously proposed EH domain interlocking in the oligomer might be favored by ATP binding. In GIMAP2, GTP binding releases an inhibitory α-helix. In EHD2, the KPFxxxNPF loop might relocate upon ATP binding to accommodate the second NPF binding pocket. In both proteins, nucleoside triphosphate binding might form an oligomer interface.

4.3 THE EH DOMAIN ADOPTS TWO CONFORMATIONS

Following the mechanistic principle of the small GTPases Arf1 and Sar1, the interswitch region of EHD2 might contribute to nucleotide-dependent regulation. The interswitch region of EHD2 contains the KPFxxxNPF motif required for targeting of EHD2 to caveolae.

Contacts in the oligomer are not only mediated by the conserved oligomerization interface, but might be complemented by an interlocking of the EH domains. The EH domain at the top position sterically restricts oligomerization, since the C-terminal Arg536 points into the oligomerization interface close to the nucleotide-binding pocket. Arg536, although not required for nucleotide binding, might work as a nucleotide sensor, regulating oligomerization. The EH domain interlocking in the oligomer requires a movement of the EH domain from the top of one monomer to the side of the neighboring monomer. The linker is 40 amino acids long, which permits such a movement. Furthermore, when located at the side, the EH domain bound via its second NPF binding pocket to the KPFxxxNPF loop, which by itself might adopt different conformations depending on the nucleotide-loading state. The primary NPF binding pocket might be accessible to specific factors carrying an NPF motif.

Interestingly, the EH domain binding to the KPFxxxNPF loop is oriented in a fashion permissive for membrane interaction. The conserved membrane interacting residues R488, K491 and R497 face the membrane and R488 was shown

to interact with the lipid headgroups. In conclusion, the EH domain movement as postulated by Daumke *et al.* is correct [164]. Here, the correct orientation of the EH domain at the side position was discovered. An interaction of the second NPF binding pocket with the KPFxxxNPF motif was proposed. Furthermore, residues located in vicinity to the primary NPF binding pocket are ideally located for membrane interaction.

4.4 FUNCTION OF EHD2 AT CAVEOLAE

Stoeber *et al.* confirmed co-localization of EHD2 wild-type with Cav1, and targeting defects of the EHD2 double mutant F122A/F128A (KPAxxxNPA). In contrast to the results presented here, they observe targeting defects for the EHD2 ΔEH construct [219]. Note that Stoeber *et al.* used different cell lines and different tagging strategies, namely CV1 cells and C-terminally tagged EHD2-EGFP fusions. My collaborators used 3T3-L1 cells with N-terminally tagged EGFP-EHD2 fusions. CV1 cells are derived from monkey kidneys and 3T3-L1 cells from mouse fibroblasts. Abundance and type of caveolae might differ in those cell lines. The N-terminal GFP-tag used in the studies presented in this thesis might hinder the N-terminus from interactions with the membrane. The C-terminal GFP-tag might instead restrict the movement of the EH domain and therefore change the oligomerization behavior of EHD2. Possible ways to circumvent tagging-artifacts are described in Section 5.5.

It was shown that EHD2 is a stable component of caveolae, whereas PACSIN2 only temporarily associates with a subset of caveolae [111, 150]. Dynamin was previously shown to be present at caveola necks [231, 232]. During caveola endocytosis, the stable caveolar component EHD2 might deform the membrane into a fission-competent shape. EHD2, via its EH domain, might recruit PACSIN2, which temporarily stabilizes the membrane curvature. PACSIN2 in turn might recruit dynamin via its SH3 domain and thereby promote scission of caveolae.

4.5 MODEL OF MEMBRANE DEFORMATION BY EHD2

A recent publication shows that the N-terminus of several N-BAR proteins triggers vesiculation of liposomes, and that the BAR domain scaffold promotes tubulation of liposomes [96]. Thus, vesiculation and tubulation are separated into two tasks. In EHD2, the N-terminus was required for vesiculation, but tubulation even occurred in the absence of the first 18 amino acids and ATP. Therefore, it was speculated that after tubulation of liposomes by a scaffold composed of the lipid binding site of EHD2, vesiculation requires the N-terminus and is triggered by ATP. Under physiological ATP concentrations of 1-10 mM, EHD2 tubules are

unlikely to form, because vesiculation would be triggered before long tubules could form.

The *in vitro* data can be summarized in the following model (Figure 43). In solution, EHD2 is found in its dimeric form. The EH domain sits on top of the opposing monomer, with its primary NPF binding pocket bound to the GPF motif situated in the linker between the helical domain and the EH domain. At this position the EH domains inhibits oligomerization. The N-terminus binds to a hydrophopic pocket at the side of the G domain and the NPF motif from the KPFxxxNPF loop is not occupied. Upon addition of liposomes, EHD2 undergoes a structural reorganization. Oligomers are formed and concomitantly the N-terminus switches from its hydrophopic pocket into the membrane. The EH domain moves from the top position to the NPF motif at the side of the G domain from the next dimer. The membrane is contacted by the lipid binding site, the N-terminus and the EH domain. A scaffold formed by the lipid binding site is sufficient to deform liposomes into tubules. Vesiculation occurs after the addition of ATP and is mediated by the membrane remodeling activity of the N-terminus.

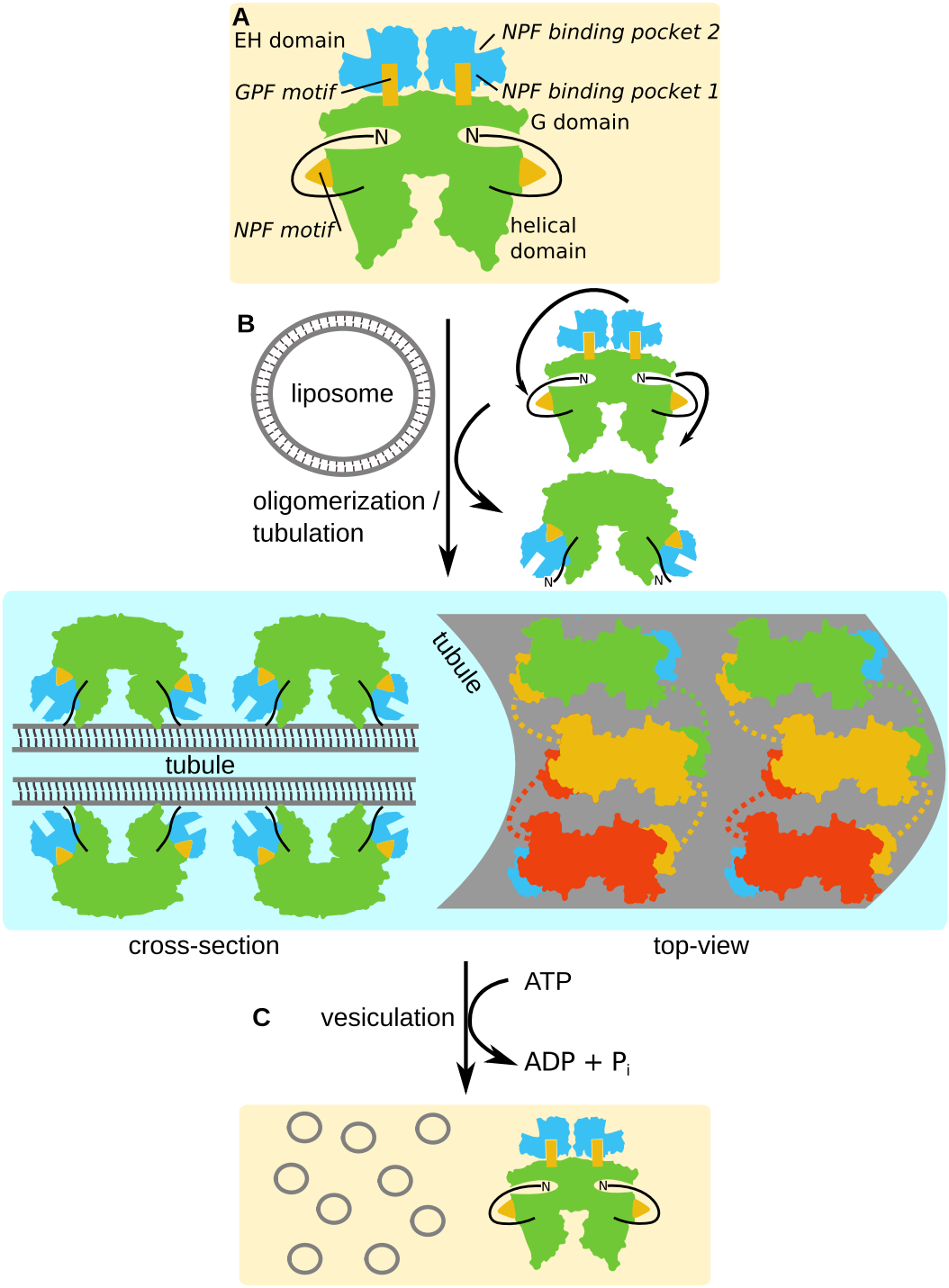

Figure 43: Model of membrane binding and remodeling by EHD2. The G and helical domain are shown in green, the EH domain in blue. GPF (orange rectangles) and NPF motifs (orange triangles) are indicated. The N-terminus is depicted as a black solid line. **A** Dimeric EHD2 in solution with important structural features annotated. **B** EHD2 deforms liposomes into tubules and forms an oligomeric coat. Structural rearrangements including a movement of the EH domain and relocation of the N-terminus are indicated. A cross-section and a top view of an EHD2 coated membrane tubule is shown. In the top view, EHD2 dimers are shown in different colors and the EH domain interlocking is visualized. The flexible linker connecting the EH domain to the helical domain is depicted as a dashed line. **C** EHD2 vesiculates membrane tubules with its N-terminus upon addition of ATP.

5

OUTLOOK

5.1 EM RECONSTRUCTION

A model of an oligomeric ring composed of twenty EHD2•AMP-PNP dimers was previously proposed. The dimensions of the ring, with an inner diameter of ≈ 18 nm and a height of ≈ 10 nm, are in agreement with negative stain EM tubulation assays (Figure 44) [164]. The observed inter-ring distances were confirmed by a computational model, in which membrane deformation caused by EHD2 oligomers disfavors rings in close vicinity [233]. This could explain the regular arrangement of the rings.

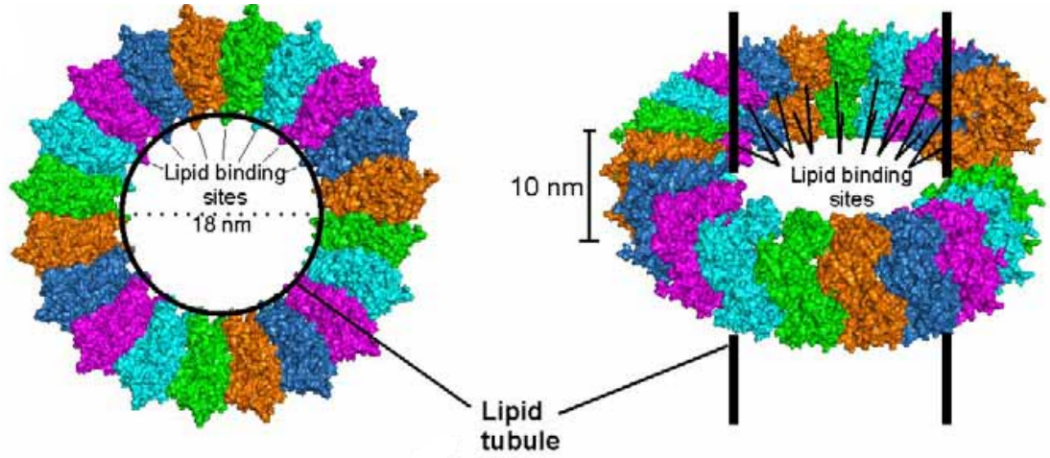

Figure 44: Model of the EHD2 oligomeric ring. Top and side view of the EHD2 oligomeric ring model in a surface representation. For better clarity, the EH domains are not included. The diameter of the embraced lipid tubules is ≈ 18 nm and the thickness of the EHD2 ring is ≈ 10 nm, in agreement with what is observed in the EM assays. Approximately twenty EHD2 dimers constitute one turn in this model. Figure and legend adapted from [164].

The cryo-EM reconstruction of dynamin in the unconstricted state (nucleotide-free) and constricted state (GMP-PCP-bound) helped tremendously in building oligomeric ring models of dynamin by fitting existing related crystal structures into the cryo-EM map [225, 134, 224, 130, 131]. Similarly, a cryo-EM map of EHD2 in both the nucleotide-free and -bound forms would aid in understanding the molecular function of nucleotide hydrolysis. During my thesis I unsuccessfully tried to optimize the negative stain EM conditions to such an extent, that 3D-reconstructions would be feasible. Initial attempts using cryo-EM in cooperation with the group of Prof. Dr. Christian Spahn, Charité, Berlin failed. Recently,

however, first cryo-EM images for EHD2 bound to lipid tubules have been observed (Figure 45). A three-dimensional EM-reconstruction of membrane bound EHD2 might be possible in the future.

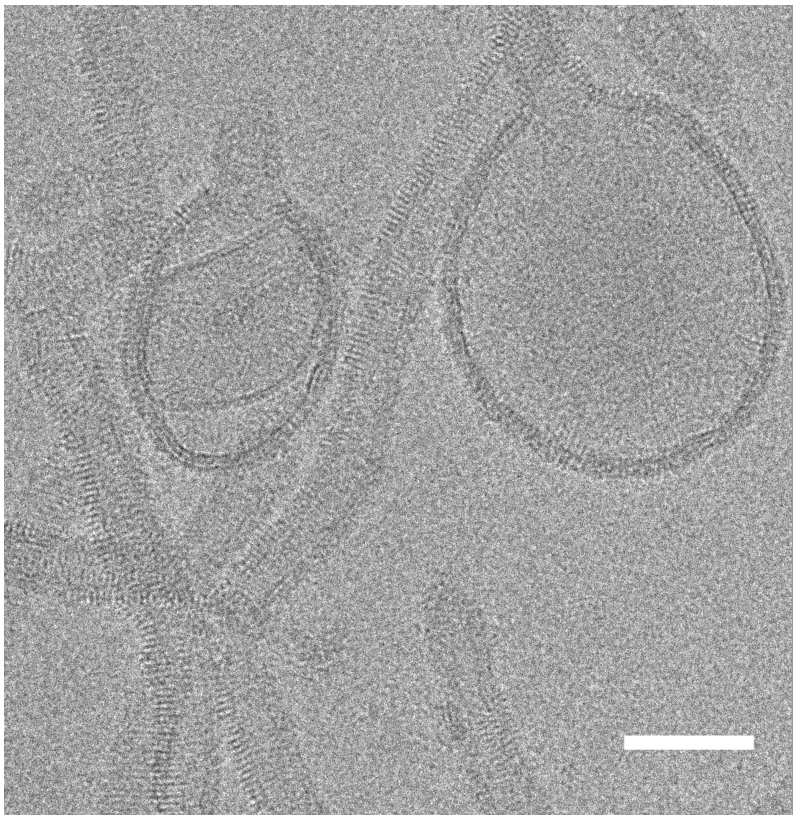

Figure 45: Cryo electron micrograph showing 800 nm extruded Folch-liposomes decorated with 80 µM EHD2 after 15 min incubation at RT in the presence of ATP. Note, that not all decorated liposomes are deformed into tubules. Scale bar represents 100 nm. Image kindly provided by Elmar Behrmann.

5.2 EHD2 KNOCK-OUT MICE

A knock-out of EHD1 in mice resulted in a reduced rate of endocytosis [147] and defects in spermatogenesis and male fertility [148]. Mice without EHD4 showed a 50 % reduced testis weight [149]. Thus, EHD1 and EHD4 might have a functional overlap, as predicted earlier [142]. In this thesis it was shown that EHD2, the sole isoform predominantly expressed in heart and skeletal muscle [142], is a component of caveolae [150, 219], and the membrane repair system in muscle cells [163]. In cooperation with Dr. Ines Lahmann from the group of Prof. Dr. Carmen Birchmeier, MDC, Berlin, a conditional EHD2 knock-out mouse will be generated and characterized.

5.3 EPR DISTANCE MEASUREMENTS ON LIPID TEMPLATES

In this thesis, EPR was employed successfully to assign membrane binding function to specific residues, since subtle differences in membrane affinity are not detectable by spin assays. Additionally, distances between two spin probes by pulsed EPR methods were measured, and the position of a specific residue in relation to other residues in the crystal structure was calculated. Transferring this know-how on lipid-bound EHD2 or other large membrane remodeling assemblies will allow tracking of conformational changes upon liposome binding. The determination of the monomer exchange rate allows the dilution of oligomers with unlabeled monomers, a prerequisite for obtaining distances within the building blocks of the oligomer. Relating EPR distance restraints to crystal structures was greatly improved by *in silico* modeling of the spin label position using MMM2011[1] [201] or PRONOX[2] [202]. Feeding these restraints to modeling tools like DireX[3] [234] it will be possible to generate a model of liposome-bound EHD2. DireX allows molecular simulations of crystal structures with additional distance restraints upon preserving the secondary structure elements. Preliminary data obtained from the EHD2 dimer in solution suggested that the helical domain might rotate at the hinge region between the G and helical domains and generate a more elongated structure, resembling a BAR domain.

5.4 EPR AS A TOOL TO STUDY NUCLEOTIDE-MEDIATED CONFORMATIONAL CHANGES

Previously, no nucleotide-dependent conformational changes in EHD2 were detected by EPR. Recently, however, these changes were observed for the first time. EHD2's sensitivity on nucleotide binding critically depended on the thawing procedure of cryo-stored EHD2. The protein required careful thawing on ice and addition of pre-cooled buffer. With this method it was possible to observe different conformations of a residue located in the G domain depending on the nucleotide-loading state. The nucleotide-sensitivity was undetectable after adding buffer at RT directly to the cryo-stored protein. Tubulation assays were not affected by the cold/warm buffer issue. For all other experiments EHD2 was thawed carefully on ice and diluted with pre-cooled buffer.

1 http://www.epr.ethz.ch/software/index
2 http://rockscluster.hsc.usc.edu/research/software/pronox/pronox.html
3 http://www.schroderlab.org/software/direx/index.html

5.5 CELL BIOLOGY

Cell biological results from Morén *et al.* and Stoeber *et al.* demonstrated that EHD2 co-localizes with caveolin, but only in one study targeting of EHD2 to caveolae required the EH domain [150, 219]. Possibly, the discrepancy was caused by different tagging strategies employed in the two studies.

To avoid tagging-artifacts, untagged EHD2 could be over-expressed and subsequently detected using polyclonal α-EHD2 antibodies. Unfortunately, the detection by antibodies requires fixing and permeabilization of the cells, making live-cell imaging or FRAP experiments impossible. For these types of experiments fluorescent labeled EHD2 could be injected into the cells. A fluorescent dye, e.g. Alexa 488 (721 Da), is much smaller than a GFP-tag (30 kDa) and therefore should not interfere with cellular localization or FRAP analysis.

APPENDIX A - LIST OF MATERIALS

Table 11: Instruments used in this study

INSTRUMENT	MANUFACTURER
Thermocycler TGradient	Biometra, Göttingen, D
Thermocycler TPersonal	Biometra, Göttingen, D
Agarose Gel Electrophoresis System	OLS, Bremen, D
SDS PAGE System Xcell Sure Lock	Invitrogen, Darmstadt, D
Western Blot Module Xcell II	Invitrogen, Darmstadt, D
Thermomixer Comfort	Eppendorf, Hamburg, D
Amicon centrifugal filter devices	Millipore, Billerica, USA
Photometer BioPhotometer	Eppendorf, Hamburg, D
Photometer NanoDrop 2000	Thermo Scientific, Dreieich, D
Benchtop Centrifuge 5415 R	Eppendorf, Hamburg, D
Benchtop Centrifuge 5415 D	Eppendorf, Hamburg, D
Benchtop Centrifuge 5804 R	Eppendorf, Hamburg, D
Fluidizer M-110L Pneumatic	Microfluidics, Newton, USA
Centrifuge Avanti J-26 XP	Beckman Coulter, Krefeld, D
Ultracentrifuge Optima L-100K	Beckman Coulter, Krefeld, D
Ultracentrifuge Optima TLX	Beckman Coulter, Krefeld, D
Chromatography column GSTrap HP 1 mL	GE Healthcare, Piscataway, USA
Chromatography column HisTrap HP 1 mL	GE Healthcare, Piscataway, USA
Chromatography column material GSH Sepharose 4B	GE Healthcare, Piscataway, USA
Chromatography column material Ni Sepharose HP	GE Healthcare, Piscataway, USA
Chromatography columns Superdex 75 16/60, 26/60	GE Healthcare, Piscataway, USA
Chromatography columns Superdex 200 16/60, 26/60	GE Healthcare, Piscataway, USA
Chromatography columns XK 16/20, XK 26/20	GE Healthcare, Piscataway, USA
Desalting columns PD-10	GE Healthcare, Piscataway, USA
Peristaltic Pump Reglo Analog ISM827B	Ismatec, Glattbrugg, CH

Table 11 – Continued on next page

Table 11 – Continued

INSTRUMENT	MANUFACTURER
Äkta Prime Plus	GE Healthcare, Piscataway, USA
Äkta FPLC	GE Healthcare, Piscataway, USA
Äkta Purifier	GE Healthcare, Piscataway, USA
RALS Viscotec RImax	Malvern, Malvern, UK
DLS Zetasizer Nano ZS90	Malvern, Malvern, UK
CD spectropolarimeter J-720	Jasco, Tokyo, J
HPLC Infinity 1260	Agilent Technologies, Santa Clara, USA
Hypersil ODS guard column	Agilent Technologies, Santa Clara, USA
Reversed-phase ODS-2 Hypersil HPLC column	Thermo Scientific, Dreieich, D
Isothermal Titration Calorimeter VP-ITC	GE Healthcare, Piscataway, USA
Fluorescence Spectrophotometer Varian Cary Eclipse	Agilent Technologies, Santa Clara, USA
pH-Meter	Mettler-Toledo, Gießen, D
Scales	Sartorius, Göttingen, D
Shaker Incubator Innova44	New Brunswick Scientific, Edison, USA
Matrix Hydra II 96-well liquid handling system	Thermo Scientific, Dreieich, D
crystallization plate storage and imaging system Rock Imager	Formulatrix, Waltham, USA
EPR Spectrometer Elexsys E500	Bruker BioSpin, Billerica, USA
EPR Spectrometer Elexsys E580	Bruker BioSpin, Billerica, USA
Binocular Microscope MZ 7.5	Leica, Wetzlar, D
Zeiss EM910	Carl Zeiss, Oberkochen, D

Table 12: Enzymes used in this study

ENZYME	MANUFACTURER
DNAse I	Roche, Mannheim, D
GST-PreScission Protease	GE Healthcare, Piscataway, USA
Pfu DNA Polymerase	EURx, Gdansk, PL
Restiction Endonucleases	New England Biolabs, Frankfurt am Main, D
T4 DNA Ligase	New England Biolabs, Frankfurt am Main, D

Table 13: Kits used in this study

KIT	MANUFACTURER
2-Log DNA ladder	New England Biolabs, Frankfurt am Main, D
Unstained Protein Molecular Weight Marker	Fermentas, St. Leon-Rot, D
Mark 12 unstained protein standard	life technologies, Carlsbad, USA
Bradford protein assay	Bio-Rad, München, D
GeneAmp dNTPs	Roche, Mannheim, D
NuPAGE LDS Sample Buffer (4x)	life technologies, Carlsbad, USA
NuPAGE MES SDS Buffer	life technologies, Carlsbad, USA
NuPAGE MOPS SDS Buffer	life technologies, Carlsbad, USA
NuPAGE Novex 4-12% Bis-Tris	life technologies, Carlsbad, USA
QIAprep Spin Miniprep Kit	Qiagen, Hilden, D
QIAquick PCR Purification Kit	Qiagen, Hilden, D
QIAquick Gel Extraction Kit	Qiagen, Hilden, D
QuickChange	Agilent Technologies, Santa Clara, USA
Additive Screen	Hampton Research, Aliso Viejo, USA
The Classics Suite	Qiagen, Hilden, D
The JSCG+ Suite	Qiagen, Hilden, D
The PEGs Suite	Qiagen, Hilden, D
The PEGs II Suite	Qiagen, Hilden, D
The ProComplex Suite	Qiagen, Hilden, D

Table 14: Media

MEDIUM	COMPONENTS
Luria-Bertani (LB)	5 g/l yeast extract
	10 g/l tryptone
	5 g/l NaCl
M9 minimal medium	12.8 g/l Na_2HPO_4
	4 g/l KH_2PO_4
	1 g/l NaCl
	50 mg/l EDTA
	5 mg/l $FeSO_4$
	0.5 mg/l $ZnCl_2$
	0.1 mg/l $CoSO_4$
	0.1 mg/l $CuCl_2$
	0.1 mg/l H_3 BO_3
	1 mM $MgSO_4$
	0.3 mM $CaCl_2$
	2 g/l glucose
	0.5 g/l NH_4Cl
	1.5 mg/l Thiamin
	1.5 mg/l Biotin
Terrific Broth (TB)	ordered from Carl Roth (HP61.1)
Auto Induction Medium (AIM)	ordered from Merck (71491-5)

Table 15: Buffers

BUFFER	COMPONENTS
Hexahistidine-tagged proteins	
Resuspension buffer	50 mM HEPES pH 7.5
	400 mM NaCl
	2.8 mM β-mercaptoethanol
	250 µM Pefabloc
	1 µg/mL DNase I
	1 mM $MgCl_2$
	25 mM imidazole
Equilibration buffer	20 mM HEPES pH 7.5
	300 mM NaCl
	2.8 mM β-mercaptoethanol
	25 mM imidazole
Washing buffer	20 mM HEPES pH 7.5
	700 mM NaCl
	2.8 mM β-mercaptoethanol
	30 mM imidazole
	5 mM KH_2 PO_4
	5 mM K_2 HPO_4
	0.5 mM ATP
Elution buffer	20 mM HEPES pH 7.5
	300 mM NaCl
	2.8 mM β-mercaptoethanol
	300 mM imidazole
GST-tagged proteins	
Resuspension buffer	50 mM HEPES pH 7.5
	400 mM NaCl
	2.5 mM DTT
	250 µM Pefabloc
	1 µg/mL DNase I
	1 mM $MgCl_2$
Equilibration buffer	20 mM HEPES pH 7.5
	300 mM NaCl
	2.5 mM DTT
Washing buffer	20 mM HEPES pH 7.5
	700 mM NaCl

Table 15 – Continued on next page

Table 15 – Continued

BUFFER	COMPONENTS
	2.5 mM DTT
	5 mM KH_2 PO_4
	5 mM K_2 HPO_4
	0.5 mM ATP
Elution buffer	20 mM HEPES pH 7.5
	300 mM NaCl
	2.5 mM DTT
	20 mM glutathione
SEC buffer	20 mM HEPES pH 7.5
	300 mM NaCl
	2.5 mM DTT
CD buffer	20 mM phosphate buffer pH 7,5
	300 mM NaF
	2 mM DTT
RALS buffer	20 mM HEPES pH 7,5
	150 mM NaCl
	2.5 mM DTT
	2 mM $MgCl_2$
	1 mM $CaCl_2$
HPLC buffer	100 mM KH_2 PO_4
	100 mM K_2 HPO_4
	10 mM TBAB
	7.5% (v/v) Acetonitril
Liposome buffer I	20 mM HEPES pH 7.5
	300 mM NaCl
	0.5 mM $MgCl_2$
Liposome buffer II	10 mM HEPES pH 7.5
	1 mM EDTA

Table 16: Constructs used in this study

VECTOR	PROTEIN	LENGTH	MUTATIONS
Mus musculus EHD2 mutants for crystallization			
pSKB2-LNB	mmEHD2	1-543	Q410A
pSKB2-LNB	mmEHD2	1-543	L5M, Q410A

Table 16 – Continued on next page

Table 16 – Continued

VECTOR	PROTEIN	LENGTH	MUTATIONS
pSKB2-LNB	mmEHD2	1-543	QR13,14YY, Q410A
pSKB2-LNB	mmEHD2	1-543	E91Y, Q410A
pSKB2-LNB	mmEHD2	1-543	VF321,322YY, K328A, Q410A
pSKB2-LNB	mmEHD2	1-543	K375Y, K377YY, Q410A
pSKB2-LNB	mmEHD2	1-543	EDGEE432-437YYGYY, Q410A
pSKB2-LNB	mmEHD2	1-543	E518Y, Q410A
pSKB2-LNB	mmEHD2	1-543	QR13,14YY, E91Y, K328A, Q410A
pSKB2-LNB	mmEHD2	1-543	QR13,14YY, E91Y, K328A, K375Y, K377Y, Q410A
pSKB2-LNB	mmEHD2	1-543	QR13,14YY, E91Y, K328A, Q410A, E518Y
pSKB2-LNB	mmEHD2	1-543	QR13,14YY, E91Y, K328A, K375Y, K377Y, Q410A, E518Y
pSKB2-LNB	mmEHD2	1-543	QR13,14YY, E91Y, VF321/322YY, K328A, K375Y, K377Y, Q410A, E518Y
pSKB2-LNB	mmEHD2	1-543	QR13,14YY, E91Y, K328A, Q410A, EDGEE432-437YYGYY, E518Y
pSKB2-LNB	mmEHD2	1-543	QR13,14YY, E91Y, K328A, K375Y, K377Y, Q410A, EDGEE432-437YYGYY, E518Y
pSKB2-LNB	mmEHD2	1-543	QR13,14YY, E91Y, VF321/322YY, K328A, K375Y, K377Y, Q410A, EDGEE432-437YYGYY, E518Y
pSKB2-LNB	mmEHD2	1-543	EK119,120AA, Q410A
pSKB2-LNB	mmEHD2	1-543	KKE315-317AAA, Q410A
pSKB2-LNB	mmEHD2	1-543	KENK324-327AANA, Q410A
pSKB2-LNB	mmEHD2	1-543	EELE400-403AALA, Q410A
pSKB2-LNB	mmEHD2	1-543	EEGSE435-439SSGSS, Q410A
pSKB2-LNB	mmEHD2	1-543	KENK324-327AANA, EELE400-403AALA, Q410A
pSKB2-LNB	mmEHD2	1-543	KENK324-327AANA, EEGSE435-439SSGSS, Q410A
EHD family constructs			
pSKB2-LNB	mmEHD1	1-534	
pEGFP-C3-MCS	mmEHD2	1-543	
pSKB2-LNB	mmEHD3	1-535	
pSKB2-LNB	mmEHD4	1-541	

Table 16 – Continued on next page

Table 16 – Continued

VECTOR	PROTEIN	LENGTH	MUTATIONS
pSKB2-LNB	mmEHD2	1-543	L5D
pSKB2-LNB	mmEHD2	1-543	KK6,7DD
pEGFP-C3-MCS	mmEHD2	1-543	KK6,7DD
pSKB2-LNB	mmEHD2	1-543	K120N
pEGFP-C3-MCS	mmEHD2	1-416	F122A
pSKB2-LNB	mmEHD2	1-543	F122A
pSKB2-LNB	mmEHD2	1-543	F128A
pSKB2-LNB	mmEHD2	1-543	G420N
pSKB2-LNB	mmEHD2	1-543	F422A
pEGFP-C3-MCS	mmEHD2	1-543	G487L
pEGFP-C3-MCS	mmEHD2	1-543	R488D
pEGFP-C3-MCS	mmEHD2	1-543	K491D
pEGFP-C3-MCS	mmEHD2	1-543	R497D
pEGFP-C3-MCS	mmEHD2	1-543	S510E
pSKB2-LNB	mmEHD2	19-543	ΔN-terminus
pEGFP-C3-MCS	mmEHD2	19-543	ΔN-terminus
pEGFP-C3-MCS	mmEHD2	1-416	ΔEH domain
pSKB2-LNB	mmEHD1	56-288	G domain
pSKB2-LNB	mmEHD2	56-288	G domain
pSKB2-LNB	mmEHD2	1-543	G domain, PP Cleavage Site: LPRH288-LEVLFQGP-289AALR, Q410A
pSKB2-LNB	hsEHD2	56-288	G domain
pSKB2-LNB	hsEHD3	56-288	G domain
pSKB2-LNB	mmEHD4	59-291	G domain
pSKB2-LNB	tgEHD	59-290	G domain
pSKB2-LNB	mmEHD1	288-404	helical domain
pSKB2-LNB	mmEHD2	288-404	helical domain
pSKB2-LNB	hsEHD2	288-404	helical domain
pSKB2-LNB	hsEHD3	288-404	helical domain
pSKB2-LNB	mmEHD4	291-407	helical domain
pSKB2-LNB	tgEHD	290-405	helical domain
pGEX-6P-1	mmEHD1	56-288	G domain
pGEX-6P-1	mmEHD2	56-288	G domain
pGEX-6P-1	hsEHD2	56-288	G domain

Table 16 – Continued on next page

Table 16 – Continued

VECTOR	PROTEIN	LENGTH	MUTATIONS
pGEX-6P-1	hsEHD3	56-288	G domain
pGEX-6P-1	mmEHD4	59-291	G domain
pGEX-6P-1	tgEHD	59-290	G domain
pGEX-6P-1	mmEHD1	288-404	helical domain
pGEX-6P-1	mmEHD2	288-404	helical domain
pGEX-6P-1	hsEHD2	288-404	helical domain
pGEX-6P-1	hsEHD3	288-404	helical domain
pGEX-6P-1	mmEHD4	291-407	helical domain
pGEX-6P-1	tgEHD	290-405	helical domain
pGEX-6P-1	mmEHD2	440-543	EH domain
Mus musculus EHD2 cysteine mutants			
pSKB2-LNB	mmEHD2	1-543	C96S, C138S, C356S
pSKB2-LNB	mmEHD2	1-543	F2C (C96S, C138S, C356S)
pSKB2-LNB	mmEHD2	1-543	F2C, KK6,7DD (C96S, C138S, C356S)
pSKB2-LNB	mmEHD2	1-543	F2C, L28C (C96S, C138S, C356S)
pSKB2-LNB	mmEHD2	1-543	F2C, L294C (C96S, C138S, C356S)
pSKB2-LNB	mmEHD2	1-543	F2C, L303C (C96S, C138S, C356S)
pSKB2-LNB	mmEHD2	1-543	F2C, Y313C (C96S, C138S, C356S)
pSKB2-LNB	mmEHD2	1-543	S3C (C96S, C138S, C356S)
pSKB2-LNB	mmEHD2	1-543	S3C, KK6,7DD (C96S, C138S, C356S)
pSKB2-LNB	mmEHD2	1-543	W4C (C96S, C138S, C356S)
pSKB2-LNB	mmEHD2	1-543	L5C (C96S, C138S, C356S)
pSKB2-LNB	mmEHD2	1-543	L5C, L28C (C96S, C138S, C356S)
pSKB2-LNB	mmEHD2	1-543	L5C, L294C (C96S, C138S, C356S)
pSKB2-LNB	mmEHD2	1-543	L5C, L303C (C96S, C138S, C356S)
pSKB2-LNB	mmEHD2	1-543	L5C, Y313C (C96S, C138S, C356S)
pSKB2-LNB	mmEHD2	1-543	K6C (C96S, C138S, C356S)
pSKB2-LNB	mmEHD2	1-543	K7C (C96S, C138S, C356S)
pSKB2-LNB	mmEHD2	1-543	K7C, L303C (C96S, C138S, C356S)
pSKB2-LNB	mmEHD2	1-543	G8C (C96S, C138S, C356S)
pSKB2-LNB	mmEHD2	1-543	G9C (C96S, C138S, C356S)
pSKB2-LNB	mmEHD2	1-543	G9C, KK6,7DD (C96S, C138S, C356S)
pSKB2-LNB	mmEHD2	1-543	L28C (C96S, C138S, C356S)
pSKB2-LNB	mmEHD2	1-543	L28C, L303C (C96S, C138S, C356S)
pSKB2-LNB	mmEHD2	1-543	C138S, C356S
pSKB2-LNB	mmEHD2	1-543	C356S

Table 16 – Continued on next page

Table 16 – Continued

VECTOR	PROTEIN	LENGTH	MUTATIONS
pSKB2-LNB	mmEHD2	1-543	C138S
pSKB2-LNB	mmEHD2	1-543	C96S, C356S
pSKB2-LNB	mmEHD2	1-543	C96S
pSKB2-LNB	mmEHD2	1-543	C96S, C138S
pSKB2-LNB	mmEHD2	1-543	M237C (C96S, C138S, C356S)
pSKB2-LNB	mmEHD2	1-543	D277C (C96S, C138S, C356S)
pSKB2-LNB	mmEHD2	1-543	L294C (C96S, C138S, C356S)
pSKB2-LNB	mmEHD2	1-543	L294C, Y313C (C96S, C138S, C356S)
pSKB2-LNB	mmEHD2	1-543	L303C (C96S, C138S, C356S)
pSKB2-LNB	mmEHD2	1-543	L303C (C138S, C356S)
pSKB2-LNB	mmEHD2	1-543	L303C (C96S, C356S)
pSKB2-LNB	mmEHD2	1-543	L303C, K328C (C96S, C138S, C356S)
pSKB2-LNB	mmEHD2	1-543	L303C (C96S, C138S)
pSKB2-LNB	mmEHD2	1-543	Y313C (C96S, C138S, C356S)
pSKB2-LNB	mmEHD2	1-543	T320C (C96S, C138S, C356S)
pSKB2-LNB	mmEHD2	1-543	G323C (C96S, C138S, C356S)
pSKB2-LNB	mmEHD2	1-543	K324C (C96S, C138S, C356S)
pSKB2-LNB	mmEHD2	1-543	K328C (C96S, C138S, C356S)
pSKB2-LNB	mmEHD2	1-543	L331C (C96S, C138S, C356S)
pSKB2-LNB	mmEHD2	1-543	L333C (C96S, C138S, C356S)
pSKB2-LNB	mmEHD2	1-543	V337C (C96S, C138S, C356S)
pSKB2-LNB	mmEHD2	1-543	A340C (C96S, C138S, C356S)
pSKB2-LNB	mmEHD2	1-543	T474C (C96S, C138S, C356S)
pSKB2-LNB	mmEHD2	1-543	T474C (C96S, C356S)
pSKB2-LNB	mmEHD2	1-543	R488C (C96S, C138S, C356S)
pSKB2-LNB	mmEHD2	1-543	F122A, R488C (C96S, C138S, C356S)
pSKB2-LNB	mmEHD2	1-543	K491C (C96S, C138S, C356S)
pSKB2-LNB	mmEHD2	1-543	F122A, K491C (C96S, C138S, C356S)
pSKB2-LNB	mmEHD2	1-543	R497C (C96S, C138S, C356S)
pSKB2-LNB	mmEHD2	1-543	F122A, R497C (C96S, C138S, C356S)
pSKB2-LNB	mmEHD2	1-543	E514C (C96S, C138S, C356S)
pSKB2-LNB	mmEHD2	1-543	E514C (C96S, C356S)
pSKB2-LNB	mmEHD2	1-543	R537C (C96S, C138S, C356S)
pSKB2-LNB	mmEHD2	1-543	R537C (C138S, C356S)
pSKB2-LNB	mmEHD2	1-543	R537C (C96S, C356S)
pSKB2-LNB	mmEHD2	1-543	R537C (C96S, C138S)

Mus musculus PACSIN2 constructs

Table 16 – Continued on next page

Table 16 – Continued

VECTOR	PROTEIN	LENGTH	MUTATIONS
pGEX-2T	mmPACSIN2	1-486	
pGEX-6P-1	mmPACSIN2	1-486	
pCMV-Myc	mmPACSIN2	1-486	
pGEX-6P-1	mmPACSIN2	1-486	
pGEX-6P-1	mmPACSIN2	1-486	S313E
pCMV-Myc	mmPACSIN2	1-486	F364A
pCMV-Myc	mmPACSIN2	1-486	F419A
pCMV-Myc	mmPACSIN2	1-486	F364A, F407A
pCMV-Myc	mmPACSIN2	1-486	F364A, F419A
pCMV-Myc	mmPACSIN2	1-486	F407A, F419A
pCMV-Myc	mmPACSIN2	1-486	F364A, F407A, F419A
pGEX-2T	mmPACSIN2	1-486	F364A, F407A, F419A
pGEX-6P-1	mmPACSIN2	1-339	F-BAR
pGEX-6P-1	mmPACSIN2	1-339	F-BAR, S313E
pGEX-6P-1	mmPACSIN2	1-425	ΔSH3
pCMV-Myc	mmPACSIN2	1-425	ΔSH3
pGEX-2T	mmPACSIN2	1-486	ΔSH3, PP Cleavage Site: 425-LEVLFQGP-426
pGEX-6P-1	mmPACSIN2	340-486	SH3
pGEX-6P-3	mmPACSIN2	387-486	Myc-SH3

B

APPENDIX B - MATHEMATICAL BACKGROUND FOR FITTING OF MONOMER EXCHANGE

In Section 2.4.9 monomer exchange data for EHD2 was fitted with a first-order exponential decay function. Donor-labeled EHD2 dimers and acceptor-labeled EHD2 dimers were combined and the formation of mixed dimers was detected via FRET. Here, PD Dr. Martin Falcke explains mathematically, why mixed-dimer formation was approximated by a first-order exponential decay function:

SPECIES	ABBREVIATION FOR CONCENTRATION	INITIAL CONDITION AT TIME $t = 0$
Donor monomer	D	$D(0) = 0$
Total donor monomer	D_0	D_0
Donor dimer	D_2	$2D_2 = D_0$
Acceptor monomer	A	$A(0) = 0$
Total acceptor monomer	A_0	A_0
Acceptor dimer	A_2	$2A_2 = A_0$
Donor-Acceptor-Complexes		
AD	C	$C(0) = 0$
DA	E	$E(0) = 0$
$AD + DA$	F	$F(0) = 0$

Conservation relation:

$$A_0 = 2A_2 + A + C + E = 2A_2 + A + F \qquad D_0 = 2D_2 + D + F$$

Reactions and dynamics:

$$A_2 \xrightarrow{k^-} 2A \qquad A_2 \xleftarrow{k^+} 2A \qquad D_2 \xrightarrow{k^-} 2D \qquad D_2 \xleftarrow{k^+} 2D$$

$$C \xrightarrow{k^-} A + D \qquad C \xleftarrow{k^+} A + D \qquad E \xrightarrow{k^-} D + A \qquad E \xleftarrow{k^+} D + A$$

$$\begin{aligned}
\frac{dA}{dt} &= k^-(2A_2 + C + E) - 2k^+(A^2 + AD) = \\
&= k^-(A_0 - A) - 2k^+(A^2 + AD) \\
\frac{dD}{dt} &= k^-(D_0 - D) - 2k^+(D^2 + AD) \\
\frac{dC}{dt} &= -k^- C + k^+ AD \\
\frac{dE}{dt} &= -k^- E + k^+ AD \\
\frac{dF}{dt} &= -k^- F + 2k^+ AD
\end{aligned}$$

Now we set $A_0 = D_0$. That entails identical A and D dynamics and $A = D$ is valid for all times. The A- and D-dynamics decouples from the other equations:

$$\frac{dA}{dt} = k^-(A_0 - A) - 4k^+A^2 = k^-A_0 - k^-A - 4k^+A^2$$

This is a Riccaati Differential Equation [235] of the type:

$$\frac{dy}{dt} = h(t) + g(t)y + f(t)y^2$$

The solution is

$$y(t) = \frac{-1}{f(t)z}\frac{dz}{dt} \qquad \text{and } z \text{ obeys}$$

$$\frac{d^2z}{dt^2} - \left(g + \frac{1}{f}\frac{df}{dt}\right)\frac{dz}{dt} + fhz = 0 \quad .$$

With $h = k^-A_0$, $g = -k^-$, $f = -4k^+$, the solution $A(t)$ is determined by

$$A(t) = \frac{1}{4k^+z}\frac{dz}{dt}, \qquad \frac{d^2z}{dt^2} + k^-\frac{dz}{dt} - 4k^-k^+A_0z = 0, \qquad z(0) = 0 \quad .$$

With $z \propto e^{\lambda t}$ we obtain

$$\begin{aligned}
\lambda_{1,2} &= -\frac{k^-}{2} \pm \sqrt{\left(\frac{k^-}{2}\right)^2 + 4k^-k^+A_0} = -\frac{k^-}{2} \pm d \\
z(0) &= 0 \quad \Rightarrow \quad z = e^{\lambda_1 t} - \frac{\lambda_1}{\lambda_2} e^{\lambda_2 t} \\
A(t) &= \frac{\lambda_1\lambda_2\left(e^{\lambda_1 t} - e^{\lambda_2 t}\right)}{4k^+\left(\lambda_2 e^{\lambda_1 t} - \lambda_1 e^{\lambda_2 t}\right)} \quad .
\end{aligned}$$

Now, be $\lambda_1 > 0$ and $t \to \infty$ (stationary state):

$$\begin{aligned}
A(\infty) &= \frac{\lambda_1}{4k^+} = -\frac{k^-}{8k^+} + \sqrt{\left(\frac{k^-}{8k^+}\right)^2 + \frac{k^-}{4k^+}A_0} \\
\text{with } k^- \ll 16k^+A_0 \qquad A(\infty) &\approx \frac{1}{2}\sqrt{\frac{k^-}{k^+}A_0}
\end{aligned}$$

We obtain with the same assumption on the rates that $|\lambda_{1,2}| \gg k^-$ applies.

We solve the differential equation for F now. Since we know the solution for A and D which takes the reactions of A and D with F into account via monomer conservation, the term $k^+AD = k^+A^2$ turns into a known time-dependent inhomogeneity of the equation. We can write down the solution for F with the method of the variation of constants as

$$F(t) = 2k^+e^{-k^-t}\int_0^t e^{k^-t'}\left[\frac{\lambda_1\lambda_2\left(e^{\lambda_1 t'} - e^{\lambda_2 t'}\right)}{4k^+\left(\lambda_2 e^{\lambda_1 t'} - \lambda_1 e^{\lambda_2 t'}\right)}\right]^2 dt' + Be^{-k^-t}$$

The term in square brackets is constant after a short transient $t^s > \lambda_1^{-1}$ and $t^s > \lambda_2^{-1}$, and we obtain an approximate asymptotic solution:

$$\begin{aligned}
F(t > t^s) &= 2k^+e^{-k^-t^s}\int_0^{t^s} e^{k^-t'}\left[\frac{\lambda_1\lambda_2\left(e^{\lambda_1 t'} - e^{\lambda_2 t'}\right)}{4k^+\left(\lambda_2 e^{\lambda_1 t'} - \lambda_1 e^{\lambda_2 t'}\right)}\right]^2 dt' + \\
&+ e^{-k^-t}\int_{t^s}^t e^{k^-t'}A(\infty)^2 dt' + Be^{-k^-t} \approx \\
&\approx \tilde{B}_1 + \tilde{B}_2 e^{-k^-t}
\end{aligned}$$

Applying the initial condition $F(0) = 0$ to the approximate asymptotic solution leads to

$$F(t > t^s) \approx F(\infty)\left(1 - e^{-k^- t}\right) \qquad \text{with } F(\infty) = \frac{1}{2}A_0 \quad .$$

We obtain further $A_2(\infty) = \frac{1}{4}A_0$, and

$$A_0 = 2A_2(\infty) + F(\infty) + A(\infty) \approx A_0\left(1 + \frac{k^-}{4k^+}\right) \quad .$$

In accordance with the approximation $k^- \ll 16k^+A_0$ is monomer conservation fulfilled only up to terms of order $\frac{k^-}{4k^+}$.

C

APPENDIX C - EPR THEORY

Electron Paramagnetic Resonance (EPR) requires an unpaired electron, which was introduced in EHD2 by site-directed spin labeling (SDSL) with a small paramagnetic spin probe. A commonly used nitroxide label was employed, which covalently binds to cysteine residues, resulting in the side chain R1 (Figure 46). Here, I will describe shortly the theoretical background of EPR experiments conducted in this thesis. An excellent source of information were the manuals of the EPR spectrometers from Bruker Biospin and the teaching resources[1] from G. Jeschke, ETH Zürich, Zürich, CH.

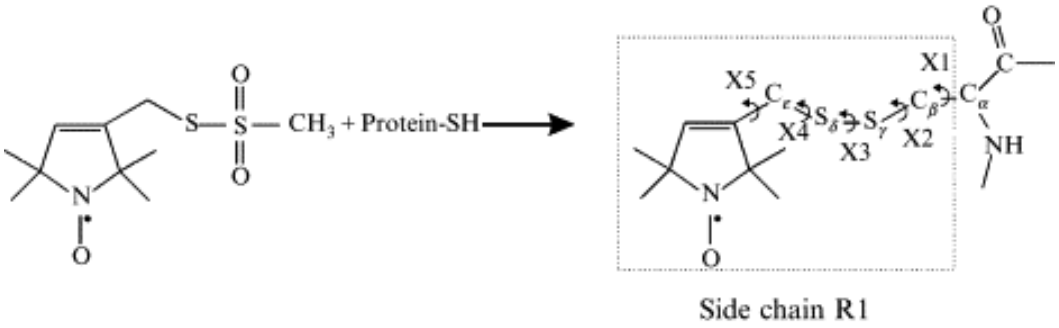

Figure 46: Reaction of the spin label [1-oxy-2,2,5,5-tetramethyl-pyrroline-3-methyl]-methane-thiosulfonate (MTSL) with a sulfhydryl group in a protein results in the side chain R1 (enclosed by a dotted square). Dihedral angles $\chi 1 - \chi 5$ are indicated. Figure and legend adapted from [195].

MOBILITY

Continuous-wave (CW) EPR spectra contain information about the mobility of R1. The unpaired electron has a magnetic moment, which can be oriented with or against the external magnetic field of the spectrometer. Transition between the possible orientations of the magnetic moment occur, when externally applied microwaves meet the resonance condition. Due to the amplitude modulation of the magnetic field, CW spectra are usually recorded as the first derivative of the absorption spectra. The three lines observed in an CW spectrum of R1 arise from three different possible spin states with different spin moments.

Flexible R1 side-chains result in a spectrum with narrowly spaced, sharp lines, whereas buried, immobile R1 side-chains result in broad and distant peaks (Fig-

1 http://www.epr.ethz.ch/education/index

ure 47). Spectra of surface-exposed residues or residues with partial tertiary contacts often reflect intermediate states, between the above mentioned extremes.

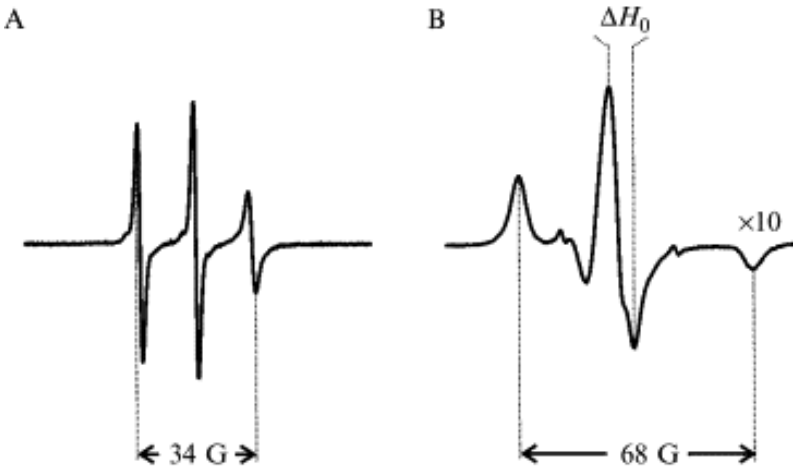

Figure 47: Mobility of R1 determines electron paramagnetic resonance spectral line shape. A test protein is spin-derivatized at a single position. **A** Three sharp peaks indicate high mobility in the GdnHCl denatured state. **B** Broad, highly separated peaks and small amplitudes reflect low mobility of the buried spin label in the native fold ([236]. For a comparison of line shapes, the spectrum in B is amplified 10-fold. The scan width for both spectra is 100 G. Dotted lines mark outer peaks. Separation between outer peaks is indicated for both spectra. The peak-to-peak distance of the central resonance, defined as the central line width (ΔH_0^{-1}), is indicated in B. Figure and legend adapted from [195].

ACCESSIBILITY

CW EPR spectra monitor the transition between different spin states depending on the absorbed microwave power. The energy required for this transition can be altered by the presence of paramagnetic colliders. By recording different spectra in the presence of paramagnetic colliders and simultaneously applying increasing microwave power, important insights into the environment of R1 are obtained. For example, the insertion-depth of R1 into a lipid bilayer can be determined by measuring power saturation in the presence of Ni(II)-ethylenediaminediacetic acid (NiEDDA), a paramagnetic collider partitioning into the aqueous phase, and in the presence of O_2, a paramagnetic collider partitioning into the lipid phase [196].

SPIN-LABEL DISTANCES BY PULSED EPR

Distances between spin probes which are separated between 15 Å and 50 Å, can be detected by double electron electron repulsion (DEER), a pulsed EPR technique.

For an explanation of the detailed physical background of pulsed EPR I direct the reader to a recent review [237].

In brief, a paramagnetic spin label containing an unpaired electron is inserted into a magnetic field, causing the electron spin to precess. Strong, but short microwave pulses are applied by a microwave source operated at two different frequencies. The observer pulse sequence at the observer frequency generates a spin echo. Concomitant with the spin echo a pump pulse at the pump frequency is applied, inverting the orientation of roughly half of the spins. This inversion changes the frequency of the other half of the spins by dipolar coupling, but only if they are separated in space by a permissive distance. The dipolar coupling is reflected in the refocused spin echo at the end of the observer pulse sequence. The distance between the two spin labels can be obtained from a Fourier-Transform of the dipolar spectrum. Another method to calculate the distance by using Tikhonov regularization is explained in [199, 200].

D

APPENDIX D - ABBREVIATIONS

LIST OF ABBREVIATIONS

ADP	adenosine diphosphate
AIM	auto induction medium
ALPS	ArfGAP1-like lipid packing sensor
Amp	ampicillin
AMP-PNP	adenosine-5′-[β,γ-imido]triphosphate
AP2	adapter protein 2
Arf	ADP ribosylation factor
ATP	adenosine triphosphate
BAR	Bin/Amphiphysin/Rvs
BDLP	bacterial dynamin like protein
BESSY	Berliner Elektronenspeicherring für Synchrotronstrahlung
Bin	bridging interactor
BSE	bundle signaling element
Cam	chloramphenicol
Cav	caveolin
CCD	charge-coupled device
CCP	clathrin-coated pit
CCP4	collaborative computational project no. 4
CCV	clathrin-coated vesicle
CD	circular dichroism
CME	clathrin-mediated endocytosis
COP	coat protein complex
C-terminus	carboxy-terminus
CV	column volume
CW	continuous wave
Da	Dalton
DEER	double electron electron resonance
DLP	dynamin like protein
DRP	dynamin related protein
DTT	dithiothreitol
E	extinction
EDTA	ethylenediaminetetraacetic acid
EE	early endosome

EGFP	enhanced green fluorescent protein
EGFR	epidermal growth factor receptor
EH	Eps15-homology
EHBP1	EH domain binding protein 1
EHD	EH domain containing protein
ENTH	epsin N-terminal homology
EPR	electron paramagnetic resonance
Eps15	EGFR pathway substrate 15
ER	endoplasmic reticulum
FCHo	Fer/CIP4 homology only
FMP	Leibniz Forschungsinstitut für Molekulare Medizin
FPLC	fast protein liquid chromatography
FRAP	fluorescent recovery after photobleaching
FRET	förster resonance energy transfer
G domain	guanine nucleotide binding domain
GAP	GTPase activating protein
GBP1	interferon-induced guanylate-binding protein 1
GDP	guanosine diphosphate
GED	guanine effector domain
GEF	guanine exchange factor
GMP-PCP	guanosine-5′-[(β,γ)-methyleno]triphosphate
GMP-PNP	guanosine-5′-[β,γ-imido]triphosphate
GSH	glutathione
GTP	guanosine triphosphate
HEPES	4-(2-hydroxyethyl)-1-piperazineethanesulfonic acid
HPLC	high pressure liquid chromatography
Hsc70	heat shock cognate 70
IMAC	immobilized metal ion affinity chromatography
IPTG	isopropyl β-D-1-thiogalactopyranoside
ITC	isothermal titration calorimetry
Kan	kanamycin
LB	lysogeny broth
LUV	large uni-lamellar vesicle
MD	middle domain
MDC	Max-Delbrück-Centre for Molecular Medicine
MES	2-(*N*-morpholino)ethanesulfonic acid
MLV	multi-lamellar vesicle
MPD	2-Methyl-2,4-pentanediol
MTSL	1-oxy-2,2,5,5-tetramethyl-pyrroline-3-methyl]-methane-thiosulfonate
MW	molecular weight

NiEDDA	Ni(II)-ethylenediaminediacetic acid
NiNTA	nickel-nitrilotriacetic acid
N-terminus	amino-terminus
PACSIN	protein kinase C and casein kinase substrate in neurons protein
PCR	polymerase chain reaction
PDB	protein data bank
PEG	polyethylene glycol
PH	pleckstrin homology
PI(4)P	phosphatidylinositol-4-phosphate
PI(4,5)P_2	phosphatidylinositol-4,5-bisphosphate
PKC	protein kinase C
PMT	photo multiplier tube
PRD	proline-rich domain
PX	PhoX
RALS	right angle light scattering
Ras	rat sarcoma
RI	refractive index
RT	room temperature
Rvs	reduced viability upon starvation
SAD	single anomalous dispersion
Sar	Secretion-associated RAS-related protein 1
SDSL	site-directed spin labeling
SDS-PAGE	sodiumdodecylsulfate polyacrylamide gel electrophoresis
SEC	size exclusion chromatography
SeMet	selenomethionine
SH3	Src homology 3
SLS	swiss light source
Snx9	sorting nexin 9
SUV	small uni-lamellar vesicle
TIRF	total internal reflection fluorescence
TLS	translation, liberation and screw-rotation displacement
UV	ultraviolet

AMINO ACID ABBREVIATIONS

For amino acids, the one and three letter code was used: A, Ala: alanine; C, Cys: cysteine; D, Asp: aspartate; E, Glu: glutamate; F, Phe: phenylalanine; G, Gly: glycine; H, His: histidine; I, Ile: isoleucine; K, Lys: lysine; L, Leu: leucine; M, Met: methionine; N, Asn: asparagine; P, Pro: proline; Q, Gln: glutamine; R, Arg: arginine; S, Ser: serine; T, Thr: threonine; V, Val: valine; W, Trp: tryptophane; Y, Tyr: tyrosine; x: any amino acid.

BIBLIOGRAPHY

[1] Doherty, G.J. & McMahon, H.T. Mechanisms of endocytosis. *Annu Rev Biochem*, 2009

[2] Lin, R.C. & Scheller, R.H. Mechanisms of synaptic vesicle exocytosis. *Annu Rev Cell Dev Biol*, 16:19–49, 2000

[3] McMahon, H.T. & Boucrot, E. Molecular mechanism and physiological functions of clathrin-mediated endocytosis. *Nat Rev Mol Cell Biol*, 12(8):517–533, 2011

[4] Henne, W.M., Boucrot, E., Meinecke, M., Evergren, E., Vallis, Y., Mittal, R. & McMahon, H.T. Fcho proteins are nucleators of clathrin-mediated endocytosis. *Science*, 328(5983):1281–1284, 2010

[5] Stimpson, H.E.M., Toret, C.P., Cheng, A.T., Pauly, B.S. & Drubin, D.G. Early-arriving syp1p and ede1p function in endocytic site placement and formation in budding yeast. *Mol Biol Cell*, 20(22):4640–4651, 2009

[6] Collins, B.M., McCoy, A.J., Kent, H.M., Evans, P.R. & Owen, D.J. Molecular architecture and functional model of the endocytic ap2 complex. *Cell*, 109(4):523–535, 2002

[7] Ford, M.G.J., Mills, I.G., Peter, B.J., Vallis, Y., Praefcke, G.J.K., Evans, P.R. & McMahon, H.T. Curvature of clathrin-coated pits driven by epsin. *Nature*, 419(6905):361–366, 2002

[8] Pearse, B.M. Clathrin: a unique protein associated with intracellular transfer of membrane by coated vesicles. *Proc Natl Acad Sci U S A*, 73(4):1255–1259, 1976

[9] ter Haar, E., Musacchio, A., Harrison, S.C. & Kirchhausen, T. Atomic structure of clathrin: a beta propeller terminal domain joins an alpha zigzag linker. *Cell*, 95(4):563–573, 1998

[10] Wigge, P., Köhler, K., Vallis, Y., Doyle, C.A., Owen, D., Hunt, S.P. & McMahon, H.T. Amphiphysin heterodimers: potential role in clathrin-mediated endocytosis. *Mol Biol Cell*, 8(10):2003–2015, 1997

[11] Ferguson, S.M., Ferguson, S., Raimondi, A., Paradise, S., Shen, H., Mesaki, K., Ferguson, A., Destaing, O., Ko, G., Takasaki, J., Cremona, O., Toole, E.O. & Camilli, P.D. Coordinated actions of actin and bar proteins upstream of dynamin at endocytic clathrin-coated pits. *Dev Cell*, 17(6):811–822, 2009

[12] Youn, J.Y., Friesen, H., Kishimoto, T., Henne, W.M., Kurat, C.F., Ye, W., Ceccarelli, D.F., Sicheri, F., Kohlwein, S.D., McMahon, H.T. & Andrews, B.J. Dissecting bar domain function in the yeast amphiphysins rvs161 and rvs167 during endocytosis. *Mol Biol Cell*, 21(17):3054–3069, 2010

[13] Sundborger, A., Soderblom, C., Vorontsova, O., Evergren, E., Hinshaw, J.E. & Shupliakov, O. An endophilin-dynamin complex promotes budding of clathrin-coated vesicles during synaptic vesicle recycling. *J Cell Sci*, 124(Pt 1):133–143, 2011

[14] Praefcke, G.J.K. & McMahon, H.T. The dynamin superfamily: universal membrane tubulation and fission molecules? *Nat Rev Mol Cell Biol*, 5(2):133–147, 2004

[15] Cheng, Y., Boll, W., Kirchhausen, T., Harrison, S.C. & Walz, T. Cryo-electron tomography of clathrin-coated vesicles: structural implications for coat assembly. *J Mol Biol*, 365(3):892–899, 2007

[16] Bretscher, M.S., Thomson, J.N. & Pearse, B.M. Coated pits act as molecular filters. *Proc Natl Acad Sci U S A*, 77(7):4156–4159, 1980

[17] Ungewickell, E., Ungewickell, H., Holstein, S.E., Lindner, R., Prasad, K., Barouch, W., Martin, B., Greene, L.E. & Eisenberg, E. Role of auxilin in uncoating clathrin-coated vesicles. *Nature*, 378(6557):632–635, 1995

[18] Schlossman, D.M., Schmid, S.L., Braell, W.A. & Rothman, J.E. An enzyme that removes clathrin coats: purification of an uncoating atpase. *J Cell Biol*, 99(2):723–733, 1984

[19] Guo, S., Stolz, L.E., Lemrow, S.M. & York, J.D. Sac1-like domains of yeast sac1, inp52, and inp53 and of human synaptojanin encode polyphosphoinositide phosphatases. *J Biol Chem*, 274(19):12990–12995, 1999

[20] Haffner, C., Takei, K., Chen, H., Ringstad, N., Hudson, A., Butler, M.H., Salcini, A.E., Fiore, P.P.D. & Camilli, P.D. Synaptojanin 1: localization on coated endocytic intermediates in nerve terminals and interaction of its 170 kda isoform with eps15. *FEBS Lett*, 419(2-3):175–180, 1997

[21] Haffner, C., Paolo, G.D., Rosenthal, J.A. & de Camilli, P. Direct interaction of the 170 kda isoform of synaptojanin 1 with clathrin and with the clathrin adaptor ap-2. *Curr Biol*, 10(8):471–474, 2000

[22] Cocucci, E., Aguet, F., Boulant, S. & Kirchhausen, T. The first five seconds in the life of a clathrin-coated pit. *Cell*, 150(3):495–507, 2012

[23] Kukulski, W., Schorb, M., Kaksonen, M. & Briggs, J.A.G. Plasma membrane reshaping during endocytosis is revealed by time-resolved electron tomography. *Cell*, 150(3):508–520, 2012

[24] Howes, M.T., Kirkham, M., Riches, J., Cortese, K., Walser, P.J., Simpson, F., Hill, M.M., Jones, A., Lundmark, R., Lindsay, M.R., Hernandez-Deviez, D.J., Hadzic, G., McCluskey, A., Bashir, R., Liu, L., Pilch, P., McMahon, H., Robinson, P.J., Hancock, J.F., Mayor, S. & Parton, R.G. Clathrin-independent carriers form a high capacity endocytic sorting system at the leading edge of migrating cells. *J Cell Biol*, 190(4):675–691, 2010

[25] Sandvig, K., Pust, S., Skotland, T. & van Deurs, B. Clathrin-independent endocytosis: mechanisms and function. *Curr Opin Cell Biol*, 2011

[26] Rothberg, K.G., Heuser, J.E., Donzell, W.C., Ying, Y.S., Glenney, J.R. & Anderson, R.G. Caveolin, a protein component of caveolae membrane coats. *Cell*, 68(4):673–682, 1992

[27] Kurzchalia, T.V., Dupree, P., Parton, R.G., Kellner, R., Virta, H., Lehnert, M. & Simons, K. Vip21, a 21-kd membrane protein is an integral component of trans-golgi-network-derived transport vesicles. *J Cell Biol*, 118(5):1003–1014, 1992

[28] Richter, T., Floetenmeyer, M., Ferguson, C., Galea, J., Goh, J., Lindsay, M.R., Morgan, G.P., Marsh, B.J. & Parton, R.G. High-resolution 3d quantitative analysis of caveolar ultrastructure and caveola-cytoskeleton interactions. *Traffic*, 9(6):893–909, 2008

[29] Schlörmann, W., Steiniger, F., Richter, W., Kaufmann, R., Hause, G., Lemke, C. & Westermann, M. The shape of caveolae is omega-like after glutaraldehyde fixation and cup-like after cryofixation. *Histochem Cell Biol*, 133(2):223–228, 2010

[30] Walser, P.J., Ariotti, N., Howes, M., Ferguson, C., Webb, R., Schwudke, D., Leneva, N., Cho, K.J., Cooper, L., Rae, J., Floetenmeyer, M., Oorschot, V.M.J., Skoglund, U., Simons, K., Hancock, J.F. & Parton, R.G. Constitutive formation of caveolae in a bacterium. *Cell*, 150(4):752–763, 2012

[31] Thomsen, P., Roepstorff, K., Stahlhut, M. & van Deurs, B. Caveolae are highly immobile plasma membrane microdomains, which are not involved in constitutive endocytic trafficking. *Mol Biol Cell*, 13(1):238–250, 2002

[32] Pelkmans, L. & Zerial, M. Kinase-regulated quantal assemblies and kiss-and-run recycling of caveolae. *Nature*, 436(7047):128–133, 2005

[33] Lay, S.L. & Kurzchalia, T.V. Getting rid of caveolins: phenotypes of caveolin-deficient animals. *Biochim Biophys Acta*, 1746(3):322–333, 2005

[34] Parton, R.G. & Simons, K. The multiple faces of caveolae. *Nat Rev Mol Cell Biol*, 8(3):185–194, 2007

[35] Monier, S., Dietzen, D.J., Hastings, W.R., Lublin, D.M. & Kurzchalia, T.V. Oligomerization of vip21-caveolin in vitro is stabilized by long chain fatty acylation or cholesterol. *FEBS Lett*, 388(2-3):143–149, 1996

[36] Pol, A., Martin, S., Fernández, M.A., Ingelmo-Torres, M., Ferguson, C., Enrich, C. & Parton, R.G. Cholesterol and fatty acids regulate dynamic caveolin trafficking through the golgi complex and between the cell surface and lipid bodies. *Mol Biol Cell*, 16(4):2091–2105, 2005

[37] Monier, S., Parton, R.G., Vogel, F., Behlke, J., Henske, A. & Kurzchalia, T.V. Vip21-caveolin, a membrane protein constituent of the caveolar coat, oligomerizes in vivo and in vitro. *Mol Biol Cell*, 6(7):911–927, 1995

[38] Hayer, A., Stoeber, M., Ritz, D., Engel, S., Meyer, H.H. & Helenius, A. Caveolin-1 is ubiquitinated and targeted to intralumenal vesicles in endolysosomes for degradation. *J Cell Biol*, 191(3):615–629, 2010

[39] Dietzen, D.J., Hastings, W.R. & Lublin, D.M. Caveolin is palmitoylated on multiple cysteine residues. palmitoylation is not necessary for localization of caveolin to caveolae. *J Biol Chem*, 270(12):6838–6842, 1995

[40] Parat, M.O. & Fox, P.L. Palmitoylation of caveolin-1 in endothelial cells is post-translational but irreversible. *J Biol Chem*, 276(19):15776–15782, 2001

[41] Bastiani, M. & Parton, R.G. Caveolae at a glance. *J Cell Sci*, 123(Pt 22):3831–3836, 2010

[42] Head, B.P., Patel, H.H., Roth, D.M., Murray, F., Swaney, J.S., Niesman, I.R., Farquhar, M.G. & Insel, P.A. Microtubules and actin microfilaments regulate lipid raft/caveolae localization of adenylyl cyclase signaling components. *J Biol Chem*, 281(36):26391–26399, 2006

[43] Stahlhut, M. & van Deurs, B. Identification of filamin as a novel ligand for caveolin-1: evidence for the organization of caveolin-1-associated membrane domains by the actin cytoskeleton. *Mol Biol Cell*, 11(1):325–337, 2000

[44] Fra, A.M., Williamson, E., Simons, K. & Parton, R.G. De novo formation of caveolae in lymphocytes by expression of vip21-caveolin. *Proc Natl Acad Sci U S A*, 92(19):8655–8659, 1995

[45] Lipardi, C., Mora, R., Colomer, V., Paladino, S., Nitsch, L., Rodriguez-Boulan, E. & Zurzolo, C. Caveolin transfection results in caveolae formation but not apical sorting of glycosylphosphatidylinositol (gpi)-anchored proteins in epithelial cells. *J Cell Biol*, 140(3):617–626, 1998

[46] Hagiwara, Y., Sasaoka, T., Araishi, K., Imamura, M., Yorifuji, H., Nonaka, I., Ozawa, E. & Kikuchi, T. Caveolin-3 deficiency causes muscle degeneration in mice. *Hum Mol Genet*, 9(20):3047–3054, 2000

[47] Galbiati, F., Razani, B. & Lisanti, M.P. Caveolae and caveolin-3 in muscular dystrophy. *Trends Mol Med*, 7(10):435–441, 2001

[48] Drab, M., Verkade, P., Elger, M., Kasper, M., Lohn, M., Lauterbach, B., Menne, J., Lindschau, C., Mende, F., Luft, F.C., Schedl, A., Haller, H. & Kurzchalia, T.V. Loss of caveolae, vascular dysfunction, and pulmonary defects in caveolin-1 gene-disrupted mice. *Science*, 293(5539):2449–2452, 2001

[49] Razani, B., Engelman, J.A., Wang, X.B., Schubert, W., Zhang, X.L., Marks, C.B., Macaluso, F., Russell, R.G., Li, M., Pestell, R.G., Vizio, D.D., Hou, H., Kneitz, B., Lagaud, G., Christ, G.J., Edelmann, W. & Lisanti, M.P. Caveolin-1 null mice are viable but show evidence of hyperproliferative and vascular abnormalities. *J Biol Chem*, 276(41):38121–38138, 2001

[50] Razani, B., Wang, X.B., Engelman, J.A., Battista, M., Lagaud, G., Zhang, X.L., Kneitz, B., Hou, H., Christ, G.J., Edelmann, W. & Lisanti, M.P. Caveolin-2-deficient mice show evidence of severe pulmonary dysfunction without disruption of caveolae. *Mol Cell Biol*, 22(7):2329–2344, 2002

[51] Park, D.S., Woodman, S.E., Schubert, W., Cohen, A.W., Frank, P.G., Chandra, M., Shirani, J., Razani, B., Tang, B., Jelicks, L.A., Factor, S.M., Weiss, L.M., Tanowitz, H.B. & Lisanti, M.P. Caveolin-1/3 double-knockout mice

are viable, but lack both muscle and non-muscle caveolae, and develop a severe cardiomyopathic phenotype. *Am J Pathol*, 160(6):2207–2217, 2002

[52] Aboulaich, N., Vainonen, J.P., Strålfors, P. & Vener, A.V. Vectorial proteomics reveal targeting, phosphorylation and specific fragmentation of polymerase i and transcript release factor (ptrf) at the surface of caveolae in human adipocytes. *Biochem J*, 383(Pt 2):237–248, 2004

[53] Hill, M.M., Bastiani, M., Luetterforst, R., Kirkham, M., Kirkham, A., Nixon, S.J., Walser, P., Abankwa, D., Oorschot, V.M.J., Martin, S., Hancock, J.F. & Parton, R.G. Ptrf-cavin, a conserved cytoplasmic protein required for caveola formation and function. *Cell*, 132(1):113–124, 2008

[54] Hansen, C.G., Bright, N.A., Howard, G. & Nichols, B.J. Sdpr induces membrane curvature and functions in the formation of caveolae. *Nat Cell Biol*, 11(7):807–814, 2009

[55] McMahon, K.A., Zajicek, H., Li, W.P., Peyton, M.J., Minna, J.D., Hernandez, V.J., Luby-Phelps, K. & Andersonah, R.G.W. Srbc/cavin-3 is a caveolin adapter protein that regulates caveolae function. *EMBO J*, 28(8):1001–1015, 2009

[56] Bastiani, M., Liu, L., Hill, M.M., Jedrychowski, M.P., Nixon, S.J., Lo, H.P., Abankwa, D., Luetterforst, R., Fernandez-Rojo, M., Breen, M.R., Gygi, S.P., Vinten, J., Walser, P.J., North, K.N., Hancock, J.F., Pilch, P.F. & Parton, R.G. Murc/cavin-4 and cavin family members form tissue-specific caveolar complexes. *J Cell Biol*, 185(7):1259–1273, 2009

[57] Hansen, C.G. & Nichols, B.J. Exploring the caves: cavins, caveolins and caveolae. *Trends Cell Biol*, 20(4):177–186, 2010

[58] Liu, L., Brown, D., McKee, M., Lebrasseur, N.K., Yang, D., Albrecht, K.H., Ravid, K. & Pilch, P.F. Deletion of cavin/ptrf causes global loss of caveolae, dyslipidemia, and glucose intolerance. *Cell Metab*, 8(4):310–317, 2008

[59] Liu, L. & Pilch, P.F. A critical role of cavin (polymerase i and transcript release factor) in caveolae formation and organization. *J Biol Chem*, 283(7):4314–4322, 2008

[60] Gustincich, S., Vatta, P., Goruppi, S., Wolf, M., Saccone, S., Valle, G.D., Baggiolini, M. & Schneider, C. The human serum deprivation response gene (sdpr) maps to 2q32-q33 and codes for a phosphatidylserine-binding protein. *Genomics*, 57(1):120–129, 1999

[61] Izumi, Y., Hirai, S., Tamai, Y., Fujise-Matsuoka, A., Nishimura, Y. & Ohno, S. A protein kinase cdelta-binding protein srbc whose expression is induced by serum starvation. *J Biol Chem*, 272(11):7381–7389, 1997

[62] Ogata, T., Ueyama, T., Isodono, K., Tagawa, M., Takehara, N., Kawashima, T., Harada, K., Takahashi, T., Shioi, T., Matsubara, H. & Oh, H. Murc, a muscle-restricted coiled-coil protein that modulates the rho/rock pathway, induces cardiac dysfunction and conduction disturbance. *Mol Cell Biol*, 28(10):3424–3436, 2008

[63] Tagawa, M., Ueyama, T., Ogata, T., Takehara, N., Nakajima, N., Isodono, K., Asada, S., Takahashi, T., Matsubara, H. & Oh, H. Murc, a muscle-restricted coiled-coil protein, is involved in the regulation of skeletal myogenesis. *Am J Physiol Cell Physiol*, 295(2):C490–C498, 2008

[64] Dulhunty, A.F. & Franzini-Armstrong, C. The relative contributions of the folds and caveolae to the surface membrane of frog skeletal muscle fibres at different sarcomere lengths. *J Physiol*, 250(3):513–539, 1975

[65] Prescott, L. & Brightman, M.W. The sarcolemma of aplysia smooth muscle in freeze-fracture preparations. *Tissue Cell*, 8(2):241–258, 1976

[66] Boyd, N.L., Park, H., Yi, H., Boo, Y.C., Sorescu, G.P., Sykes, M. & Jo, H. Chronic shear induces caveolae formation and alters erk and akt responses in endothelial cells. *Am J Physiol Heart Circ Physiol*, 285(3):H1113–H1122, 2003

[67] Park, H., Go, Y.M., Darji, R., Choi, J.W., Lisanti, M.P., Maland, M.C. & Jo, H. Caveolin-1 regulates shear stress-dependent activation of extracellular signal-regulated kinase. *Am J Physiol Heart Circ Physiol*, 278(4):H1285–H1293, 2000

[68] Rizzo, V., Morton, C., DePaola, N., Schnitzer, J.E. & Davies, P.F. Recruitment of endothelial caveolae into mechanotransduction pathways by flow conditioning in vitro. *Am J Physiol Heart Circ Physiol*, 285(4):H1720–H1729, 2003

[69] Sedding, D.G., Hermsen, J., Seay, U., Eickelberg, O., Kummer, W., Schwencke, C., Strasser, R.H., Tillmanns, H. & Braun-Dullaeus, R.C. Caveolin-1 facilitates mechanosensitive protein kinase b (akt) signaling in vitro and in vivo. *Circ Res*, 96(6):635–642, 2005

[70] Kawamura, S., Miyamoto, S. & Brown, J.H. Initiation and transduction of stretch-induced rhoa and rac1 activation through caveolae: cytoskeletal regulation of erk translocation. *J Biol Chem*, 278(33):31111–31117, 2003

[71] Kozera, L., White, E. & Calaghan, S. Caveolae act as membrane reserves which limit mechanosensitive i(cl,swell) channel activation during swelling in the rat ventricular myocyte. *PLoS One*, 4(12):e8312, 2009

[72] Sinha, B., Köster, D., Ruez, R., Gonnord, P., Bastiani, M., Abankwa, D., Stan, R.V., Butler-Browne, G., Vedie, B., Johannes, L., Morone, N., Parton, R.G., Raposo, G., Sens, P., Lamaze, C. & Nassoy, P. Cells respond to mechanical stress by rapid disassembly of caveolae. *Cell*, 144(3):402–413, 2011

[73] Shibata, Y., Hu, J., Kozlov, M.M. & Rapoport, T.A. Mechanisms shaping the membranes of cellular organelles. *Annu Rev Cell Dev Biol*, 25:329–354, 2009

[74] McMahon, H.T. & Gallop, J.L. Membrane curvature and mechanisms of dynamic cell membrane remodelling. *Nature*, 438(7068):590–596, 2005

[75] Kooijman, E.E., Chupin, V., Fuller, N.L., Kozlov, M.M., de Kruijff, B., Burger, K.N.J. & Rand, P.R. Spontaneous curvature of phosphatidic acid and lysophosphatidic acid. *Biochemistry*, 44(6):2097–2102, 2005

[76] Mackinnon, R. Structural biology. voltage sensor meets lipid membrane. *Science*, 306(5700):1304–1305, 2004

[77] Rodriguez-Boulan, E., Kreitzer, G. & Müsch, A. Organization of vesicular trafficking in epithelia. *Nat Rev Mol Cell Biol*, 6(3):233–247, 2005

[78] Kessels, M.M. & Qualmann, B. The syndapin protein family: linking membrane trafficking with the cytoskeleton. *J Cell Sci*, 117(Pt 15):3077–3086, 2004

[79] Kinuta, M., Yamada, H., Abe, T., Watanabe, M., Li, S.A., Kamitani, A., Yasuda, T., Matsukawa, T., Kumon, H. & Takei, K. Phosphatidylinositol 4,5-bisphosphate stimulates vesicle formation from liposomes by brain cytosol. *Proc Natl Acad Sci U S A*, 99(5):2842–2847, 2002

[80] Campelo, F., McMahon, H.T. & Kozlov, M.M. The hydrophobic insertion mechanism of membrane curvature generation by proteins. *Biophys J*, 95(5):2325–2339, 2008

[81] Liu, Y., Kahn, R.A. & Prestegard, J.H. Structure and membrane interaction of myristoylated arf1. *Structure*, 17(1):79–87, 2009

[82] Shiba, T., Kawasaki, M., Takatsu, H., Nogi, T., Matsugaki, N., Igarashi, N., Suzuki, M., Kato, R., Nakayama, K. & Wakatsuki, S. Molecular mechanism of membrane recruitment of gga by arf in lysosomal protein transport. *Nat Struct Biol*, 10(5):386–393, 2003

[83] Beck, R., Sun, Z., Adolf, F., Rutz, C., Bassler, J., Wild, K., Sinning, I., Hurt, E., Brügger, B., Béthune, J. & Wieland, F. Membrane curvature induced by arf1-gtp is essential for vesicle formation. *Proc Natl Acad Sci U S A*, 105(33):11731–11736, 2008

[84] Krauss, M., Jia, J.Y., Roux, A., Beck, R., Wieland, F.T., Camilli, P.D. & Haucke, V. Arf1-gtp-induced tubule formation suggests a function of arf family proteins in curvature acquisition at sites of vesicle budding. *J Biol Chem*, 283(41):27717–27723, 2008

[85] Bi, X., Corpina, R.A. & Goldberg, J. Structure of the sec23/24-sar1 prebudding complex of the copii vesicle coat. *Nature*, 419(6904):271–277, 2002

[86] Lee, M.C.S., Orci, L., Hamamoto, S., Futai, E., Ravazzola, M. & Schekman, R. Sar1p n-terminal helix initiates membrane curvature and completes the fission of a copii vesicle. *Cell*, 122(4):605–617, 2005

[87] Lundmark, R., Doherty, G.J., Vallis, Y., Peter, B.J. & McMahon, H.T. Arf family gtp loading is activated by, and generates, positive membrane curvature. *Biochem J*, 414(2):189–194, 2008

[88] Barlowe, C. & Schekman, R. Sec12 encodes a guanine-nucleotide-exchange factor essential for transport vesicle budding from the er. *Nature*, 365(6444):347–349, 1993

[89] Yoshihisa, T., Barlowe, C. & Schekman, R. Requirement for a gtpase-activating protein in vesicle budding from the endoplasmic reticulum. *Science*, 259(5100):1466–1468, 1993

[90] Gillingham, A.K. & Munro, S. The small g proteins of the arf family and their regulators. *Annu Rev Cell Dev Biol*, 23:579–611, 2007

[91] Bigay, J., Gounon, P., Robineau, S. & Antonny, B. Lipid packing sensed by arfgap1 couples copi coat disassembly to membrane bilayer curvature. *Nature*, 426(6966):563–566, 2003

[92] Pucadyil, T.J. & Schmid, S.L. Conserved functions of membrane active gtpases in coated vesicle formation. *Science*, 325(5945):1217–1220, 2009

[93] Kirchhausen, T. Clathrin. *Annu Rev Biochem*, 69:699–727, 2000

[94] McMahon, H.T. & Mills, I.G. Cop and clathrin-coated vesicle budding: different pathways, common approaches. *Curr Opin Cell Biol*, 16(4):379–391, 2004

[95] Stagg, S.M., LaPointe, P. & Balch, W.E. Structural design of cage and coat scaffolds that direct membrane traffic. *Curr Opin Struct Biol*, 17(2):221–228, 2007

[96] Boucrot, E., Pick, A., Camdere, G., Liska, N., Evergren, E., McMahon, H.T. & Kozlov, M.M. Membrane fission is promoted by insertion of amphipathic helices and is restricted by crescent bar domains. *Cell*, 149(1):124–136, 2012

[97] Takei, K., Slepnev, V.I., Haucke, V. & Camilli, P.D. Functional partnership between amphiphysin and dynamin in clathrin-mediated endocytosis. *Nat Cell Biol*, 1(1):33–39, 1999

[98] Farsad, K., Ringstad, N., Takei, K., Floyd, S.R., Rose, K. & Camilli, P.D. Generation of high curvature membranes mediated by direct endophilin bilayer interactions. *J Cell Biol*, 155(2):193–200, 2001

[99] Peter, B.J., Kent, H.M., Mills, I.G., Vallis, Y., Butler, P.J.G., Evans, P.R. & McMahon, H.T. Bar domains as sensors of membrane curvature: the amphiphysin bar structure. *Science*, 303(5657):495–499, 2004

[100] Tarricone, C., Xiao, B., Justin, N., Walker, P.A., Rittinger, K., Gamblin, S.J. & Smerdon, S.J. The structural basis of arfaptin-mediated cross-talk between rac and arf signalling pathways. *Nature*, 411(6834):215–219, 2001

[101] Henne, W.M., Kent, H.M., Ford, M.G.J., Hegde, B.G., Daumke, O., Butler, P.J.G., Mittal, R., Langen, R., Evans, P.R. & McMahon, H.T. Structure and analysis of fcho2 f-bar domain: a dimerizing and membrane recruitment module that effects membrane curvature. *Structure*, 15(7):839–852, 2007

[102] Shimada, A., Niwa, H., Tsujita, K., Suetsugu, S., Nitta, K., Hanawa-Suetsugu, K., Akasaka, R., Nishino, Y., Toyama, M., Chen, L., Liu, Z.J., Wang, B.C., Yamamoto, M., Terada, T., Miyazawa, A., Tanaka, A., Sugano, S., Shirouzu, M., Nagayama, K., Takenawa, T. & Yokoyama, S. Curved efc/f-bar-domain dimers are joined end to end into a filament for membrane invagination in endocytosis. *Cell*, 129(4):761–772, 2007

[103] Frost, A., Camilli, P.D. & Unger, V.M. F-bar proteins join the bar family fold. *Structure*, 15(7):751–753, 2007

[104] Frost, A., Unger, V.M. & Camilli, P.D. The bar domain superfamily: membrane-molding macromolecules. *Cell*, 137(2):191–196, 2009

[105] Rao, Y. & Haucke, V. Membrane shaping by the bin/amphiphysin/rvs (bar) domain protein superfamily. *Cell Mol Life Sci*, 2011

[106] Gallop, J.L., Jao, C.C., Kent, H.M., Butler, P.J.G., Evans, P.R., Langen, R. & McMahon, H.T. Mechanism of endophilin n-bar domain-mediated membrane curvature. *EMBO J*, 25(12):2898–2910, 2006

[107] Jao, C.C., Hegde, B.G., Gallop, J.L., Hegde, P.B., McMahon, H.T., Haworth, I.S. & Langen, R. Roles of amphipathic helices and the bin/amphiphysin/rvs (bar) domain of endophilin in membrane curvature generation. *J Biol Chem*, 285(26):20164–20170, 2010

[108] Mim, C., Cui, H., Gawronski-Salerno, J.A., Frost, A., Lyman, E., Voth, G.A. & Unger, V.M. Structural basis of membrane bending by the n-bar protein endophilin. *Cell*, 149(1):137–145, 2012

[109] Wang, Q., Navarro, M.V.A.S., Peng, G., Molinelli, E., Goh, S.L., Judson, B.L., Rajashankar, K.R. & Sondermann, H. Molecular mechanism of membrane constriction and tubulation mediated by the f-bar protein pacsin/syndapin. *Proc Natl Acad Sci U S A*, 106(31):12700–12705, 2009

[110] Rao, Y., Ma, Q., Vahedi-Faridi, A., Sundborger, A., Pechstein, A., Puchkov, D., Luo, L., Shupliakov, O., Saenger, W. & Haucke, V. Molecular basis for sh3 domain regulation of f-bar-mediated membrane deformation. *Proc Natl Acad Sci U S A*, 107(18):8213–8218, 2010

[111] Senju, Y., Itoh, Y., Takano, K., Hamada, S. & Suetsugu, S. Essential role of pacsin2/syndapin-ii in caveolae membrane sculpting. *J Cell Sci*, 2011

[112] Quan, A., Xue, J., Wielens, J., Smillie, K.J., Anggono, V., Parker, M.W., Cousin, M.A., Graham, M.E. & Robinson, P.J. Phosphorylation of syndapin i f-bar domain at two helix-capping motifs regulates membrane tubulation. *Proc Natl Acad Sci U S A*, 2012

[113] Bai, X., Meng, G., Luo, M. & Zheng, X. The rigidity of the wedge loop in pacsin 3 is a key factor in dictating the diameters of tubules. *J Biol Chem*, 2012

[114] Ridley, A.J. Rho gtpases and actin dynamics in membrane protrusions and vesicle trafficking. *Trends Cell Biol*, 16(10):522–529, 2006

[115] de Kreuk, B.J., Nethe, M., Fernandez-Borja, M., Anthony, E.C., Hensbergen, P.J., Deelder, A.M., Plomann, M. & Hordijk, P.L. The f-bar domain protein pacsin2 associates with rac1 and regulates cell spreading and migration. *J Cell Sci*, 124(Pt 14):2375–2388, 2011

[116] Cao, H., Garcia, F. & McNiven, M.A. Differential distribution of dynamin isoforms in mammalian cells. *Mol Biol Cell*, 9(9):2595–2609, 1998

[117] Heymann, J.A.W. & Hinshaw, J.E. Dynamins at a glance. *J Cell Sci*, 122(Pt 19):3427–3431, 2009

[118] Ramachandran, R. Vesicle scission: dynamin. *Semin Cell Dev Biol*, 22(1):10–17, 2011

[119] Schmid, S.L. & Frolov, V.A. Dynamin: Functional design of a membrane fission catalyst. *Annu Rev Cell Dev Biol*, 2011

[120] Campelo, F. & Malhotra, V. Membrane fission: the biogenesis of transport carriers. *Annu Rev Biochem*, 81:407–427, 2012

[121] Paschal, B.M., Shpetner, H.S. & Vallee, R.B. Map 1c is a microtubule-activated atpase which translocates microtubules in vitro and has dynein-like properties. *J Cell Biol*, 105(3):1273–1282, 1987

[122] Shpetner, H.S. & Vallee, R.B. Identification of dynamin, a novel mechanochemical enzyme that mediates interactions between microtubules. *Cell*, 59(3):421–432, 1989

[123] Koenig, J.H. & Ikeda, K. Disappearance and reformation of synaptic vesicle membrane upon transmitter release observed under reversible blockage of membrane retrieval. *J Neurosci*, 9(11):3844–3860, 1989

[124] van der Bliek, A.M. & Meyerowitz, E.M. Dynamin-like protein encoded by the drosophila shibire gene associated with vesicular traffic. *Nature*, 351(6325):411–414, 1991

[125] Chen, M.S., Obar, R.A., Schroeder, C.C., Austin, T.W., Poodry, C.A., Wadsworth, S.C. & Vallee, R.B. Multiple forms of dynamin are encoded by shibire, a drosophila gene involved in endocytosis. *Nature*, 351(6327):583–586, 1991

[126] Hinshaw, J.E. & Schmid, S.L. Dynamin self-assembles into rings suggesting a mechanism for coated vesicle budding. *Nature*, 374(6518):190–192, 1995

[127] Carr, J.F. & Hinshaw, J.E. Dynamin assembles into spirals under physiological salt conditions upon the addition of gdp and gamma-phosphate analogues. *J Biol Chem*, 272(44):28030–28035, 1997

[128] Sweitzer, S.M. & Hinshaw, J.E. Dynamin undergoes a gtp-dependent conformational change causing vesiculation. *Cell*, 93(6):1021–1029, 1998

[129] Takei, K., McPherson, P.S., Schmid, S.L. & Camilli, P.D. Tubular membrane invaginations coated by dynamin rings are induced by gtp-gamma s in nerve terminals. *Nature*, 374(6518):186–190, 1995

[130] Faelber, K., Posor, Y., Gao, S., Held, M., Roske, Y., Schulze, D., Haucke, V., Noé, F. & Daumke, O. Crystal structure of nucleotide-free dynamin. *Nature*, 477(7366):556–560, 2011

[131] Ford, M.G.J., Jenni, S. & Nunnari, J. The crystal structure of dynamin. *Nature*, 477(7366):561–566, 2011

[132] Gao, S., von der Malsburg, A., Paeschke, S., Behlke, J., Haller, O., Kochs, G. & Daumke, O. Structural basis of oligomerization in the stalk region of dynamin-like mxa. *Nature*, 465(7297):502–506, 2010

[133] Gao, S., von der Malsburg, A., Dick, A., Faelber, K., Schröder, G.F., Haller, O., Kochs, G. & Daumke, O. Structure of myxovirus resistance protein a reveals intra- and intermolecular domain interactions required for the antiviral function. *Immunity*, 2011

[134] Mears, J.A., Ray, P. & Hinshaw, J.E. A corkscrew model for dynamin constriction. *Structure*, 15(10):1190–1202, 2007

[135] Chappie, J.S., Acharya, S., Leonard, M., Schmid, S.L. & Dyda, F. G domain dimerization controls dynamin's assembly-stimulated gtpase activity. *Nature*, 465(7297):435–440, 2010

[136] Stowell, M.H., Marks, B., Wigge, P. & McMahon, H.T. Nucleotide-dependent conformational changes in dynamin: evidence for a mechanochemical molecular spring. *Nat Cell Biol*, 1(1):27–32, 1999

[137] Roux, A., Uyhazi, K., Frost, A. & Camilli, P.D. Gtp-dependent twisting of dynamin implicates constriction and tension in membrane fission. *Nature*, 441(7092):528–531, 2006

[138] Bashkirov, P.V., Akimov, S.A., Evseev, A.I., Schmid, S.L., Zimmerberg, J. & Frolov, V.A. Gtpase cycle of dynamin is coupled to membrane squeeze and release, leading to spontaneous fission. *Cell*, 135(7):1276–1286, 2008. 090218 literature seminar

[139] Pucadyil, T.J. & Schmid, S.L. Real-time visualization of dynamin-catalyzed membrane fission and vesicle release. *Cell*, 135(7):1263–1275, 2008. 090218 literature seminar

[140] Mintz, L., Galperin, E., Pasmanik-Chor, M., Tulzinsky, S., Bromberg, Y., Kozak, C.A., Joyner, A., Fein, A. & Horowitz, M. Ehd1–an eh-domain-containing protein with a specific expression pattern. *Genomics*, 59(1):66–76, 1999

[141] Haider, N.B., Searby, C., Galperin, E., Mintz, L., Horowitz, M., Stone, E.M. & Sheffield, V.C. Evaluation and molecular characterization of ehd1, a candidate gene for bardet-biedl syndrome 1 (bbs1). *Gene*, 240(1):227–232, 1999

[142] Pohl, U., Smith, J.S., Tachibana, I., Ueki, K., Lee, H.K., Ramaswamy, S., Wu, Q., Mohrenweiser, H.W., Jenkins, R.B. & Louis, D.N. Ehd2, ehd3, and ehd4 encode novel members of a highly conserved family of eh domain-containing proteins. *Genomics*, 63(2):255–262, 2000

[143] Grant, B., Zhang, Y., Paupard, M.C., Lin, S.X., Hall, D.H. & Hirsh, D. Evidence that rme-1, a conserved c. elegans eh-domain protein, functions in endocytic recycling. *Nat Cell Biol*, 3(6):573–579, 2001

[144] Naslavsky, N. & Caplan, S. Ehd proteins: key conductors of endocytic transport. *Trends Cell Biol*, 21(2):122–131, 2011

[145] Leberer, E., Charuk, J.H., Green, N.M. & MacLennan, D.H. Molecular cloning and expression of cdna encoding a lumenal calcium binding glycoprotein from sarcoplasmic reticulum. *Proc Natl Acad Sci U S A*, 86(16):6047–6051, 1989

[146] Leberer, E., Charuk, J.H., Clarke, D.M., Green, N.M., Zubrzycka-Gaarn, E. & MacLennan, D.H. Molecular cloning and expression of cdna encoding the 53,000-dalton glycoprotein of rabbit skeletal muscle sarcoplasmic reticulum. *J Biol Chem*, 264(6):3484–3493, 1989

[147] Rapaport, D., Auerbach, W., Naslavsky, N., Pasmanik-Chor, M., Galperin, E., Fein, A., Caplan, S., Joyner, A.L. & Horowitz, M. Recycling to the plasma membrane is delayed in ehd1 knockout mice. *Traffic*, 7(1):52–60, 2006

[148] Rainey, M.A., George, M., Ying, G., Akakura, R., Burgess, D.J., Siefker, E., Bargar, T., Doglio, L., Crawford, S.E., Todd, G.L., Govindarajan, V., Hess, R.A., Band, V., Naramura, M. & Band, H. The endocytic recycling regulator ehd1 is essential for spermatogenesis and male fertility in mice. *BMC Dev Biol*, 10:37, 2010

[149] George, M., Rainey, M.A., Naramura, M., Ying, G., Harms, D.W., Vitaterna, M.H., Doglio, L., Crawford, S.E., Hess, R.A., Band, V. & Band, H. Ehd4 is required to attain normal prepubertal testis size but dispensable for fertility in male mice. *Genesis*, 48(5):328–342, 2010

[150] Morén, B., Shah, C., Howes, M.T., Schieber, N.L., McMahon, H.T., Parton, R.G., Daumke, O. & Lundmark, R. Ehd2 regulates caveola dynamics via atp-driven targeting and oligomerization. *Mol Biol Cell*, 2012

[151] McNeil, P.L. & Khakee, R. Disruptions of muscle fiber plasma membranes. role in exercise-induced damage. *Am J Pathol*, 140(5):1097–1109, 1992

[152] Steinhardt, R.A., Bi, G. & Alderton, J.M. Cell membrane resealing by a vesicular mechanism similar to neurotransmitter release. *Science*, 263(5145):390–393, 1994

[153] Terasaki, M., Miyake, K. & McNeil, P.L. Large plasma membrane disruptions are rapidly resealed by ca2+-dependent vesicle-vesicle fusion events. *J Cell Biol*, 139(1):63–74, 1997

[154] Bi, G.Q., Alderton, J.M. & Steinhardt, R.A. Calcium-regulated exocytosis is required for cell membrane resealing. *J Cell Biol*, 131(6 Pt 2):1747–1758, 1995

[155] Miyake, K. & McNeil, P.L. Vesicle accumulation and exocytosis at sites of plasma membrane disruption. *J Cell Biol*, 131(6 Pt 2):1737–1745, 1995

[156] McNeil, P.L., Miyake, K. & Vogel, S.S. The endomembrane requirement for cell surface repair. *Proc Natl Acad Sci U S A*, 100(8):4592–4597, 2003

[157] Hernández-Deviez, D.J., Howes, M.T., Laval, S.H., Bushby, K., Hancock, J.F. & Parton, R.G. Caveolin regulates endocytosis of the muscle repair protein, dysferlin. *J Biol Chem*, 283(10):6476–6488, 2008

[158] Matsuda, C., Hayashi, Y.K., Ogawa, M., Aoki, M., Murayama, K., Nishino, I., Nonaka, I., Arahata, K. & Brown, Jr, R. The sarcolemmal proteins dysferlin and caveolin-3 interact in skeletal muscle. *Hum Mol Genet*, 10(17):1761–1766, 2001

[159] Bansal, D., Miyake, K., Vogel, S.S., Groh, S., Chen, C.C., Williamson, R., McNeil, P.L. & Campbell, K.P. Defective membrane repair in dysferlin-deficient muscular dystrophy. *Nature*, 423(6936):168–172, 2003

[160] Lennon, N.J., Kho, A., Bacskai, B.J., Perlmutter, S.L., Hyman, B.T. & Brown, Jr, R.H. Dysferlin interacts with annexins a1 and a2 and mediates sarcolemmal wound-healing. *J Biol Chem*, 278(50):50466–50473, 2003

[161] Cai, C., Masumiya, H., Weisleder, N., Matsuda, N., Nishi, M., Hwang, M., Ko, J.K., Lin, P., Thornton, A., Zhao, X., Pan, Z., Komazaki, S., Brotto, M., Takeshima, H. & Ma, J. Mg53 nucleates assembly of cell membrane repair machinery. *Nat Cell Biol*, 11(1):56–64, 2009

[162] Zhu, H., Lin, P., De, G., Choi, K.h., Takeshima, H., Weisleder, N. & Ma, J. Polymerase transcriptase release factor (ptrf) anchors mg53 protein to cell injury site for initiation of membrane repair. *J Biol Chem*, 286(15):12820–12824, 2011

[163] Marg, A., Schoewel, V., Timmel, T., Schulze, A., Shah, C., Daumke, O. & Spuler, S. Sarcolemmal repair is a slow process and includes ehd2. *Traffic*, 9999(999A), 2012

[164] Daumke, O., Lundmark, R., Vallis, Y., Martens, S., Butler, P.J.G. & McMahon, H.T. Architectural and mechanistic insights into an ehd atpase involved in membrane remodelling. *Nature*, 449(7164):923–927, 2007

[165] Reubold, T.F., Eschenburg, S., Becker, A., Leonard, M., Schmid, S.L., Vallee, R.B., Kull, F.J. & Manstein, D.J. Crystal structure of the gtpase domain of rat dynamin 1. *Proc Natl Acad Sci U S A*, 102(37):13093–13098, 2005

[166] won Lee, D., Zhao, X., Scarselletta, S., Schweinsberg, P.J., Eisenberg, E., Grant, B.D. & Greene, L.E. Atp binding regulates oligomerization and endosome association of rme-1 family proteins. *J Biol Chem*, 280(17):17213–17220, 2005

[167] Ghosh, A., Praefcke, G.J.K., Renault, L., Wittinghofer, A. & Herrmann, C. How guanylate-binding proteins achieve assembly-stimulated processive cleavage of gtp to gmp. *Nature*, 440(7080):101–104, 2006

[168] Low, H.H. & Löwe, J. A bacterial dynamin-like protein. *Nature*, 444(7120):766–769, 2006

[169] Low, H.H., Sachse, C., Amos, L.A. & Löwe, J. Structure of a bacterial dynamin-like protein lipid tube provides a mechanism for assembly and membrane curving. *Cell*, 139(7):1342–1352, 2009

[170] de Beer, T., Carter, R.E., Lobel-Rice, K.E., Sorkin, A. & Overduin, M. Structure and asn-pro-phe binding pocket of the eps15 homology domain. *Science*, 281(5381):1357–1360, 1998

[171] Santolini, E., Salcini, A.E., Kay, B.K., Yamabhai, M. & Fiore, P.P.D. The eh network. *Exp Cell Res*, 253(1):186–209, 1999

[172] Polo, S., Confalonieri, S., Salcini, A.E. & Fiore, P.P.D. Eh and uim: endocytosis and more. *Sci STKE*, 2003(213):re17, 2003

[173] Kieken, F., Jović, M., Tonelli, M., Naslavsky, N., Caplan, S. & Sorgen, P.L. Structural insight into the interaction of proteins containing npf, dpf, and gpf motifs with the c-terminal eh-domain of ehd1. *Protein Sci*, 18(12):2471–2479, 2009

[174] Chen, H., Fre, S., Slepnev, V.I., Capua, M.R., Takei, K., Butler, M.H., Fiore, P.P.D. & Camilli, P.D. Epsin is an eh-domain-binding protein implicated in clathrin-mediated endocytosis. *Nature*, 394(6695):793–797, 1998

[175] Martina, J.A., Bonangelino, C.J., Aguilar, R.C. & Bonifacino, J.S. Stonin 2: an adaptor-like protein that interacts with components of the endocytic machinery. *J Cell Biol*, 153(5):1111–1120, 2001

[176] Rumpf, J., Simon, B., Jung, N., Maritzen, T., Haucke, V., Sattler, M. & Groempingko, Y. Structure of the eps15-stonin2 complex provides a molecular explanation for eh-domain ligand specificity. *EMBO J*, 27(3):558–569, 2008

[177] Braun, A., Pinyol, R., Dahlhaus, R., Koch, D., Fonarev, P., Grant, B.D., Kessels, M.M. & Qualmann, B. Ehd proteins associate with syndapin i and ii and such interactions play a crucial role in endosomal recycling. *Mol Biol Cell*, 16(8):3642–3658, 2005. 090909 literature seminar

[178] Guilherme, A., Soriano, N.A., Bose, S., Holik, J., Bose, A., Pomerleau, D.P., Furcinitti, P., Leszyk, J., Corvera, S. & Czech, M.P. Ehd2 and the novel eh domain binding protein ehbp1 couple endocytosis to the actin cytoskeleton. *J Biol Chem*, 279(11):10593–10605, 2004

[179] Shpetner, H.S., Herskovits, J.S. & Vallee, R.B. A binding site for sh3 domains targets dynamin to coated pits. *J Biol Chem*, 271(1):13–16, 1996

[180] Okamoto, P.M., Herskovits, J.S. & Vallee, R.B. Role of the basic, proline-rich region of dynamin in src homology 3 domain binding and endocytosis. *J Biol Chem*, 272(17):11629–11635, 1997

[181] Simpson, F., Hussain, N.K., Qualmann, B., Kelly, R.B., Kay, B.K., McPherson, P.S. & Schmid, S.L. Sh3-domain-containing proteins function at distinct steps in clathrin-coated vesicle formation. *Nat Cell Biol*, 1(2):119–124, 1999

[182] Low, H.H. & Löwe, J. Dynamin architecture-from monomer to polymer. *Curr Opin Struct Biol*, 2010

[183] Sambrook, J., Russell, D.W. & Laboratory., C.S.H. *Molecular cloning : a laboratory manual*. Cold Spring Harbor Laboratory, Cold Spring Harbor, N.Y. :, 3rd. ed. ed., 2001

[184] Chung, C.T., Niemela, S.L. & Miller, R.H. One-step preparation of competent escherichia coli: transformation and storage of bacterial cells in the same solution. *Proc Natl Acad Sci U S A*, 86(7):2172–2175, 1989

[185] Doublié, S. Production of selenomethionyl proteins in prokaryotic and eukaryotic expression systems. *Methods Mol Biol*, 363:91–108, 2007

[186] Bradford, M.M. A rapid and sensitive method for the quantitation of microgram quantities of protein utilizing the principle of protein-dye binding. *Anal Biochem*, 72:248–254, 1976

[187] Wilkins, M.R., Gasteiger, E., Bairoch, A., Sanchez, J.C., Williams, K.L., Appel, R.D. & Hochstrasser, D.F. Protein identification and analysis tools in the expasy server. *Methods Mol Biol*, 112:531–552, 1999

[188] Lenzen, C., Cool, R.H. & Wittinghofer, A. Analysis of intrinsic and cdc25-stimulated guanine nucleotide exchange of p21ras-nucleotide complexes by fluorescence measurements. *Methods Enzymol*, 255:95–109, 1995

[189] Ladokhin, A.S., Wimley, W.C. & White, S.H. Leakage of membrane vesicle contents: determination of mechanism using fluorescence requenching. *Biophys J*, 69(5):1964–1971, 1995

[190] Ladokhin, A.S., Wimley, W.C., Hristova, K. & White, S.H. Mechanism of leakage of contents of membrane vesicles determined by fluorescence requenching. *Methods Enzymol*, 278:474–486, 1997

[191] Piston, D.W. & Kremers, G.J. Fluorescent protein fret: the good, the bad and the ugly. *Trends Biochem Sci*, 32(9):407–414, 2007

[192] Tamrazi, A., Carlson, K.E., Daniels, J.R., Hurth, K.M. & Katzenellenbogen, J.A. Estrogen receptor dimerization: ligand binding regulates dimer affinity and dimer dissociation rate. *Mol Endocrinol*, 16(12):2706–2719, 2002

[193] Ohi, M., Li, Y., Cheng, Y. & Walz, T. Negative staining and image classification - powerful tools in modern electron microscopy. *Biol Proced Online*, 6:23–34, 2004

[194] Altenbach, C., Flitsch, S.L., Khorana, H.G. & Hubbell, W.L. Structural studies on transmembrane proteins. 2. spin labeling of bacteriorhodopsin mutants at unique cysteines. *Biochemistry*, 28(19):7806–7812, 1989

[195] Margittai, M. & Langen, R. Spin labeling analysis of amyloids and other protein aggregates. *Methods Enzymol*, 413:122–139, 2006. o80716 literature seminar

[196] Altenbach, C., Greenhalgh, D.A., Khorana, H.G. & Hubbell, W.L. A collision gradient method to determine the immersion depth of nitroxides in lipid bilayers: application to spin-labeled mutants of bacteriorhodopsin. *Proc Natl Acad Sci U S A*, 91(5):1667–1671, 1994

[197] Hubbell, W.L., Gross, A., Langen, R. & Lietzow, M.A. Recent advances in site-directed spin labeling of proteins. *Curr Opin Struct Biol*, 8(5):649–656, 1998

[198] Pannier, M., Veit, S., Godt, A., Jeschke, G. & Spiess, H.W. Dead-time free measurement of dipole-dipole interactions between electron spins. *J Magn Reson*, 142(2):331–340, 2000

[199] Chiang, Y.W., Borbat, P.P. & Freed, J.H. The determination of pair distance distributions by pulsed esr using tikhonov regularization. *J Magn Reson*, 172(2):279–295, 2005

[200] Jeschke, G., Chechik, V., Ionita, P., Godt, A., Zimmermann, H., Banham, J., Timmel, C.R., Hilger, D. & Jung, H. Deeranalysis2006 - a comprehensive software package for analyzing pulsed eldor data. *APPLIED MAGNETIC RESONANCE*, 30(3-4):473–498, 2006

[201] Polyhach, Y., Bordignon, E. & Jeschke, G. Rotamer libraries of spin labelled cysteines for protein studies. *Phys Chem Chem Phys*, 13(6):2356–2366, 2011

[202] Hatmal, M.M., Li, Y., Hegde, B.G., Hegde, P.B., Jao, C.C., Langen, R. & Haworth, I.S. Computer modeling of nitroxide spin labels on proteins. *Biopolymers*, 97(1):35–44, 2012

[203] Leslie, A.G.W. The integration of macromolecular diffraction data. *Acta Crystallogr D Biol Crystallogr*, 62(Pt 1):48–57, 2006

[204] Kabsch, W. Xds. *Acta Crystallogr D Biol Crystallogr*, 66(Pt 2):125–132, 2010

[205] Vonrhein, C., Blanc, E., Roversi, P. & Bricogne, G. Automated structure solution with autosharp. *Methods Mol Biol*, 364:215–230, 2007

[206] Emsley, P., Lohkamp, B., Scott, W.G. & Cowtan, K. Features and development of coot. *Acta Crystallogr D Biol Crystallogr*, 66(Pt 4):486–501, 2010

[207] Winn, M.D., Isupov, M.N. & Murshudov, G.N. Use of tls parameters to model anisotropic displacements in macromolecular refinement. *Acta Crystallogr D Biol Crystallogr*, 57(Pt 1):122–133, 2001

[208] Murshudov, G.N., Skubák, P., Lebedev, A.A., Pannu, N.S., Steiner, R.A., Nicholls, R.A., Winn, M.D., Long, F. & Vagin, A.A. Refmac5 for the refinement of macromolecular crystal structures. *Acta Crystallogr D Biol Crystallogr*, 67(Pt 4):355–367, 2011

[209] Davis, I.W., Leaver-Fay, A., Chen, V.B., Block, J.N., Kapral, G.J., Wang, X., Murray, L.W., Arendall, W.B., Snoeyink, J., Richardson, J.S. & Richardson, D.C. Molprobity: all-atom contacts and structure validation for proteins and nucleic acids. *Nucleic Acids Res*, 35(Web Server issue):W375–W383, 2007

[210] Larkin, M.A., Blackshields, G., Brown, N.P., Chenna, R., McGettigan, P.A., McWilliam, H., Valentin, F., Wallace, I.M., Wilm, A., Lopez, R., Thompson, J.D., Gibson, T.J. & Higgins, D.G. Clustal w and clustal x version 2.0. *Bioinformatics*, 23(21):2947–2948, 2007

[211] Goujon, M., McWilliam, H., Li, W., Valentin, F., Squizzato, S., Paern, J. & Lopez, R. A new bioinformatics analysis tools framework at embl-ebi. *Nucleic Acids Res*, 38(Web Server issue):W695–W699, 2010

[212] Matthews, B.W. Solvent content of protein crystals. *J Mol Biol*, 33(2):491–497, 1968

[213] Diederichs, K. & Karplus, P.A. Improved r-factors for diffraction data analysis in macromolecular crystallography. *Nat Struct Biol*, 4(4):269–275, 1997

[214] Cieślik, M. & Derewenda, Z.S. The role of entropy and polarity in intermolecular contacts in protein crystals. *Acta Crystallogr D Biol Crystallogr*, 65(Pt 5):500–509, 2009

[215] Derewenda, Z.S. Rational protein crystallization by mutational surface engineering. *Structure*, 12(4):529–535, 2004

[216] Goldschmidt, L., Cooper, D.R., Derewenda, Z.S. & Eisenberg, D. Toward rational protein crystallization: A web server for the design of crystallizable protein variants. *Protein Sci*, 16(8):1569–1576, 2007

[217] Frazier, A.A., Roller, C.R., Havelka, J.J., Hinderliter, A. & Cafiso, D.S. Membrane-bound orientation and position of the synaptotagmin i c2a domain by site-directed spin labeling. *Biochemistry*, 42(1):96–105, 2003

[218] Hansen, C.G., Howard, G. & Nichols, B.J. Pacsin 2 is recruited to caveolae and functions in caveolar biogenesis. *J Cell Sci*, 124(Pt 16):2777–2785, 2011

[219] Stoeber, M., Stoeck, I.K., Hänni, C., Bleck, C.K.E., Balistreri, G. & Helenius, A. Oligomers of the atpase ehd2 confine caveolae to the plasma membrane through association with actin. *EMBO J*, 2012

[220] Naslavsky, N., Rahajeng, J., Chenavas, S., Sorgen, P.L. & Caplan, S. Ehd1 and eps15 interact with phosphatidylinositols via their eps15 homology domains. *J Biol Chem*, 282(22):16612–16622, 2007

[221] Vetter, I.R. & Wittinghofer, A. The guanine nucleotide-binding switch in three dimensions. *Science*, 294(5545):1299–1304, 2001

[222] Byrnes, L.J. & Sondermann, H. Structural basis for the nucleotide-dependent dimerization of the large g protein atlastin-1/spg3a. *Proc Natl Acad Sci U S A*, 2011

[223] Niemann, H.H., Knetsch, M.L., Scherer, A., Manstein, D.J. & Kull, F.J. Crystal structure of a dynamin gtpase domain in both nucleotide-free and gdp-bound forms. *EMBO J*, 20(21):5813–5821, 2001

[224] Chappie, J.S., Mears, J.A., Fang, S., Leonard, M., Schmid, S.L., Milligan, R.A., Hinshaw, J.E. & Dydaca, F. A pseudoatomic model of the dynamin polymer identifies a hydrolysis-dependent powerstroke. *Cell*, 147(1):209–222, 2011

[225] Zhang, P. & Hinshaw, J.E. Three-dimensional reconstruction of dynamin in the constricted state. *Nat Cell Biol*, 3(10):922–926, 2001

[226] Chen, Y.J., Zhang, P., Egelman, E.H. & Hinshaw, J.E. The stalk region of dynamin drives the constriction of dynamin tubes. *Nat Struct Mol Biol*, 11(6):574–575, 2004

[227] Bhatia, V.K., Hatzakis, N.S. & Stamoutakei, D. A unifying mechanism accounts for sensing of membrane curvature by bar domains, amphipathic helices and membrane-anchored proteins. *Semin Cell Dev Biol*, 21(4):381–390, 2010

[228] Hamilton, N., Kerr, M.C., Burrage, K. & Teasdale, R.D. Analyzing real-time video microscopy: the dynamics and geometry of vesicles and tubules in endocytosis. *Curr Protoc Cell Biol*, Chapter 14:Unit 4.16, 2007

[229] Antonny, B., Beraud-Dufour, S., Chardin, P. & Chabre, M. N-terminal hydrophobic residues of the g-protein adp-ribosylation factor-1 insert into membrane phospholipids upon gdp to gtp exchange. *Biochemistry*, 36(15):4675–4684, 1997

[230] Schwefel, D., Fröhlich, C., Eichhorst, J., Wiesner, B., Behlke, J., Aravind, L. & Daumke, O. Structural basis of oligomerization in septin-like gtpase of immunity-associated protein 2 (gimap2). *Proc Natl Acad Sci U S A*, 107(47):20299–20304, 2010

[231] Henley, J.R., Krueger, E.W., Oswald, B.J. & McNiven, M.A. Dynamin-mediated internalization of caveolae. *J Cell Biol*, 141(1):85–99, 1998

[232] Oh, P., McIntosh, D.P. & Schnitzer, J.E. Dynamin at the neck of caveolae mediates their budding to form transport vesicles by gtp-driven fission from the plasma membrane of endothelium. *J Cell Biol*, 141(1):101–114, 1998

[233] Campelo, F., Fabrikant, G., McMahon, H.T. & Kozlov, M.M. Modeling membrane shaping by proteins: Focus on ehd2 and n-bar domains. *FEBS Lett*, 2009

[234] Schröder, G.F., Brunger, A.T. & Levitt, M. Combining efficient conformational sampling with a deformable elastic network model facilitates structure refinement at low resolution. *Structure*, 15(12):1630–1641, 2007

[235] Bronshtein, I.N., Semendyayev, K.A., Musiol, G. & Muehlig, H. *Handbook of Mathematics*. Springer, 2004

[236] Isas, J.M., Langen, R., Hubbell, W.L. & Haigler, H.T. Structure and dynamics of a helical hairpin that mediates calcium-dependent membrane binding of annexin b12. *J Biol Chem*, 279(31):32492–32498, 2004

[237] Jeschke, G. Deer distance measurements on proteins. *Annu Rev Phys Chem*, 63:419–446, 2012

ACKNOWLEDGMENTS

I would like to thank Prof. Dr. Oliver Daumke for his excellent guidance. He is one of the smartest and most positive persons I met. Our group is fascinating, enabled with a truly scientific spirit without ever forgetting about the fun part. Special thanks to Katja Fälber, Steven Marino and Eva Rosenbaum for critical reading of my thesis.

My collaboration partners Dr. Ralf Langen, Los Angeles, California, USA, Dr. Balachandra Gajanan Hegde, Bangalore, Karnataka, India, and the group of Dr. Richard Lundmark, Umeå, Sweden contributed very valuably to this joint project.

My doctor father Prof. Dr. Udo Heinemann is a great source of knowledge and provides useful hints in our group seminars. His group, specially Florian Mayr, was always open for sharing science or a beer.

My intern students Aloysius Wilfred Raj Arokiaraj, Miriam Chebli, Philip Luxen and Megha Boilla advanced the project with cloning and protein purifications. I hope you learned something during your internship!

Of course, I also want to thank the MDC, the FMP, the graduate office and all PhD students and PostDocs for providing an excellent research environment on campus. Not to forget my always encouraging friends Wolfi, Benni, Jan, Maxi, Sabby, Flo, my parents Krishna and Ulrike Shah, and my sister Carolin Shah.